Cosmological Investigations On Large And Small Scales

Dissertation
zur
Erlangung des Doktorgrades (Dr. rer. nat.)
der
Mathematisch-Naturwissenschaftlichen Fakultät
der
Rheinischen Friedrich-Wilhelms-Universität Bonn

von
Behnam Javanmardi
aus
Shiraz (Iran)

Bonn, October 2016

Dieser Forschungsbericht wurde als Dissertation von der Mathematisch-Naturwissenschaftlichen Fakultät der Universität Bonn angenommen und ist auf dem Hochschulschriftenserver der ULB Bonn http://hss.ulb.uni-bonn.de/diss_online elektronisch publiziert.

1. Gutachter:	Prof. Dr. Pavel Kroupa
2. Gutachter:	Prof. Dr. Cristiano Porciani
Tag der Promotion:	08.02.2017
Erscheinungsjahr:	2017

To Leila Chaboki and Jalil Javanmardi
my first and best teachers.

Contents

Abstract

The standard model of cosmology, founded on Einstein's theory of gravity and on the Cosmological Principle (CP), has been understood as being successful in providing explanations for many observations so far. However, it relies on some yet unknown components; dark matter and dark energy. Apart from these two problems, there are some other interesting challenges for this model on both large and small scales. On large scales, some deviations from isotropy in the Cosmic Microwave Background (CMB) radiation have stimulated studies on testing isotropy using various extragalactic data. On small scales there are long-lasting issues with the predictions of structure formation in the standard model and the observed properties of the Local Group (LG) of Galaxies. The contribution of this thesis is testing the assumption of isotropy of the CP on large scales and launching a survey of dwarf galaxies for addressing the small scale problems.

On large scales, first we probed the isotropy of cosmic acceleration using the magnitude-redshift relation of high redshift Type Ia Supernovae (SNe Ia). We found that although the deviation from isotropy is small, it is significantly aligned with the direction of the CMB dipole. This can be either due to uncleaned systematics, or some yet unknown phenomena. However, because of the non-uniformity of the sky distribution of the current SNe Ia data sets, it is hard to draw a firm conclusion. We then probed the isotropy of the distribution of the galaxy morphological types for the first time. We used the de Vaucouleurs morphological types of more than 60,000 galaxies from the HyperLeda database within a distance of about 200 Mpc. Surprisingly, we found a significant hemispherical asymmetry aligned with the celestial equator. Regardless of the significance of the difference in the distribution, the observed alignment would be a major challenge for the CP if the anisotropy is real. However since the asymmetry has a north-south alignment, it is most likely due to a systematic bias in the classifications of the morphological types or in the homogenization procedure of the catalog. Further studies are essential to reveal the exact source of this anisotropy. Future all-sky surveys can provide a large number of SNe Ia, and can deliver uniform measurements of galaxy morphological types for further testing of the assumption of isotropy.

On small scales, we started the Dwarf Galaxy Survey with Amateur Telescopes (DGSAT) in which we use long exposure wide field images obtained by, as the name suggests, small telescopes to search for dwarf satellite galaxies around nearby Milky-Way-type galaxies. Increasing the number of known dwarf satellite galaxies outside the LG is necessary for testing the predictions of the standard model of cosmology in other galaxy groups. In the first application of the survey we managed to discover eleven low surface brightness (LSB) galaxies around six nearby Milky-Way-type galaxies. These LSB galaxies have similar properties to the satellite galaxies in the LG. The DGSAT will continue its operation and we are very optimistic that we can find more LSB galaxies outside the LG.

The forthcoming huge amount of data in the next two decades from various large and small surveys will provide valuable information for studying the assumptions and predictions of the current standard model of cosmology and can enhance our knowledge about the Universe.

The Effort For Understanding The Cosmos

"there is at least one philosophical problem in which all thinking men are interested. It is the problem of cosmology: the problem of understanding the world – including ourselves, and our knowledge, as part of the world. All science is cosmology, I believe, and for me the interest of philosophy, no less than of science, lies solely in the contributions which it has made to it"

Karl Popper, The Logic of Scientific Discovery (1959)

To the best of our knowledge, so far we (humans) are the only *pieces* of Nature who are trying to comprehend it. Apart from many interesting questions from inside ourselves to our immediate outside environment on this planet, the sky has always fascinated us, perhaps since the time when our primitive ancestors were gazing at it. It has been linked to many myths and supernatural powers and was believed to have great influence on our lives on Earth. All around the Earth and from various ancient civilizations, we can find evidences for the efforts to observe the *heavenly* objects, to follow their movement in the sky, to build a model of the Universe, and to determine our position in it. Our conception of the Universe has changed a lot in the past few centuries, from being at the center of the Universe to living on a tiny planet orbiting one of the hundreds of billions of stars in one of the hundreds of billions of galaxies in the Universe.

Modern cosmology, by using the laws of physics, is trying to answer the same questions that our ancestors used to ask. Why is the Universe like what we observe?, how did it become like this?, and how do we happen to be where we are? Many observations in the past decades helped cosmologists to build a standard model of cosmology which the majority of cosmologists take to be successful in explaining many observations but which has problems with explaining some others.

In the Introduction to this thesis (Chapter 1) I briefly describe, mostly in historical order, our current status of knowledge in cosmology. Then I introduce the basic formulations of the standard model of cosmology and some of its consequences related to the projects in my thesis. After mentioning the successes of this model, I focus on some of its challenges and problems. Chapters 2, 3, and 4 are my contributions towards finding the answers to those problems, and I provide a summary of the thesis and an outlook in Chapter 5.

CHAPTER 1

Introduction

1.1 A Universe of Galaxies

We live in a galaxy (a gravitationally bound system of stars, gas, and dust), and the Universe is observed to have numerous galaxies with different shapes and at different distances. But this was not known until the last century.

The "milky" hoop of light which is observable in a dark night sky has been linked to many myths and stories, but as early as 400 BC Democritus suggested that the *Milky Way* is a combination of numerous distant stars. In 964 AD in his *Book of Fixed Stars*[1], Sufi (also referred to as Al-Sufi or Azophi) identified two nebulous objects in the sky, (later named as) the Andromeda galaxy and the Large Magellanic Cloud, and noted them as "a small cloud" and "white ox", respectively (Al-Sufi 964)[2]. In 1610, Galileo Galilei pointed his telescope towards the Milky Way for the first time and confirmed that it actually consists of a large number of stars (Galilei 1610). In the 1770s, Charles Messier catalogued 109 objects with nebulous appearance (Messier 1771). They are named with an M and a number (e.g. the Andromeda galaxy is M31 in the Messier catalog). In the 1880s, J. L. E. Dreyer compiled *The New General Catalogue of Nebulae and Clusters of Stars* (abbreviated as NGC) which contained more than 7800 objects (Dreyer 1888). However, all of the observed "nebulae" were commonly believed to be in our Galaxy until the first decades of the 20th century when astronomers started to realize that many of them are galaxies similar to, but at large distances from, our Milky Way. This revolutionized our understanding of the Universe and was the beginning of the *extragalactic astronomy* era.

1.1.1 Morphological classification of galaxies

A common approach of different branches of science for studying objects, entities or phenomena, is to classify them into various categories based on their observed properties. In the beginning of the last century, as the number of big telescopes and the amount of data were growing, a larger number of galaxies were detected and astronomers started to classify them based on their appearance. The earliest works on this attempt were those of Reynolds (1920), Hubble (1926), Jeans (1928), and Hubble (1936) whose efforts provided the famous sequence of galaxy morphologies known as the "Hubble's

[1] A catalog of stars in the constellations established by Ptolemy's *Almagest* around 100 AD.
[2] For historical notes see Matvievskaya (1983) and van Gent (2014).

tuning fork"[3]. Since historically optical observations were the main method of observing galaxies, this classification scheme (shown in Figure 1.1) is based on the visual classification of optical images. Apart from morphological features, galaxies can be classified based on other criteria (e.g. color indices, or spectral properties). However, the tuning fork scheme is still the most commonly used classification. It has three main classes, *elliptical*, *lenticular*, and *spiral* galaxies. On the left side of the fork the ellipticals are located and are ordered according to their degree of ellipticity (e.g. E0 has no ellipticity and is almost circular in projection on the sky). On the right hand side, the spirals are located which are divided into two classes of normal spirals, S, and barred spirals, SB. The spirals are categorized according to the ratio of bulge to disk luminosity and are named as a, b, and c (as well as intermediate stages ab and bc, not shown in Figure 1.1). Between the ellipticals and spirals lie the lenticular galaxies which appear to be a transition class between the two above-mentioned classes. Though they are disk-like galaxies, they do not show a clear spiral structure. The galaxies that do not fall into these three classes are referred to as *irregular* galaxies. Elliptical and spiral galaxies are sometimes referred to as *early* and *late* type galaxies, respectively. However, it should be emphasized that these names are only of historical origin and are not related to the evolutionary stage of galaxies. The morphological classification of galaxies is one of the important ways to study their formation and evolution and a considerable fraction of research in extragalactic astronomy is devoted to improving the classification methods and developing automated (rather than visual) approaches useable for future large scale galaxy surveys[4].

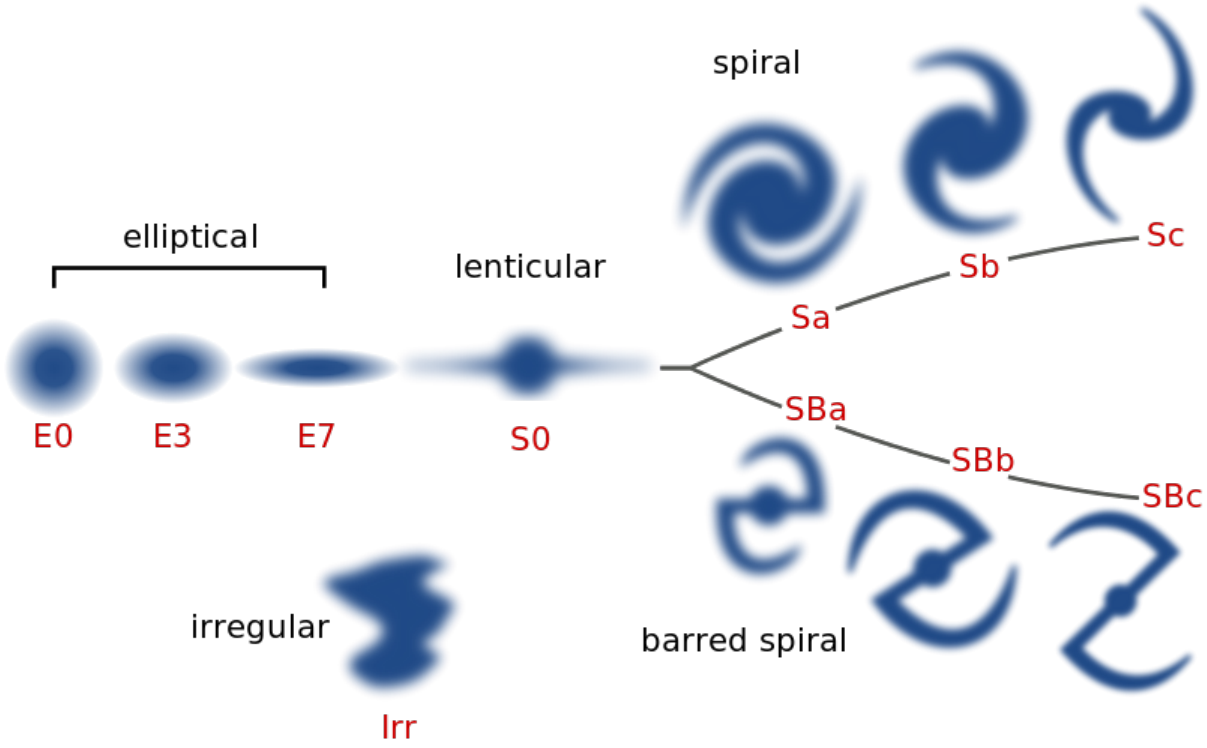

Figure 1.1: The "Hubble's tuning fork" classification for galaxy morphologies based on Reynolds (1920), Hubble (1926), Jeans (1928), and Hubble (1936). See Block & Freeman (2015). Credit: Wikipedia Public Domain.

[3] But see Block & Freeman (2015) for a historical note on the origin of this classification.
[4] For a recent review on galaxy morphology see Buta (2013).

1.2 Galaxies Are Receding From Us: An Expanding Universe

With observational evidence for the expansion of the Universe emerging in the beginning of the last century, the foundations of modern cosmology started to be formed. Slipher (1915) was one of the first observers who measured the radial velocity, v, of some galaxies (still known as *nebulae* at the time) using their redshifts, z. Redshift is the increase in the wavelength (a shift towards the red in the spectrum) of the electromagnetic radiation emitted from an object due to its motion away from the observer and is defined as:

$$z = \frac{\lambda_{obs} - \lambda_{emit}}{\lambda_{emit}} \tag{1.1}$$

where λ_{emit} and λ_{obs} are the emitted and observed wavelengths, respectively. If the source is moving towards the observer, its spectrum would be blueshifted instead. It can be seen in Slipher's paper that the majority of the galaxies in his study had a positive v meaning that they are receding from us. Seven years later, using the Einstein (1915) General Theory of Relativity, Friedmann (1922) derived a set of equations for a non-static (possibly expanding) universe. The same equations were later presented by Lemaître (1927) who also used a set of radial velocity, v, and distance, D, measurements of some galaxies and calculated the expansion rate of the Universe. The relation between v and D is today known as the "Hubble law" presented two years later in Hubble (1929)[5]. Based on this law, the more distant a galaxy, the larger is its recession velocity,

$$v = H_0 D \tag{1.2}$$

where the constant of proportionality, H_0, is today known as the Hubble constant. H_0 is one of the most important cosmological parameters and its measurement is constantly the purpose of many big projects. For velocities much smaller than the speed of light we have $z \approx \frac{v}{c}$, which relates the redshift and the distance through $cz = H_0 D$. Because of this relation, on cosmological scales the redshift of an object is considered as a measure of its distance.

Observing that distant galaxies are all redshifted and interpreting it as the expansion of the Universe led to the notion that it should have been very small sometime in the past (assuming that it has been always expanding). In an expanding universe, the redshift of a distant source is mainly due to the expansion of the space and only a fraction of that is caused by the peculiar motion of the source. This was the initiation of the "Big Bang" model for the origin and evolution of the Universe, which basically states that the Universe started from a very hot and very dense state and evolved to what we now observe.

1.3 The Cosmic Microwave Background

After the Cosmic Microwave Background (CMB) radiation was (accidentally) discovered by Penzias & Wilson (1965), who won the Physics Nobel Prize in 1978 for this discovery, the Big Bang has become the accepted cosmological theory. This radiation has been predicted in a series of studies by George Gamow, Ralph Alpher and Robert Herman (Gamow 1946; Alpher & Herman 1948, 1949; Gamow 1956). CMB is often termed as the "afterglow" of the Big Bang and is basically the radiation initiated at the moment when the photons and the matter particles of the early Universe decoupled from each other. This happened when the temperature of the Universe dropped enough (due to the expansion) so that the photons were not energetic enough to stop protons and electrons from binding. After this time, called the last scattering,

[5] See Block & Freeman (2015) for a historical note.

photons started propagating freely in space. These photons have since lost even more energy during the expansion of the Universe and are now observed in the microwave wavelength from every direction in the sky. The spectrum of CMB radiation is well fitted by that of a black body with a temperature of about 2.7 kelvins[6]. The temperature of the CMB radiation from different directions in the sky is very uniform (see the top panel of Figure 1.2). The largest anisotropy in the CMB was found by the COBE[7] satellite and has a dipole shape. The temperature of the CMB radiation is higher in one direction in the sky and is lower in the opposite direction. The middle panel of Figure 1.2 shows this CMB dipole. This is caused due to the net motion of our Solar System with respect to the CMB radiation. In other words, our net motion (due to the rotation of the Sun around the Galactic center and the motion of the Milky Way in the Local Group of Galaxies and the motion of the Local Group) causes the CMB photons coming from the direction of the motion to be less redshifted than the photons coming from the opposite direction. Removing this dipole pattern and the foreground radiation from our own Galaxy (seen as a horizontal band at the center of the bottom panel of Figure 1.2) gives us the all-sky map of the CMB. A recent map of the CMB[8] is shown in Figure 1.3. We see small anisotropies or fluctuations in the CMB which are of the order of only 10^{-5} K. The dominant contributor to these anisotropies (predicted by Sachs & Wolfe 1967, before detected by COBE and later experiments) is considered to be the small fluctuations in the distribution of matter in the early universe and at the time of the last scattering. In other words, CMB photons carry the information on their last interaction with the matter content of the early Universe and tell us how that distribution used to be around 13 billion years ago. In this respect, the CMB is a rich source of information for cosmologists.

1.3.1 Cosmic inflation

Why is the temperature of the CMB radiation so uniform across the sky? This uniformity means that all the CMB should have been radiated from a region in thermal equilibrium, which would mean that the whole region should have been in causal contact. However, the speed of light is finite and the maximum distance that light could have travelled until the last scattering can cover only around 1 deg on the sky. This means that the CMB should be uniform only on scales of ≈ 1 deg^2, but we observe it to be uniform across the whole sky, i.e. $\approx 41,253$ deg^2.

This so called "horizon problem" was raised in the 1970s and challenged the then standard model of cosmology. In the 1980s, a model was developed (Guth 1981; Linde 1982; Albrecht & Steinhardt 1982) that can be the solution to this problem (and a few others) by assuming that the Universe has undergone a rapid enormous expansion shortly after the Big Bang. Based on this model, called "inflation", the Universe has expanded by a factor of about 10^{27} from about 10^{-36}s to about 10^{-34}s after the Big Bang (see e.g. Liddle 2003). Inflation can also provide explanations for the observed flatness of the Universe (see Section 1.5.1) and the very small temperature fluctuations in the CMB (Guth 1997).

1.4 Acceleration of The Cosmic Expansion

The Universe contains matter which is naturally expected to slow down the cosmic expansion due to gravity. In the late 1990s, two independent groups of astronomers (the Supernova Cosmology Project led by Saul Perlmutter and the High-Z Supernova Search Team led by Brian P. Schmidt) were busy with observing cosmological standard candles (explained in Section 1.5.2) to measure the deceleration rate of

[6] More precisely 2.72548 ± 0.00057 kelvins (Fixsen 2009).
[7] Cosmic Background Explorer (Smoot et al. 1990; Mather et al. 1991)
[8] Observed by the *Planck* satellite (Planck Collaboration et al. 2014a)

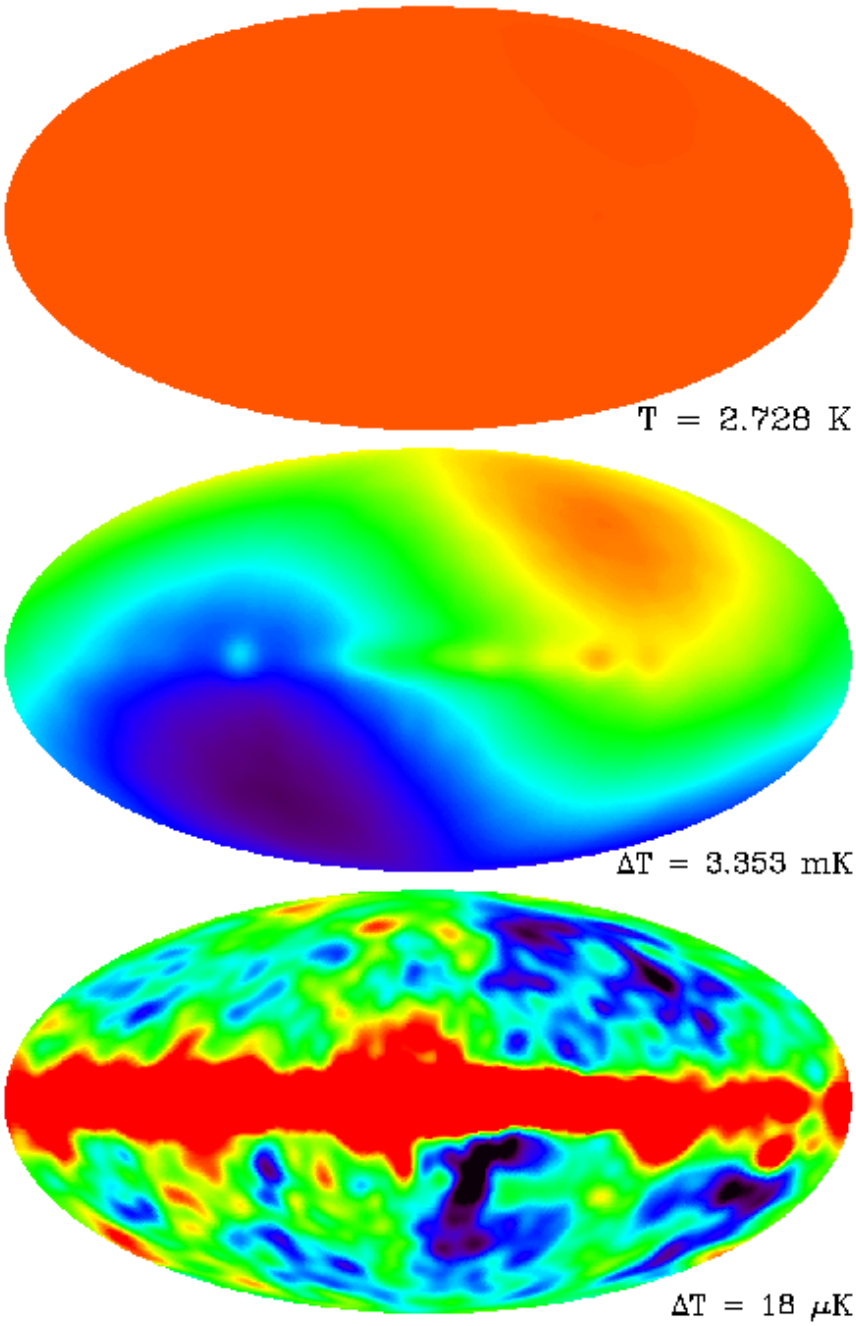

Figure 1.2: The microwave sky as observed by COBE in the Galactic coordinate system. Top: the scale is between 0 to 4 K showing the uniformity of the CMB. Middle: with a scale intended to show the contrast due to the dipole. Bottom: after subtracting the dipole. The horizontal band in the center is the foreground radiation from the Milky way. Credit: NASA and the COBE Collaboration.

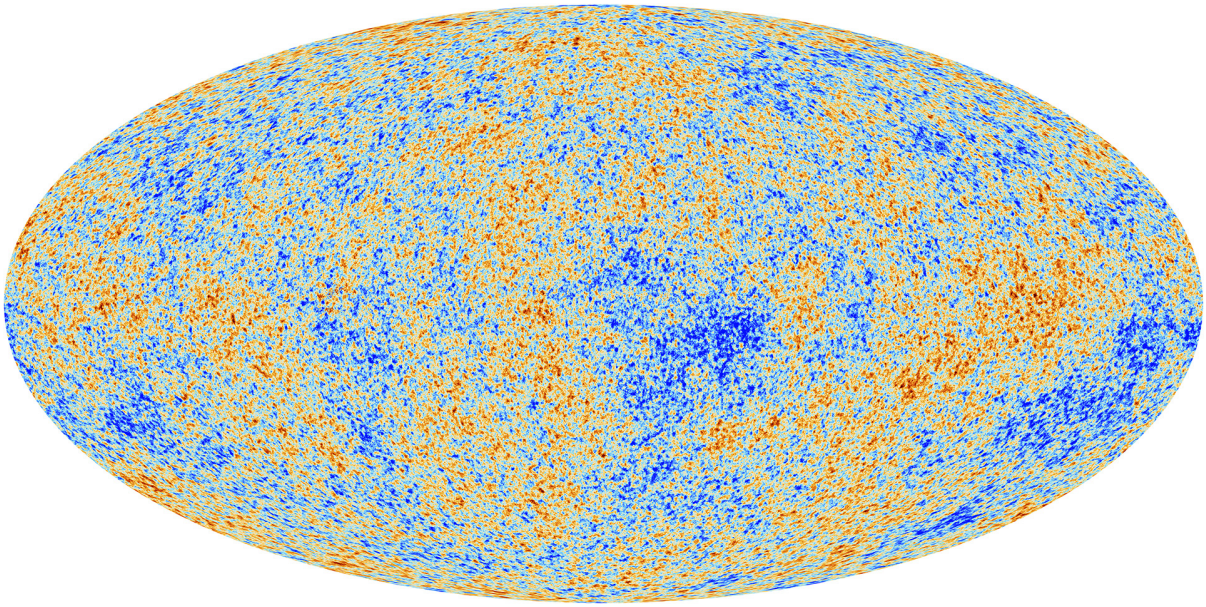

Figure 1.3: CMB temperature fluctuation map observed by the *Planck* satellite (Planck Collaboration et al. 2014a). Credit: ESA and the *Planck* Collaboration.

the expansion. Surprisingly, they found exactly the opposite of the expectations; the expansion of the Universe seems to be accelerating (Riess et al. 1998; Perlmutter et al. 1999). Saul Perlmutter, Brian P. Schmidt and Adam G. Riess, received the Nobel Prize in Physics in 2011 for this discovery. Within the framework of the standard model of cosmology, the cause of this acceleration is explained by adding a repulsive component called "dark energy" to the mass-energy contents of the Universe or by adding a cosmological constant. A large fraction of the research in cosmology is devoted to understanding the yet unknown nature of the cause of the acceleration or to find an alternative approach for explaining its related observations.

1.5 The Standard Model of Cosmology

The standard model of cosmology is founded on two assumptions:

- The Cosmological Principle (CP), and
- The validity of the Einstein theory of General Relativity (GR) on all scales.

The former is a generalized form of the Copernican Principle which states that we are not in a privileged place in the Universe. Based on the CP, the distribution of matter and energy in the Universe is expected to be homogeneous and isotropic when viewed on sufficiently large scales. This implies that the distant observables in different directions from our perspective should be statistically similar.

The latter assumes that no matter what scale we are considering, gravity is governed by GR. In GR, the geometry of space (more accurately space-time) tells the matter how to move, and at the same time, the amount and the distribution of matter tells the space what geometry to acquire.

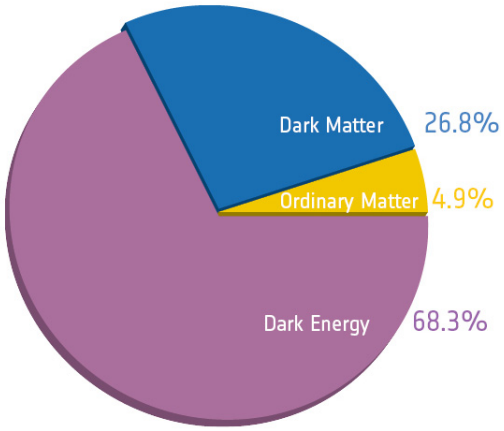

Figure 1.4: The contribution of matter and energy components of the Universe based on CMB observations (Planck Collaboration et al. 2014a). Credit: ESA and the *Planck* Collaboration.

Since these assumptions are fundamental, they should be tested continuously as new observations are being performed. However, they are very useful in the sense that they allow us to obtain a set of simple equations for the evolution of the Universe.

In the standard model (the formulation of which will be explained in Section 1.5.1), the evolution of the Universe is influenced by its components. Two of the main components of this model are the so called dark matter and dark energy. Dark matter is needed because by assuming GR to be correct and accounting for all observable ordinary matter, many observations (e.g. rotation curves of galaxies, the total mass of galaxy clusters etc.) cannot be explained (see e.g. Peacock 1999). As the name suggests, the hypothetical dark matter neither emits nor interacts with electromagnetic radiation which is the reason that it is called "dark". And as mentioned in Section 1.4, dark energy was added to the components of the Universe in the standard model to explain the acceleration of the expansion. The main contributors to the mass-energy budget of the Universe in the standard model of cosmology are shown in Figure 1.4.

Around 95% of the components of the Universe in this model, i.e. dark matter and dark energy, have remained unknown after many years of investigation. A large fraction of research in physics, astrophysics and cosmology is devoted to understanding the nature of these two components. In addition, some researchers consider the mere need of these two "dark" components as a fundamental problem with the standard model of cosmology and its foundations, and seek alternative ways for explaining the observations without assuming the existence of one or both of these unknown components (Milgrom 1983; Bekenstein 2004; Mannheim 2006; Wiltshire 2009; Kroupa 2012; Koyama 2016).

1.5.1 Basic formulations

The Friedmann-Lemaître-Robertson-Walker metric

Assuming the CP, a metric can be written for an expanding Universe. The metric, in simple words, is a function that gives the distance between two points. In a 3 dimensional Euclidean space, the metric has the familiar form of $ds^2 = dx^2 + dy^2 + dz^2$. In special relativity where space and time are not separate any longer, this metric is generalized to the Minkowski's metric, $ds^2 = -c^2dt^2 + dx^2 + dy^2 + dz^2$, where c is the speed of light. In general relativity, the metric can take more complicated forms due to the

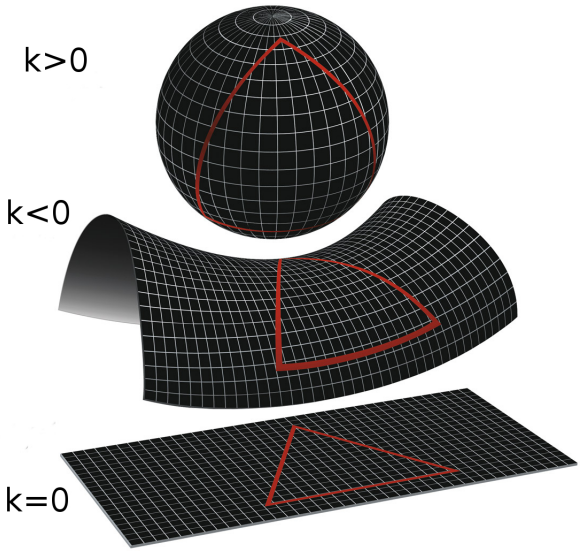

Figure 1.5: From top to bottom: positively curved (or closed) space, negatively curved (or open) space, and flat space. Credit: NASA / WMAP Science Team.

curvature of space at different points. However, the concept of distance in an expanding universe is not as trivial as in an static one. As mentioned in Section 1.2, Friedmann (1922) and Lemaître (1927) have presented a metric for studying the evolution of a homogeneous and isotropic expanding Universe. Later, Robertson (1929) and Walker (1933) have done further studies on that metric, hence, it is called the Friedmann-Lemaître-Robertson-Walker (FLRW) metric. Its simple form in a flat space is

$$ds^2 = -c^2dt^2 + a^2(t)[dx^2 + dy^2 + dz^2] \tag{1.3}$$

where a is called the scale factor which is a dimensionless parameter that describes how the spatial distance between two points changes with time due to the expansion of the Universe. The general form of the FLRW metric in the spherical coordinate system is:

$$ds^2 = -c^2dt^2 + a^2(t)[dr^2 + S_k^2(r)(d\theta^2 + \sin^2\theta d\phi^2)] \tag{1.4}$$

where (r, θ, ϕ) are the comoving spherical coordinates and

$$S_k(r) \equiv \begin{cases} k^{-1/2}\sin[k^{-1/2}r], & \text{for } (k > 0) \\ r, & \text{for } (k = 0) \\ (-k)^{-1/2}\sinh[(-k)^{-1/2}r], & \text{for } (k < 0) \end{cases} \tag{1.5}$$

in which k is the so called curvature parameter. For a flat space $k = 0$, for a positively curved (or closed) space $k > 0$, and for a negatively curved (or open) space $k < 0$. See Figure 1.5. The FLRW metric is a solution of the Einstein's Equation.

The Einstein equation

As mentioned above, in GR the contents of the space-time influences its geometry (or shape), and at the same time, the geometry of the space-time influences the contents of the space-time. In the previous section we presented the metric which represents the geometry of the space-time. Einstein's equation

relates the geometry to matter and energy:

$$G_{\mu\nu} \equiv R_{\mu\nu} - \frac{1}{2} g_{\mu\nu} R = -\frac{8\pi G}{c^4} T_{\mu\nu}. \tag{1.6}$$

In this equation, $g_{\mu\nu}$ is the metric of the space-time under consideration, $G_{\mu\nu}$ is the Einstein tensor, $R_{\mu\nu}$ is called the Ricci tensor which is a function of the metric and its derivatives, G is Newton's constant, and $T_{\mu\nu}$ is the energy-momentum tensor which describes the contents of the space-time.

The Friedmann equations

Given the CP assumption, we can assume that when studying the evolution of the Universe at very large scales, all its matter and energy content behaves like a perfect isotropic fluid.

Using this assumption and the FLRW metric in the Einstein's Equation, the so called Friedmann equations can be derived (see e.g. Dodelson 2003):

$$\left(\frac{\dot{a}}{a}\right)^2 = \frac{8\pi G}{3}\rho - \frac{kc^2}{a^2}, \tag{1.7}$$

$$\frac{\ddot{a}}{a} = -\frac{4\pi G}{3}\left(\rho + \frac{3p}{c^2}\right), \tag{1.8}$$

where ρ and p are the energy density and the pressure of the components of the Universe, respectively. These equations govern the expansion of a homogeneous and isotropic universe, i.e. the amount and type of the components of the Universe, represented by ρ and p, control the expansion of the Universe, represented by the scale factor, a, and its first, $\dot{a}$, and second, $\ddot{a}$, derivatives.

Cosmological parameters

In an expanding universe, the distance, d, between two points increases due to the expansion:

$$d = a(t)x \tag{1.9}$$

where x is the so called comoving distance between those two points. By taking the first derivative of this relation we have

$$\dot{d} = \dot{a}(t)x \tag{1.10}$$

where we ignored the peculiar motions that are negligible when considering large distances which means x is constant. The left hand side of this equation is just the recession relative velocity, v, between the two points and the left hand side can be rewritten using Eq. 1.9:

$$v = \frac{\dot{a}(t)}{a(t)} d. \tag{1.11}$$

By comparing this to Hubble's law in Eq. 1.2 we see that $H(t) = \frac{\dot{a}(t)}{a(t)}$. Using this, Friedmann's equation (i.e. Eq. 1.7) can be written as an equation for the evolution of the Hubble parameter or of the rate of the expansion of the Universe:

$$H^2(t) = \frac{8\pi G}{3}\rho(t) - \frac{kc^2}{a^2(t)} \tag{1.12}$$

Here it should be noted that Hubble's parameter is a function of time and its value at the present time is the so called Hubble constant, H_0.

Using Eq. 1.12, we can have a special value of the density (at any given time) for which the geometry of the Universe is flat, i.e. $k = 0$:

$$\rho_c(t) = \frac{3H^2(t)}{8\pi G}, \tag{1.13}$$

where $\rho_c(t)$ is known as the critical density. Using this, a density parameter, Ω, can be defined which is the ratio of the density and the critical density:

$$\Omega(t) = \frac{\rho(t)}{\rho_c(t)}. \tag{1.14}$$

The total energy density of the Universe is the sum of the densities of its individual components, i.e. $\rho(t) = \rho_m(t) + \rho_r(t) + \rho_\Lambda$, where the subscript m stands for matter, r stands for radiation and Λ stands for the cosmological constant which as mentioned earlier is one way of explaining the acceleration of the expansion of the Universe. Note that unlike the other two densities, ρ_Λ is constant with time.

By dividing both sides of Eq. (1.12) by $H^2(t)$ and using the definitions in Eqs. (1.13) and (1.14) we have:

$$1 = \Omega_m(t) + \Omega_r(t) + \Omega_\Lambda + \Omega_k(t) \tag{1.15}$$

for the density parameter of the different components. Here $\Omega_k(t) \equiv -\frac{kc^2}{a^2(t)H^2(t)}$ is called the "curvature density parameter".

However, what is usually measured is the present day value of these parameters. As the Universe expands, the energy density of matter decreases like $\rho_m \propto a^{-3}$ and that of the photons decreases like $\rho_r \propto a^{-4}$ (since each photon's energy scales as a^{-1}), the energy density of cosmological constant remains constant and Ω_k is proportional to a^{-2}. Using these relations and by dividing both sides of Eq. (1.12) by H_0^2 we have:

$$\frac{H^2(a)}{H_0^2} = \left[\Omega_m a^{-3} + \Omega_r a^{-4} + \Omega_\Lambda + \Omega_k a^{-2}\right], \tag{1.16}$$

where each Ω is the present value of the density parameter of each component of the Universe with $a = a(t)$, $\Omega_m = \Omega_m(t)$, $\Omega_r = \Omega_r(t)$, and $\Omega_k = \Omega_k(t)$. This is one of the useful equations for the evolution of the cosmic expansion as a function of the scale factor (time) and the cosmological parameters.

1.5.2 Standard candles and luminosity distance in the standard model

As mentioned in Section 1.4, observations of the cosmological standard candles led to the discovery of the acceleration of the expansion. In astronomy, a standard candle is referred to a class of objects whose luminosity is known due to some features possessed by the objects of that entire class. If the intrinsic luminosity L (energy per unit time) of an object is known, its distance d can be calculated by measuring its flux f (apparent brightness) and by using the inverse square law:

$$f = \frac{L}{4\pi d^2}, \tag{1.17}$$

which simply states that the flux (energy per unit time per unit area) of the radiation is inversely proportional to the square of the distance from the source. For example, if we have a number of exactly

similar light bulbs located at different distances from us, those with larger distance appear to be fainter than those closer to us. The faintness of the farthest bulb is not due to its intrinsic properties, but due to the fact that it is located at a larger distance. Therefore, if we can find a class of astronomical objects whose intrinsic luminosity can be known by some methods, and they can be identified by features other than their apparent brightness, we can estimate their distance from us using Eq. 1.17:

$$d_L = \left(\frac{L}{4\pi f}\right)^{\frac{1}{2}}. \tag{1.18}$$

d_L is the distance that the object appears to have based on its observed flux and is called the *luminosity distance*.

However, Eq. 1.17 holds for a static space, not an expanding one. Remember that flux is proportional to energy per unit time which means that in an expanding universe the observed flux is smaller due to two reasons:

1. The energy of the photons decreases due to the expansion. In an expanding universe the wavelength of the photons increases as the space expands, in other words:

$$\frac{\lambda_{emit}}{a_{emit}} = \frac{\lambda_{obs}}{a_{obs}} \rightarrow \lambda_{obs} = \frac{\lambda_{emit}}{a} \tag{1.19}$$

   where we used the convention that at the present epoch the scale factor is $a_{obs} = 1$ and we simply wrote a instead of a_{emit}. It is obvious that in an expanding universe always $a_{emit} < a_{obs}$ which means that $a < 1$. The longer the wavelength the smaller the energy, i.e. (observed energy) = (emitted energy) $\times\, a$.

2. Photons arrive less frequently. Due to the expansion of the space, the time difference, Δt, between two photon detections is larger than the time difference between their emission, i.e. (Δt at observation) = (Δt at emission) / a.

These two factors change the observed flux from f to $f \times a^2$ and consequently the distance would be measured to be:

$$d_L = \frac{1}{a} \times \left(\frac{L}{4\pi f}\right)^{\frac{1}{2}} = \frac{1}{a} \times d_{phys}, \tag{1.20}$$

where d_{phys} is the actual physical distance that the light has travelled. So in an expanding universe objects appear to have larger distance than they actually do.

Theoretically, the physical distance that light travels from the source to the observer can be calculated using Eq. 1.4 by remembering that for photons we have $ds = 0$:

$$c^2 dt^2 = a(t)^2 dr^2 \rightarrow d_{phys} \equiv r = c \int_{t_{emit}}^{t_{obs}} \frac{dt}{a(t)}. \tag{1.21}$$

Using Eq. (1.16) and remembering that $H = \frac{\dot{a}}{a}$ we can write the physical distance as a function of the scale factor:

$$d_{phys} = \frac{c}{H_0} \int_{a_{emit}}^{a_{obs}=1} \frac{da}{[\Omega_m a + \Omega_r + \Omega_\Lambda a^4 + \Omega_k a^2]}. \tag{1.22}$$

where we used the relation $\dot{a} = \frac{da}{dt}$ to replace dt by da. From Equations (1.1) and (1.19) we see that the relation between redshift and scale factor is:

$$a = \frac{1}{1+z}. \tag{1.23}$$

Using this relation (which gives $da = -dz/(1+z)^2$) and Eqs. (1.20) and 1.22), we can have a relation for the luminosity distance as a function of redshift which is an observable quantity:

$$d_L = \frac{c(1+z)}{H_0} \int_0^z \frac{dz'}{[\Omega_m(1+z')^3 + \Omega_r(1+z')^4 + \Omega_\Lambda + \Omega_k(1+z')^2]}. \tag{1.24}$$

Today's radiation density parameter is very small compared to that of the other components. In addition, CMB measurements yield $\Omega_k \approx 0$ (Planck Collaboration et al. 2015). These points reduce the above equation to

$$d_L = \frac{c(1+z)}{H_0} \int_0^z \frac{dz'}{[\Omega_m(1+z')^3 + \Omega_\Lambda]}, \tag{1.25}$$

for a flat Universe. In some books and papers a different but equivalent relation for d_L is given:

$$d_L = \frac{c(1+z)}{H_0} \int_0^z \frac{dz'}{[(1+z')^2(1+\Omega_m z') - z'(2+z')\Omega_\Lambda]}. \tag{1.26}$$

Magnitude and distance modulus

The astronomical magnitude, m, is a logarithmic scale for the brightness of astronomical objects. The difference between the apparent magnitudes of two objects with fluxes f_1 and f_2 is defined as:

$$m_1 - m_2 = -2.5 \log_{10}\left(\frac{f_1}{f_2}\right). \tag{1.27}$$

The brighter an object, the smaller its magnitude. The *absolute magnitude*, M, of an object is defined as its apparent magnitude if it is located at a distance of 10 pc[9]. Using Eqs. (1.17) and (1.27) we can write:

$$\mu \equiv m - M = 5 \log_{10}\left(\frac{d}{10\text{pc}}\right) = 5 \log_{10}\left(\frac{d}{\text{Mpc}}\right) + 25, \tag{1.28}$$

and μ is called the *distance modulus*. The theoretical distance modulus of a cosmological standard candle as a function of redshift and for given values of the cosmological parameters is:

$$\mu = 5 \log_{10}\left(\frac{d_L(z)}{\text{Mpc}}\right) + 25. \tag{1.29}$$

Type Ia supernovae as cosmological standard candles

Supernovae (SNe) are very luminous explosive events occurring in some stars. Due to their large luminosity, SNe can be detected in very distant galaxies. A subclass of supernovae, namely Type Ia Supernovae (SNe Ia), can (after some calibration and corrections) be used as standard candles for studying the expansion history of the Universe. Their lightcurves (change in brightness with time) and spectral

[9] 1 parsec (pc) ≈ 3.26 light years (ly)

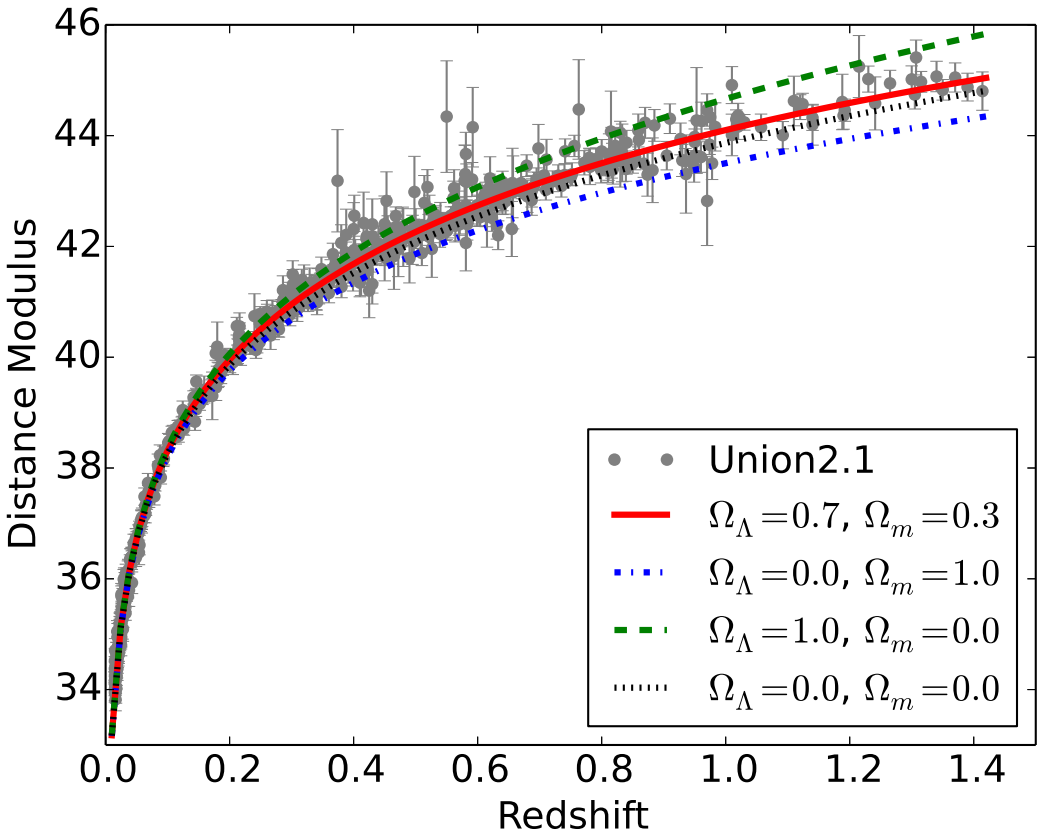

Figure 1.6: The distance modulus vs. redshift for different values of Ω_m and Ω_Λ. The data are from the Union2.1 compilation of the Supernova Cosmology Project (Suzuki et al. 2012). The best values for these data are $\Omega_m = 0.3$ and $\Omega_\Lambda = 0.7$.

features are very similar and this is linked to a threshold phenomenon in the physics of their explosions. The generally favoured theory for SNe Ia is the explosion of a white dwarf star after it accretes matter from a neighbouring star (in a binary system) and grows in mass to the Chandrasekhar mass limit above which a white dwarf cannot remain stable (Goobar & Leibundgut 2011).

Although it seems to be hard to apply a unique explosion mechanisms to all SNe Ia, the interesting similarity in their lightcurves allows for calibrating them after some "corrections". These corrections are related to the width of the lightcurve and the color, c, of a SN Ia event at its peak luminosity. The corrections modify the distance modulus of a SN Ia as follows:

$$\mu = m - M + \alpha x_1 - \beta c \tag{1.30}$$

where x_1 is the deviation from the average lightcurve shape (also called the stretch parameter) and α and β are the correction parameters for the stretch and color, respectively.

On the other hand, the redshifts of SNe Ia are obtained either from their own spectra or from that of their host galaxy. We can then compare the observed distance modulus versus redshift with the one predicted by the model (in Eq. 1.29) and obtain the best values of the cosmological parameters (or

compare the predictions of different cosmological models). Figure 1.6 shows a comparison of this relation for different values of Ω_m and Ω_Λ using Eqs. (1.26) and (1.29) and the Union2.1 data from the Supernova Cosmology Project (Suzuki et al. 2012).

1.5.3 Formation of structures and galaxies

In the standard model, formation of structure is heavily dependent on dark matter. According to this scenario, a few minutes after the Big Bang (and after inflation), the ordinary particles (electrons, protons and neutrons), dark matter and photons are distributed uniformly in space with only small density fluctuations (which caused the observed CMB temperature fluctuations). On the one hand, gravity causes the particles to move towards the positions where density is slightly higher than the average. The radiation pressure from the photons acts in the opposite way on the ordinary particles (also called baryons), not letting them to come together. But since dark matter particles by definition do not interact with photons, they can increase the over-densities. After the last scattering, baryons decouple from photons and can accumulate in the over-dense regions that have been already enhanced by dark matter particles. This grow in the density of the over-dense regions continues, and reaches a level at which the fist stars and small galaxies start to form. The first generation of small or *dwarf* galaxies form at this stage. Gravity causes small galaxies to move towards each other and to merge and form bigger galaxies. This scenario is also known as hierarchical structure formation. Figure 1.7 shows six snapshot of a computer dark matter simulation of the formation of a Milky-Way mass galaxy based on the hierarchical scenario. In the last snapshot (i.e. the bottom right panel) which corresponds to the present time, the formed massive galaxy is located at the centre of the image and a large number of small sub-structures (which are the places where dwarf galaxies are supposed to be formed) are distributed roughly isotropically around the central galaxy.

1.6 Successes and Problems of The Standard Model

The standard model provides explanations for the general statistical properties of the CMB (Planck Collaboration et al. 2015) and of the distribution of galaxies on the large-scale structure of the universe (Springel et al. 2006), the acceleration of the expansion through assuming the existence of dark energy or the cosmological constant, and other observations (see e.g. Scott 2006).

Despite these successes, the standard model is faced with some problems and challenges. Perhaps the most serious of them are dark matter and dark energy, about both of which we have no convincing physical understanding. None of the many experiments devoted to finding dark matter has detected a sign of it so far and no theoretical work yet can explain the nature and current value of the cosmological constant. Apart from these issues however, there are other thought-provoking problems on both large and small scales that are subject of active research. We briefly review the ones relevant to this thesis below. For more information on other interesting problems see Kroupa et al. (2012), Kroupa (2015), Buchert et al. (2015), and Bull et al. (2016).

1.6.1 Challenges on large scales: Some deviations from isotropy

The CMB radiation is observed to be very isotropic with only tiny temperature fluctuations of the order of 10^{-5}k. This already puts a strong constraint on possible deviations from isotropy in the early Universe. However, based on the Cosmological Principle, it is expected that also large scale features of the CMB to

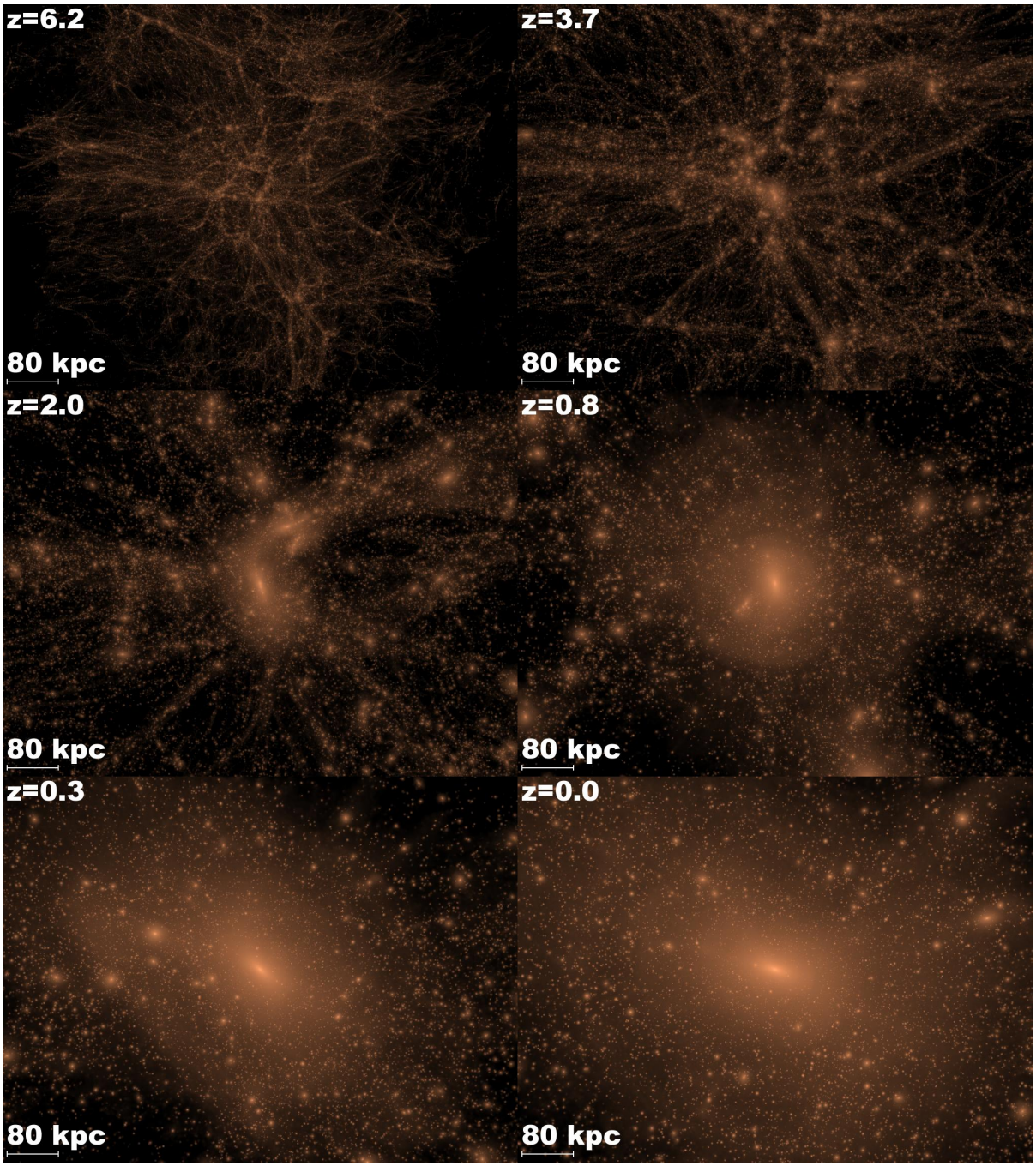

Figure 1.7: A computer simulation of the formation of a Milky Way sized halo in the standard model of cosmology. The top left image corresponds to the redshift $z = 6.2$ or more than 12 Gyr ago and the bottom right panel is at the present time. The brighter each point on the image, the higher is its projected density. Credit: the via lactea project (Diemand et al. 2008).

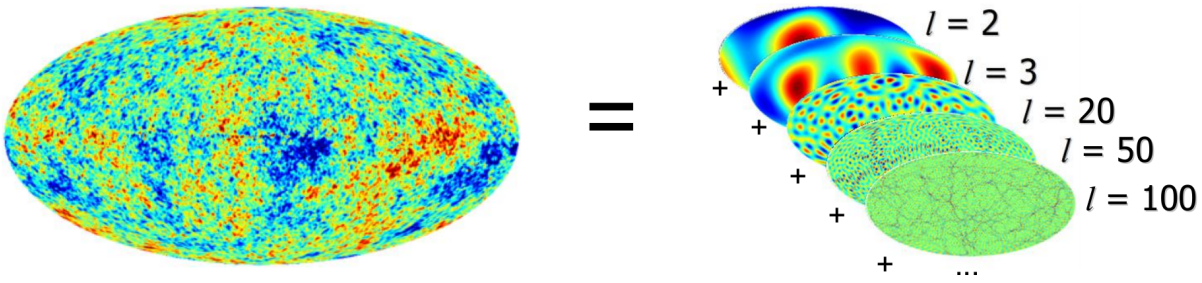

Figure 1.8: Decomposing the CMB fluctuations in to their different scales (multipoles) using spherical harmonics. Credit: Hans Kristian Eriksen.

be isotropic.

No cosmological model can predict the temperature of the CMB at a particular direction on the sky but the statistical properties of the CMB can be predicted and tested. Therefore, it is useful to describe the CMB fluctuations in terms of spherical harmonics:

$$\left(\frac{T(\theta,\phi)-\bar{T}}{\bar{T}}\right)=\sum_{l}\sum_{m=-l}^{l}a_{lm}Y_{lm}(\theta,\phi) \tag{1.31}$$

Here $T(\theta,\phi)$ is the temperature as a function of spherical coordinates θ and ϕ on the sky, and l and m describe each mode of the spherical harmonics. In general any function defined on the surface of a sphere can be expressed in terms of spherical harmonics. It is analogous to decomposing a two dimensional signal on a flat space into its Fourier modes. Similar to wave number k in Fourier space, l determines the scale of a mode while m determines its shape. The angular scale on the sphere corresponding to each l value is $\approx \frac{180^\circ}{l}$. By decomposing a CMB map using spherical harmonics, we can find the contribution of different scales to the overall fluctuations. $l=0$ corresponds to the *monopole* which is the average of the temperature across the sky[10] and is similar to the top panel of Figure 1.2. $l=1$ corresponds to the dipole term which is similar to the middle panel of the same figure. After subtracting the monopole (since only the fluctuations matter here), and removing the dipole (since, as explained in Section 1.3, it is considered to be solely due to our motion and hence is not of cosmological origin), we have the familiar CMB map[11] which is shown in Figure 1.3. Therefore, the modes related to $l \geq 2$ are cosmologically relevant. Figure 1.8 shows how a CMB map can be decomposed into the so called *multipole modes* each of which is related to a certain scale of the fluctuations. The *angular power spectrum* of the CMB is defined as the average of the expansion coefficients a_{lm} over m for each l:

$$C_l=\frac{1}{2l+1}\sum_{m=-l}^{l}|a_{lm}|^2 \tag{1.32}$$

and is a measure of the amplitude of the fluctuations as a function of scale.

After the observations by the *WMAP* satellite[12] some deviations from statistical isotropy in the CMB

[10] However, note that in Eq. (1.31) the average is already subtracted from the fluctuations and $l=0$ corresponds to a zero map.
[11] Assuming that the foreground radiation from the Milky Way is already removed.
[12] Wilkinson Microwave Anisotropy Probe (Bennett et al. 2003).

were discovered. Tegmark et al. (2003) reported that the CMB quadrupole (corresponding to $l = 2$) and the octopole (corresponding to $l = 3$) have unexpected planar structures and are significantly aligned with each other and the normals to their planes are close to the axis of the CMB dipole (see also Copi et al. 2004 and Schwarz et al. 2004). In a fully isotropic universe, these modes are expected to have random directions. Also, Eriksen et al. (2004) and Hansen et al. (2004) reported a hemispherical asymmetry in the angular power spectrum of the CMB aligned with the Ecliptic (see also Akrami et al. 2014 and Mukherjee et al. 2016). In particular, the power spectrum calculated in the hemisphere towards the Ecliptic North Pole is significantly lower than that in the opposite direction. The fact that these CMB "anomalies" were recently confirmed by the Planck Collaboration et al. (2014b) suggests that they are not artifacts caused by the detectors or data-reduction procedures. Still no convincing explanation for these observations are available and whether or not they should be considered as problems for the Cosmological Principle is still under debate (see e.g. Rassat et al. 2014a). Studying these asymmetries is an active field of research both on the data related and on the theoretical sides.

1.6.2 Problems on small scales: Observations of the Local Group of galaxies

Our Milky Way belongs to a galaxy group which is called the *Local Group* (LG). The two other most luminous galaxies in the LG are Andromeda (M31) and Triangulum (M33) which are also spiral galaxies like the Milky Way. The next luminous galaxy in the LG is the Large Magellanic Clouds (LMC) which is a satellite of the Milky Way. The rest of the known members of the LG are *dwarf galaxies*. They are very small and much less luminous. A large number of them are satellite galaxies of either Milky Way or M31, i.e. they orbit one of these two galaxies. Many of the dwarf satellite galaxies in the LG have been discovered in the past few years (e.g. by Bechtol et al. 2015). Studying the properties of satellite galaxies and their spatial distribution around their hosts is one of the important ways of testing galaxy formation and evolutions scenarios.

Although the hierarchical structure formation can explain the large scale distribution of galaxies and some properties of galaxies and galaxy clusters (Vogelsberger et al. 2014), it has problems with explaining some of the properties of the LG:

- **The missing satellite problem**
  The predicted number of satellite galaxies in the Local Group is an order of magnitude larger than the number of observed ones (Klypin et al. 1999; Moore et al. 1999; Bullock 2010; Kravtsov 2010).

- **The too big to fail problem**
  The predicted most massive subhaloes of the Milky Way are too dense to be consistent with any of the bright satellites of our Galaxy (Boylan-Kolchin et al. 2011).

- **The observed disk of satellites**
  The distribution of satellite galaxies around a Milky Way-type galaxy is predicted to be almost isotropic (see the lowest-right panel of Figure 1.7). However, the satellites of the Milky way are observed to be located in a thin disk and almost perpendicular to the plane of the Milky Way (Kroupa et al. 2005; Pawlowski et al. 2012). In addition, most of these satellites are rotating the Milky Way in a common direction. A similar structure is also observed around the Andromeda galaxy (Ibata et al. 2013).

Another interesting feature of the LG is that the number of the satellite galaxies of the Milky Way, M31, and M33 is found to be correlated with the mass of their bulges (Kroupa et al. 2010). In the hierarchical structure formation model, it is the circular velocity of the galaxies (a proxy to their dark matter halo mass) which is expected to be correlated with the number of the satellites (the more massive the dark matter halo, the larger the number of the satellites). On the other hand, if the majority of the satellite galaxies are of tidal origin (i.e. the result of interactions between two galaxies), then not only the above mentioned correlation, but also the disk of the satellites would be a natural phenomena (Kroupa 2015).

A considerable fraction of research in small scale cosmology is devoted to understanding and solving these problems (e.g. by considering complex baryonic physics, Del Popolo 2014). However, convincing solutions have not emerged yet.

1.7 Contributions of This Thesis

1.7.1 Probing large scale isotropy

A major part of this thesis is devoted to testing the assumption of isotropy derived from the Cosmological Principle. Since the reported deviations from isotropy in the CMB (Section 1.6.1) have been observed by two completely different instruments, it is less likely that it goes away by refining data analysis methods. Therefore, it is important to check if an anisotropy similar to that documented in the CMB is detected in other observable properties of the Universe. This would then be a serious violation of the Cosmological Principle. The importance of probing isotropy can be viewed from three different perspectives:

- If no significant deviation from isotropy is found, we will place more confidence in the Cosmological Principle (although it does not mean that we should stop testing it further).
- If we find deviations from isotropy in a particular data set, this can also be a hint of possible systematic issues with that data set rather than of a violation of the Cosmological Principle. Having systematic-free data is always crucial for different studies.
- If a significant deviation from isotropy is consistently found in different extragalactic observables, then we would need to reconsider the assumption of isotropy. This would be a major paradigm change in cosmology and for the understanding of our place in the Universe.

All the properties of an isotropic Universe are expected to be isotropic at large-enough scales. The scale depends on the cosmological model. Marinoni et al. (2012) quantified the scale above which the distribution of galaxies become statistically isotropic to be around 150 Mpc.

In Chapter 2 of this thesis, we probe the isotropy of the cosmic acceleration by studying the magnitude-redshift relation of SNe Ia data in different directions in the sky. We only use SNe Ia at redshifts $z \geq 0.2$ (corresponding to distances $\gtrsim$800 Mpc). The contents of this chapter have been published as "Probing the isotropy of cosmic acceleration traced by Type Ia supernovae" in Javanmardi et al. (2015). In Chapter 3 we test the isotropy of the distribution of morphological types of more than 60,000 galaxies in the Local Universe out to around 200 Mpc. The content of this chapter have been published as "Anisotropy in the all-sky distribution of galaxy morphological types" in Javanmardi & Kroupa (2017).

1.7.2 Towards addressing the small scale problems outside the Local Group

The small scale problems explained in Section 1.6.2 are mostly observed in the Local Group. Although the observations in the Local Group are among the best extragalactic observations due to the simple fact that the distances involved are smaller, the LG might be a peculiar system and these issues might not exist in other galaxy groups[13]. Therefore, it is vital to check if the same features exist around other galaxies similar to the Milky Way and the Andromeda. However, since dwarf satellite galaxies are intrinsically very faint objects, the number of known objects of this type outside the LG is still small and this makes it hard to test the small scale problems outside the Local Group. Since large galaxy surveys like the Sloan Digital Sky Survey (SDSS) scan the sky very quickly (spending only some minutes on each part of the sky), they can only detect the bright galaxies.

To search for satellite galaxies around massive galaxies, a wide field of view and very long-exposure images are necessary. However, it is very hard to have access to hours of observing time on a big telescope for such searches. Interestingly, in the past years the development of very good detectors and imagers made it possible to obtain very deep images (given enough exposure time) using even small telescopes.

A part of my PhD studies was therefore devoted to launching the Dwarf Galaxy Survey with Amateur Telescopes (DGSAT) which uses long exposure images obtained by a network of amateur astronomers to search for low surface brightness galaxies around nearby Milky-Way-type galaxies. Chapter 4 explains this ongoing survey and its first findings. The contents of this paper have been published as "DGSAT: Dwarf Galaxy Survey with Amateur Telescopes I. Discovery of low surface brightness systems around nearby spiral galaxies", in Javanmardi et al. (2016).

[13] However, even if this were to be the case, it would nevertheless be difficult to understand in the framework of the standard model of cosmology.

CHAPTER 2

Probing the isotropy of cosmic acceleration traced by Type Ia supernovae

Abstract

We present a method to test the isotropy of the magnitude-redshift relation of Type Ia Supernovae (SNe Ia) and single out the most discrepant direction (in terms of the signal-to-noise ratio) with respect to the all-sky data. Our technique accounts for possible directional variations of the corrections for SNe Ia and yields all-sky maps of the best-fit cosmological parameters with arbitrary angular resolution. To show its potential, we apply our method to the high redshift SNe Ia from the recent Union2.1 compilation, building maps with three different angular resolutions. We use a Monte Carlo method to estimate the statistical significance with which we could reject the null hypothesis that the magnitude-redshift relation is isotropic based on the properties of the observed most discrepant directions. We find that, based on pure signal-to-noise arguments, the null hypothesis cannot be rejected at any meaningful confidence level. However, if we also consider that the strongest deviations in the Union2.1 sample closely align with the dipole temperature anisotropy of the cosmic microwave background, we find that the null hypothesis should be rejected at the $95-99$ per cent confidence level, slightly depending on the angular resolution of the study. If this result is not due to a statistical fluke, it might either indicate that the SN data have not been cleaned from all possible systematics or even point towards new physics. We finally discuss future perspectives in the field for achieving larger and more uniform data sets that will vastly improve the quality of the results and optimally exploit our method.

Note: This chapter is a reprint of a paper of the same title, published in The Astrophysical Journal. The reference is: **B. Javanmardi**, C. Porciani, P. Kroupa, and J. Pflamm-Altenburg, 2015, ApJ, 810, 47.

2.1 Introduction

In 1998, the luminosity-redshift relation (Hubble diagram) of a few tens of Type Ia supernovae (SNe) provided the evidence base for the accelerated expansion of the universe (Riess et al. 1998; Perlmutter et al. 1999). Since then, major efforts have been made to increase the sample size, extend it to higher redshift, and refine the observational and data-reduction techniques. Current datasets already include several hundreds of objects but the quest for dark energy drives copious activity in this field.

The control of systematic errors is the key to making the study of SNe Ia a prime cosmological tool. Suzuki et al. (2012) state that systematic uncertainties already dominate over the statistical ones in the determination of the cosmological parameters. Given that systematics will become even more important in the future, a careful scrutiny of all the possible sources of methodological bias is crucial. In this paper, we focus on the spatial isotropy of the Hubble diagram traced by type Ia SNe. The standard cosmological model is rooted in the assumption that the Universe is homogeneous and isotropic on large scales. Hence, SNe Ia are expected to (statistically) obey the same dimming relation in all directions. There are, however, several phenomena that could introduce anisotropies with different characteristic scales and amplitudes in the observed expansion rate. To name a few: dust absorption (both in the Milky Way and in the galaxies hosting the SNe), redshift-space distortions due to large-scale motions, weak gravitational lensing, the presence of large-scale structures and contamination of the SNe Ia samples. Detecting these effects and correcting for them would ultimately lead to tighter and less biased constraints on the cosmological parameters.

At the same time, it is healthy to scrutinise the validity of the standard model of cosmology (Kroupa 2012; Kroupa et al. 2012; Kroupa 2015; Koyama 2016) and its fundamental assumptions, namely those of the cosmological principle. Ruling out cosmic isotropy with high statistical confidence would lead to a major paradigm shift especially if such a conclusion is confirmed by multiple datasets affected by different systematics. In this respect, the analysis of temperature anisotropies in the Cosmic Microwave Background (CMB) has dominated the scene in the last decade. The WMAP satellite detected a few large-scale "anomalies" that somewhat deviate from the expectations of the standard model that best fits the data on smaller scales (Tegmark et al. 2003; Eriksen et al. 2004; Hansen et al. 2009; Copi et al. 2010a). In brief, the quadrupole and octopole terms are surprisingly planar and there is a significant alignment between them. Moreover, their normals lie close to the axis of the CMB dipole. This discovery generated a long lasting debate in the literature concerning whether or not these features are genuine signs of new physics.

Alternatively they could be due to the influence of data processing, to the imperfect removal of foreground contaminants and secondary astrophysical effects (Rassat et al. 2014b), as well as to a statistical fluke (Bennett et al. 2011). The Planck satellite recently confirmed the existence of these alignments (Planck Collaboration et al. 2014b) suggesting that they are not artifacts of the data-reduction pipelines. A satisfactory explanation for the origin of these asymmetries is still not available.

The isotropy of the Hubble diagram for SNe Ia has been repeatedly tested. Kolatt & Lahav (2001) used 79 SNe from Riess et al. (1998) and Perlmutter et al. (1999) to perform localized fits within an opening angle of 60° around random directions. After expanding the best-fitting cosmological parameters in low multipoles, they found that no dipole anisotropy was statistically significant. Subsequent studies mainly adopted two methods: either they compared Hubble diagrams for pairs of hemispheres and looked for the most discrepant hemispheric cut (Hemispherical Comparison, e.g. Schwarz & Weinhorst 2007) or fit a dipole angular distribution (Dipole Modulation Fitting, e.g. Cooke & Lynden-Bell 2010). Other authors looked for angular correlations in SN magnitudes (Blomqvist et al. 2008) or analyzed the magnitude-redshift relation in the context of anisotropic cosmological models (Koivisto & Mota 2008; Campanelli et al. 2011). Low-redshift samples were used to estimate the direction and amplitude of

the local bulk flow (Bonvin et al. 2006; Schwarz & Weinhorst 2007; Colin et al. 2011; Turnbull et al. 2012; Rathaus et al. 2013; Feindt et al. 2013; Kalus et al. 2013; Appleby & Shafieloo 2014b; Appleby et al. 2015). At the same time, several authors analysed higher-redshift data to look for large-scale anisotropies (Schwarz & Weinhorst 2007; Gupta & Saini 2010; Cooke & Lynden-Bell 2010; Antoniou & Perivolaropoulos 2010; Mariano & Perivolaropoulos 2012; Cai et al. 2013; Li et al. 2013; Campanelli et al. 2011; Zhao et al. 2013; Heneka et al. 2014; Wang & Wang 2014; Yang et al. 2014; Chang & Lin 2015; Jiménez et al. 2015), which is also the aim of our work. Statistically significant deviations have been detected at low redshift (Schwarz & Weinhorst 2007), while no high-redshift study could rule out isotropy at more than 2 Gaussian standard deviations, σ.

In this paper, we present a simple but powerful method to test the isotropy of the luminosity-redshift relation for SNe Ia. Contrary to most previous studies, our analysis neither searches for hemispheric asymmetries and dipolar patterns nor does it use any other template anisotropic configuration. For each direction on the celestial sphere $\hat{r} \in S^2$, we derive a set of cosmological parameters by considering only the SNe that lie within an angle θ from $\hat{r}$. We then build maps of these "local cosmological parameters" with different values of θ and identify the directions associated with the most significant anisotropies taking into account that the number of datapoints used in the fit fluctuates from one direction to another. For completeness, we consider that the correction for the distance modulus of SNe Ia might also depend on $\hat{r}$ due, for instance, to dust extinction. Therefore, our strategy is able to detect anisotropies generated both by physical effects and by systematics. Even though our method is best suited for the large SN samples with nearly uniform sky distribution that will become available in the next decade, we provide an example of its potential by applying it to the Union2.1 SN Ia compilation (Suzuki et al. 2012) from the Supernova Cosmology Project (SCP). We limit our study to redshifts $z \geq 0.2$ in order to minimize the influence of local inhomogeneities and bulk flows.

The rest of this paper is organised as follows. Section 2.2 describes the main properties of the Union2.1 sample. Our method of analysis is introduced in Section 2.3. Results are presented and critically discussed in Section 2.4. Finally, we conclude in Section 2.5.

2.2 Data

The Union2.1 compilation (Suzuki et al. 2012) collects data for 580 SNe Ia in the redshift range of $0.015 \leq z \leq 1.414$. It combines entries from 19 datasets uniformly analysed after adopting strict lightcurve quality cuts and the SALT2 lightcurve-fitter (Guy et al. 2007). The Union2.1 catalog has been built for dark-energy science and updates the previously released Union (Kowalski et al. 2008) and Union2 (Amanullah et al. 2010) compilations. In particular, it contains 14 new SNe discovered in the HST Cluster Supernova Survey (a survey run by the SCP) that pass the Union2 selection cuts. Ten of these SNe are at $z > 1$ which makes the Union2.1 sample ideal for studying isotropy out to the largest possible distances.

The Union2.1 catalog provides five entries for each SN, specifically: name, redshift (CMB centric), distance modulus, error in the estimate of the distance modulus, and the probability that the SN was hosted by a low-mass galaxy. We obtained the coordinates for all the SNe Ia in the compilation either from the NASA/IPAC Extragalactic Database (NED)[1] or directly from the SuperNova Legacy Survey (SNLS) data release (Astier et al. 2006). The sky distribution of Union2.1 SNe is plotted in Figure 2.1. The angular position of each SN is marked by a symbol which has been colour-coded based on redshift. Several features are immediately apparent in the image. First, there are only a few SNe close

[1] The NASA/IPAC Extragalactic Database (NED) is operated by the Jet Propulsion Laboratory, California Institute of Technology, under contract with the National Aeronautics and Space Administration.

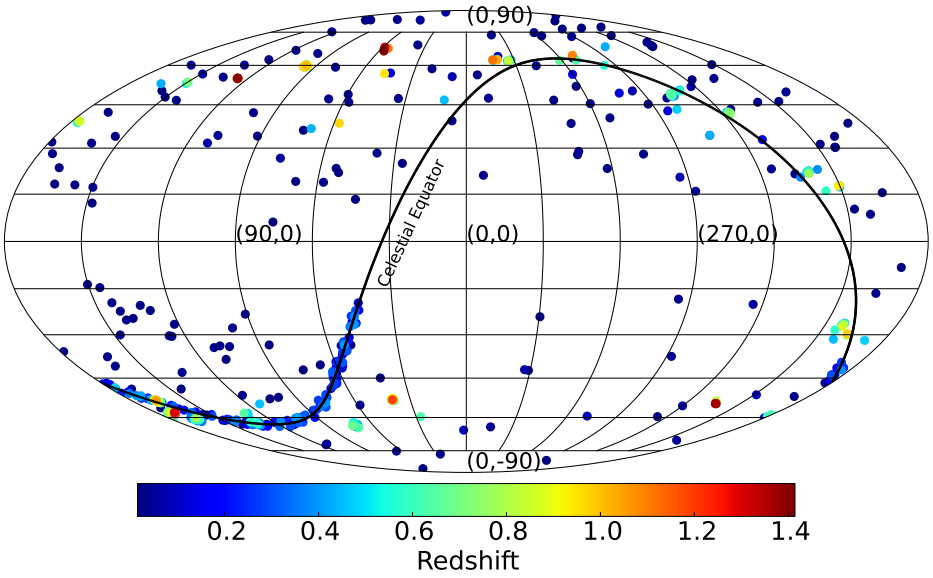

Figure 2.1: Mollweide projection map of the Union2.1 SNe Ia in the Galactic coordinate system. Each circle corresponds to the position of a SN Ia on the sky and is colour-coded based on the SN Ia redshift. The black solid curve indicates the celestial equator.

to the galactic plane. Second, an arc-like region in the southern hemisphere is much more densely populated than the rest. This is the footprint of the Sloan Digital Sky Survey-II (SDSS-II) SN search and corresponds to the southern equatiorial stripe (Stripe 82, with coordinates $-50 < RA < 59$ and $-1.25 < DEC < 1.25$) which has been imaged repeatedly with broad wavelength coverage and also been subject to extensive spectroscopic studies (Kessler et al. 2009). Finally, high-redshift SNe are very sparsely distributed and rare which is also evident from the redshift distribution of the Union2.1 SNe shown in Figure 2.2.

2.3 Method

As mentioned in the Introduction, previous studies on the isotropy of the luminosity-redshift relation of SNe Ia have mainly searched for dipolar anisotropies or hemispheric asymmetries. In this section, we introduce a more general method that does not assume any particular form of the anisotropy.

2.3.1 Cone Analysis

Let us consider a particular direction on the sky, $\hat{r}$, with Galactic longitude l and latitude b. In order to single out a finite region surrounding $\hat{r}$, we consider a cone with apex angle 2θ subtending a solid angle of $\Omega_{cone} = 2\pi(1 - \cos\theta)$ sr on the celestial sphere. The apex of the cone is located at the centre of the Galactic coordinate system and its axis of symmetry points towards $\hat{r}$. After isolating the SNe Ia contained within the cone, we build their magnitude-redshift relation and derive "local cosmological parameters" by fitting a theoretical relationship to it (see Section 2.3.2 for details). We then vary the cone direction $\hat{r}$ making sure that we cover the whole sky. For convenience, we move $\hat{r}$ along the pixel centers of a HEALPix[2] grid (Górski et al. 2005).

[2] Hierarchical Equal Area isoLatitude Pixelization, http://healpix.sourceforge.net

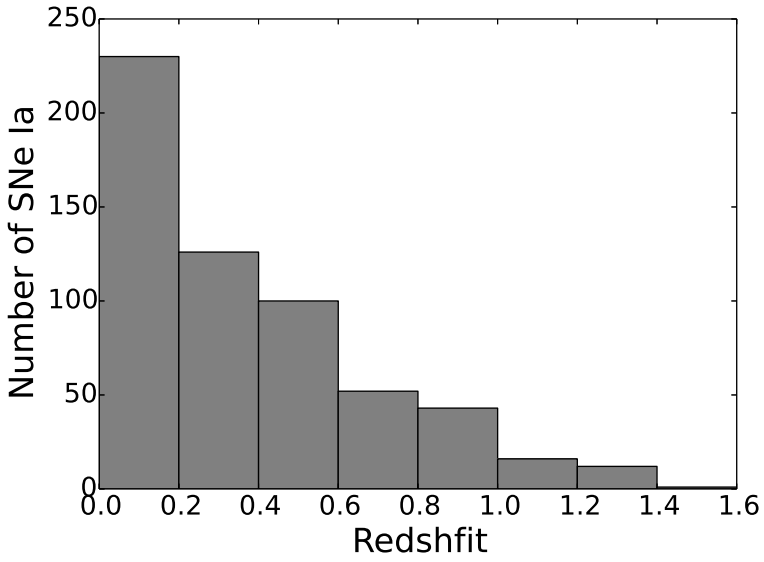

Figure 2.2: Redshift distribution of Union2.1 SNe.

For the application of the method to the Union2.1 data, we repeat the analysis using three different opening angles: $\theta = \frac{\pi}{2}$ (hemispheres), $\frac{\pi}{3}$ and $\frac{\pi}{6}$. We use a HEALPix grid with 192 pixels so that the solid angle subtended by each pixel is much smaller than that subtended by the cones.

2.3.2 Formulation

Global fit

SNe Ia are not perfect standard candles, their peak brightness correlates with their color, the light-curve width and the mass of the host galaxy. In the Union2.1 sample, individual lightcurves are analyzed with the SALT2 fitter which provides estimates for three parameters: the peak magnitude, m_{obs}, in the rest-frame B band, the deviation, x_1, from the average light-curve shape and the deviation, c, from the mean $B-V$ color. The color and light-curve-shape corrected distance modulus is then written in terms of four unknown parameters (α, β, δ and M_B) so that

$$\mu_B = m_{obs} + \alpha \cdot x_1 - \beta \cdot c + \delta \cdot P_{host} - M_B, \tag{2.1}$$

where M_B is the absolute B-band magnitude at maximum of a SN Ia and P_{host} denotes the probability that the SN Ia is hosted by a galaxy with stellar mass $M_* < 10^{10} M_\odot$. This probability is estimated differently for untargeted and targeted surveys.

In the context of the theory of general relativity, homogeneous and isotropic universes are described by Friedmann-Lemaître-Robertson-Walker models. For simplicity we only consider flat models in which the density parameters for the matter and the cosmological constant satisfy the relation $\Omega_m + \Omega_\Lambda = 1$. Following standard practice, we write the magnitude-redshift relation of SNe Ia in terms of the distance modulus

$$\mu(z) = 5 \log_{10} d_L(z, \Omega_\Lambda) + 5 \log_{10} \left(\frac{D_H}{\mathrm{Mpc}} \right) + 25 \,, \tag{2.2}$$

where

$$d_L = \int_0^z \frac{(1+z)\,dq}{\left[(1+q)^2(1+\Omega_m q) - q(2+q)\Omega_\Lambda\right]^{1/2}} \tag{2.3}$$

is the dimensionless "Hubble-constant-free" luminosity distance and $D_H = c/H_0$ is the Hubble radius defined in terms of the speed of light and the present-day value of the Hubble constant.

Classically, the SN data are fitted with a cosmological model assuming Gaussian errors and following a maximum likelihood approach (e.g. Astier et al. 2006). For N Type Ia SNe, this corresponds to minimising the target function

$$\chi^2 = \mathbf{V}^T\,\mathbf{C}^{-1}\,\mathbf{V} \tag{2.4}$$

where $\mathbf{V}$ is a N-dimensional vector with elements $V_i = \mu_{B,i}(\alpha,\beta,\delta,M_B) - \mu(z_i;H_0,\Omega_\Lambda)$ and $\mathbf{C}$ is the covariance matrix of the errors in the observed distance moduli. For the Union compilations, this matrix is publicly available. Its off-diagonal elements include several contributions due to the light-curve fits, galactic extinction, gravitational lensing, peculiar velocities and sample-dependent systematics. The nuisance parameters α,β,δ and M_B are fitted simultaneously with the cosmological parameters. Actually, the best-fit values for M_B and H_0 are completely degenerate as only the combination $\mathcal{M} = M_B + 5\log_{10}(D_H/\mathrm{Mpc})$ appears in eq. (2.4). Using the whole data set gives the following best-fit values (Suzuki et al. 2012) $\alpha = 0.121, \beta = 2.47, \delta = -0.032$, and $M_B = -19.321$ (for $H_0 = 70$ km s^{-1}Mpc^{-1}).

Local fits

The parameters α,β and δ describe correlations between different SN observables and might vary for the different surveys of a compilation. Karpenka et al. (2015) found inconsistencies between the values of these correction parameters in the Union2 catalog. In order to account for possible direction-dependent systematics, when we consider localized sub-samples of the Union2.1 data, we should in principle allow them to vary freely. However, this would require knowledge of the covariance between m_{obs}, x_1 and c for individual SNe. Regrettably this information is not provided in the Union2.1 catalog. We therefore adopt a simplified approach by assuming a constant correction, μ_{cor}, for the distant modulus of all the SNe lying within a cone. In other words, we keep the quantities α,β,δ and $\mathcal{M}$ fixed at their global best-fit value (hereafter denoted with a hat) but we write

$$V_i = \mu_{B,i}(\hat{\alpha},\hat{\beta},\hat{\delta},\hat{M}_B) - 5\log_{10} d_L(z_i;\Omega_\Lambda) - \Delta_0 \tag{2.5}$$

with $\Delta_0 = 5\log_{10}(cH_0^{-1}) + 25 - \mu_{cor}$. Note that Δ_0 accounts for both an "anisotropic Hubble constant" and for the mean effect of variations in α,β,δ and M_B due to systematic errors. We are left with a two-dimensional problem. For each pixel on the sky, we then determine the best-fitting values of the cosmological parameter Ω_Λ and of the correction parameter Δ_0 by minimizing the χ^2 target function (covariances are extracted from $\mathbf{C}$ after identifying the SNe in the cone). However, the model parameters anticorrelate: directions associated with large values of Ω_Λ provide low values of Δ_0 (and viceversa). In order to minimise this effect, we use the luminosity distance, d_L, evaluated at the mean redshift of the sample ($\bar{z} = 0.36$) as a pivot point and define

$$V_i = \mu_{B,i}(\hat{\alpha},\hat{\beta},\hat{\delta},\hat{M}_B) - 5\log_{10}\left(\frac{d_L(z_i;\Omega_\Lambda)}{d_L(\bar{z};\Omega_\Lambda)}\right) - \Delta \tag{2.6}$$

where $\Delta = \Delta_0 + 5\log_{10} d_L(\bar{z};\Omega_\Lambda)$ and Ω_Λ are our free parameters.

Table 2.1: All-sky fitting results. Best-fit parameters and the corresponding reduced chi-square, χ^2/ν, for the entire Union2.1 sample and for two redshift subsets. The quoted uncertainties correspond to $\Delta\chi^2 = 1$.

	Ω_Λ	Δ (mag)	χ^2/ν
All SNe	$0.70^{+0.04}_{-0.04}$	$41.428^{+0.028}_{-0.031}$	0.94
$z \geq 0.2$	$0.68^{+0.06}_{-0.05}$	$41.443^{+0.052}_{-0.049}$	0.94
$z < 0.2$	$0.62^{+0.18}_{-0.19}$	$41.380^{+0.040}_{-0.041}$	0.93

2.4 Results

2.4.1 All-sky fit

To test the consistency of our approach with previous studies, we first perform an all-sky fit. Results are shown in Table 2.1 for the entire Union2.1 sample and for two sub-sets including the SNe Ia with redshift smaller and larger than $z = 0.2$ (in this paper, uncertainties on the value of single parameters always correspond to $\Delta\chi^2 = 1$). Our results are in excellent agreement with the analysis in Suzuki et al. (2012) who found $\Omega_\Lambda = 0.705^{+0.040}_{-0.043}$ (see their Table 7). Also note that setting $\mu_{cor} = 0$, $H_0 = 70\ \mathrm{km\,s^{-1}Mpc^{-1}}$ and $M_B = -19.321$ corresponds to $\Delta_0 = 43.159$ mag which gives $\Delta = 41.419$ mag for $\Omega_\Lambda = 0.705$ and $\bar{z} = 0.36$.

2.4.2 Cone analysis

Ω_Λ maps

Sky maps of the best-fit values for Ω_Λ (left) and Δ (right) are shown in Figure 2.3 for three different cone opening angles (from top to bottom: $\theta = \frac{\pi}{2}$, $\frac{\pi}{3}$ and $\frac{\pi}{6}$ radians). These have been obtained using all the Union2.1 SNe with redshift $z \geq 0.2$. White pixels indicate the directions (mostly located around the Galactic equator) in which the corresponding cone contains less than 25 SNe Ia. These directions are excluded from all statistical analyses because they are associated with extremely large errors in the fitted parameters. Of course their number increases with decreasing the opening angle of the sampling cone. Similarly, the size of fluctuations in the best-fit values for Ω_Λ and Δ increases with reducing θ.

Most discrepant directions

Although Figure 2.3 gives a first visual impression of the local best-fit parameters, it does not take into account the non-uniform sky coverage of the Union2.1 data set. For a given opening angle, different directions on the celestial sphere are generally associated with very different numbers of SNe Ia. This strongly influences the uncertainty of the best-fit values.

In order to single out the most discrepant directions in a statistically meaningful way, we assume the null hypothesis that the Universe follows the cosmological principle and there are no angle-dependent systematic effects plaguing the Union2.1 sample. For each pixel we then evaluate the χ^2 target function fixing the free parameters at the values $\hat{\Omega}_\Lambda = 0.70$ and $\hat{\Delta} = 41.428$ that provide the best-fit solution for the complete Union2.1 sample. However, only the SNe within the sampling cone are used to calculate the χ^2 value that we denote by $\hat{\chi}^2$. Finally, we estimate the probability P that random noise could generate a χ^2 value exceeding $\hat{\chi}^2$. Assuming Gaussian errors, this probability coincides with the cumulative chi-square

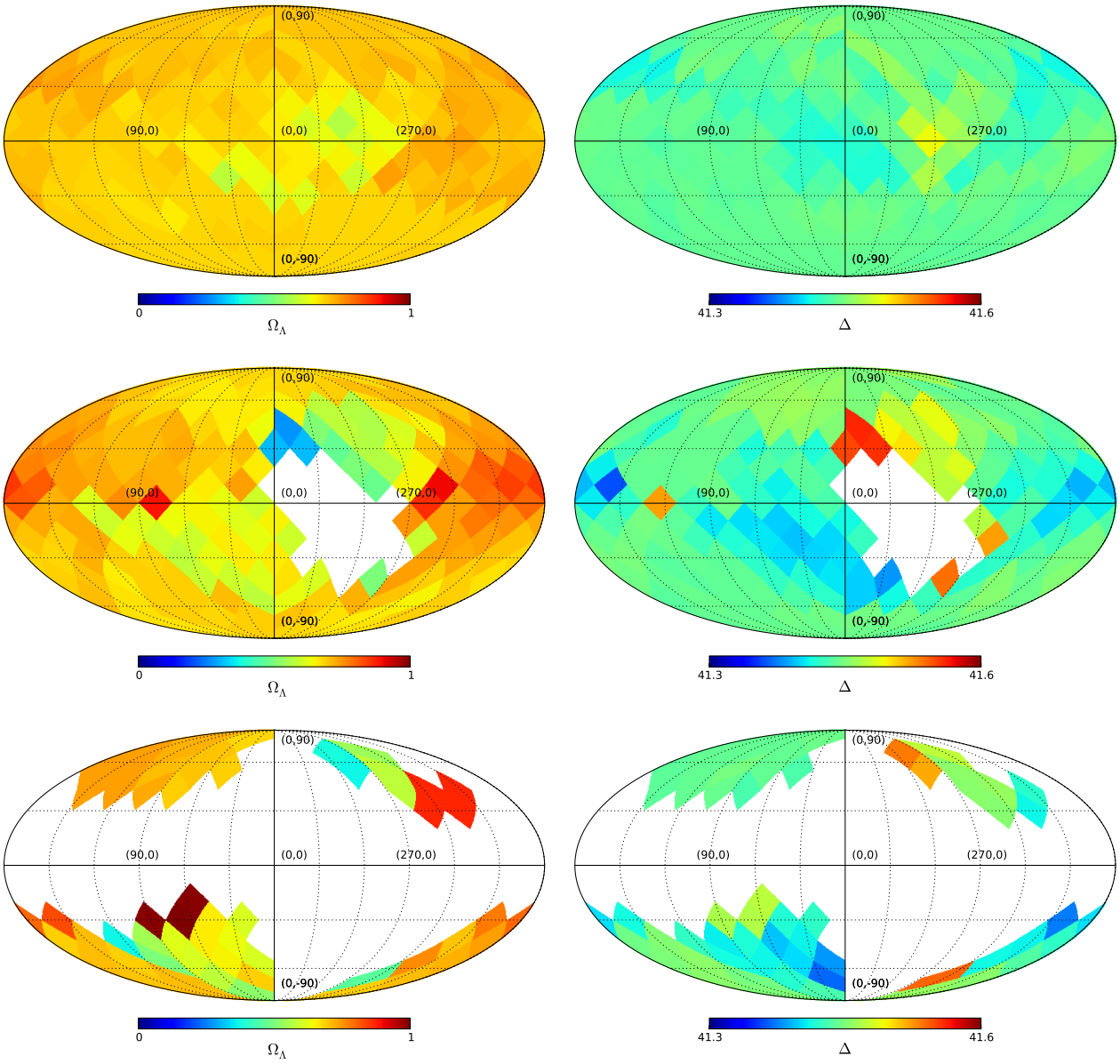

Figure 2.3: Best-fit values for Ω_Λ (left) and the correction parameter Δ (right) in different directions on the sky. Each pixel shows results that have been determined considering the magnitude-redshift relation of all Union-2.1 supernovae with redshift $z \geq 0.2$ that lie within an angle θ from the pixel center. The cone opening angle θ assumes the values $\frac{\pi}{2}$ (top), $\frac{\pi}{3}$ (middle) and $\frac{\pi}{6}$ (bottom). The white regions indicate the directions for which the sampling cone contains less than 25 SNe Ia.

distribution function evaluated at $\hat{\chi}^2$:

$$P = \frac{1}{2^{\nu/2}\Gamma(\nu/2)} \int_{\hat{\chi}^2}^{\infty} t^{\nu/2-1} e^{-t/2} dt \,, \tag{2.7}$$

where ν is the number of degrees of freedom – i.e. the number of SNe Ia used in the fitting procedure minus two (the number of free parameters). We adopt the P value as a measure of how well the all-SNe best-fit parameters also describe the SN data in a specific direction on the sky. Consequently we identify the most discrepant direction (i.e. the direction showing the most statistically significant deviation from isotropy) with the pixel showing the smallest P value. It is worth stressing that this is not necessarily the direction in which the Universe (or the SN data) might present the strongest intrinsic anisotropy but only the direction in which, given the current data, we can measure the most meaningful deviation in terms of the signal-to-noise ratio.

Maps of the P value are plotted in Fig. 2.4 for the three different cone opening angles. The most (second-most) discrepant directions are highlighted with a star (circle) in each panel. Further information is provided in Table 2.2 which gives the P value, the coordinates and the number of SNe Ia associated with the most and the second-most discrepant directions together with the local best-fit parameters. The motivation for showing two directions per map is as follows: i) the difference between their P-values is small (see Table 2.2), ii) the covariance matrix provided by the SCP is likely to be a noisy estimate, and iii) neglecting off-diagonal covariances switches the order between these directions for $\theta = \frac{\pi}{3}$.

Intriguingly, the most discrepant directions obtained with the three cone opening angles lie close to each other. Also the best-fit parameters are quite similar (let us not forget, however, that the maps with different θ are not independent as they use the same SNe and that there is significant overlap between the most discrepant cones). In Figure 2.5 we compare the formal[3] 1σ confidence regions ($\Delta\chi^2 \leq 2.30$) obtained from the all-SNe fit against those derived from the local fits along the most discrepant directions. In all cases, the tension between the local and the global fits is marginal and the formal 1σ regions always overlap.

Visual inspection of Figure 2.4 shows a striking contrast between the P values measured in the Northern and the Southern Galactic Hemispheres (hereafter NGH and SGH, respectively), although there is no tension between the luminosity-distance relation in the two hemispheres (see Table 2.3). The discrepancy in the P values is mainly due to the fact that the Union2.1 uncertainties in the distance-moduli are on average 30 per cent larger in the NGH. Consequently, the reduced chi-square $\hat{\chi}^2/\nu$ tends to be smaller in the NGH although there are many more SNe in the SGH (227 vs 123) to drive the fit results for SNe with $z \geq 0.2$ closer to the SGH results.

Monte Carlo analysis

Taken at face value, the probabilities P associated with most discrepant directions (see Table 2.2) are moderately significant. However, assuming Gaussian errors is a strong limiting factor. Also, the size of the errorbars in the distance modulus (and the off-diagonal covariances) provided in the Union2.1 catalog might be inaccurate and, as a consequence, inference based on the χ^2 statistic might be biased. For these reasons, we re-evaluate the statistical significance of the anisotropies using a more robust Monte Carlo method.

In order to assess the impact of random errors and account for the non-uniform angular distribution of the Union2.1 sample, we build 1000 mock catalogs by randomly shuffling the distance moduli of the Union2.1 SNe. In practice, we assign the distance modulus, its uncertainty and the redshift of a SN Ia

[3] I.e. obtained assuming independent Gaussian errors. The limitation of this approach is discussed in detail in Section 2.4.2.

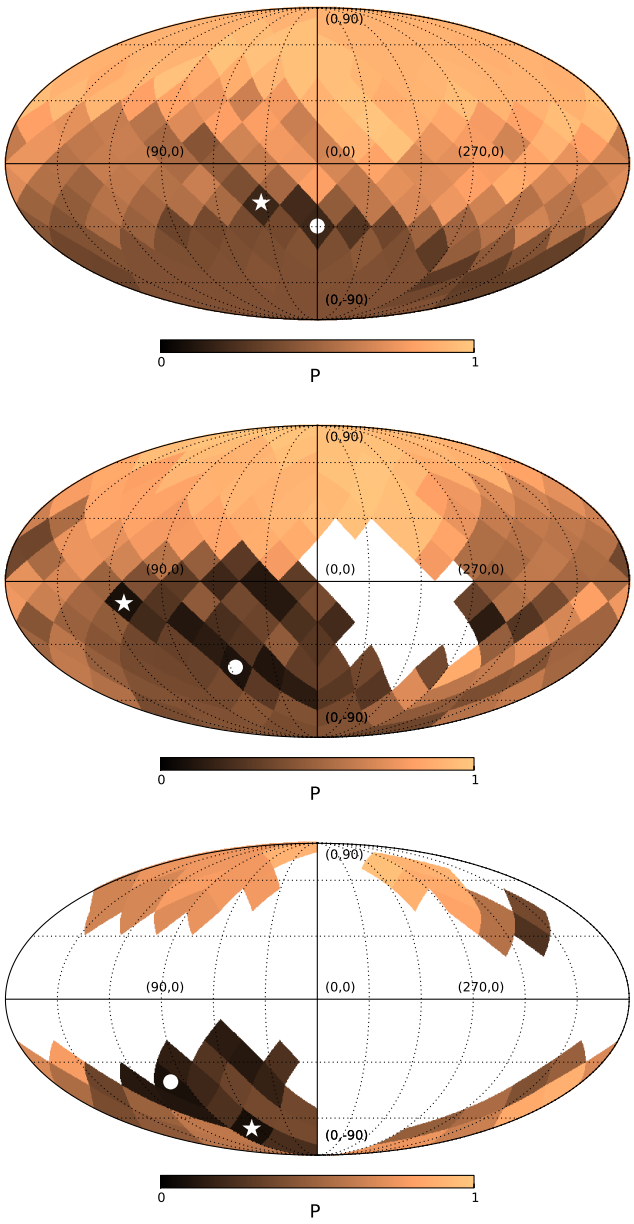

Figure 2.4: Maps of the P value (the estimated likelihood of getting larger deviations than in the data due to random fluctuations under the null hypothesis that the SN Ia Hubble diagram is isotropic) for different cone opening angles (from top to bottom, $\theta = \frac{\pi}{2}, \frac{\pi}{3}$ and $\frac{\pi}{6}$). The direction with the smallest value of P in each map is marked with a star and the second-most discrepant direction is highlighted with a circle. The white regions denote the pixels for which the cone contains less than 25 SNe Ia and are excluded from the statistical analysis.

Table 2.2: Galactic coordinates (l, b) and P values characterizing the most (stars) and the second-most (circles) discrepant directions for different cone opening angles, θ. Also reported are the number of SNe Ia in the cones, N, the best-fit values for Ω_Λ and Δ (in mag) and the ratio $\hat{\chi}^2/\nu$.

θ	(l, b)	Ω_Λ	Δ	$\hat{\chi}^2/\nu$	P	N
★ $\pi/2$	(33.7,-19.5)	$0.58^{+0.11}_{-0.13}$	$41.424^{+0.077}_{-0.072}$	1.09	0.192	128
• $\pi/2$	(0.0,-30.0)	$0.61^{+0.09}_{-0.10}$	$41.441^{+0.066}_{-0.067}$	1.08	0.197	161
★ $\pi/3$	(112.5,-9.6)	$0.60^{+0.22}_{-0.31}$	$41.439^{+0.130}_{-0.110}$	1.20	0.086	74
• $\pi/3$	(56.2,-41.8)	$0.59^{+0.11}_{-0.15}$	$41.424^{+0.081}_{-0.072}$	1.15	0.101	118
★ $\pi/6$	(67.5,-66.4)	$0.58^{+0.12}_{-0.15}$	$41.419^{+0.084}_{-0.074}$	1.18	0.081	100
• $\pi/6$	(101.2,-41.8)	$0.55^{+0.21}_{-0.29}$	$41.408^{+0.124}_{-0.106}$	1.20	0.085	73

Table 2.3: Best-fit values obtained using SNe in the NGH and SGH, separately. Also reported are the corresponding reduced chi-square, χ^2/ν, the number of SNe Ia with $z \geq 0.2$ considered for the fit, N, and their average distance-modulus uncertainty, $\bar{\sigma}_\mu$.

	Ω_Λ	Δ	χ^2/ν	N	$\bar{\sigma}_\mu$
NGH	$0.70^{+0.07}_{-0.09}$	$41.443^{+0.088}_{-0.084}$	0.82	123	0.30
SGH	$0.68^{+0.06}_{-0.08}$	$41.441^{+0.060}_{-0.056}$	1.01	227	0.23

to the angular position of another (random) SN Ia. Each mock catalog thus contains exactly the same number of SNe as the original Union2.1 sample and has exactly the same SN sky distribution. Moreover, all possible anisotropies should be erased by the shuffling procedure while the statistical properties of the distance moduli and their uncertainties are unchanged with respect to the observational data. Therefore our mock catalogs form an ensemble of realizations mimicking an isotropic Universe but having the same statistical properties as the actual Union2.1 data.

We treat the mock catalogs as the real data and identify the two most discrepant directions in each of them using the P-value-based method for the three different cone opening angles. We then compute the fraction, f_0, of the realizations in which the most (or the second most) discrepant direction is associated with a P value which is smaller than the observed ones reported in Table 2.2. For the most (second-most) discrepant directions we find that $f_0 = 0.569, 0.623$ and 0.674 $(0.473, 0.550, 0.490)$ for $\theta = \frac{\pi}{2}, \frac{\pi}{3}$ and $\frac{\pi}{6}$, respectively. Purely based on this signal-to-noise criterion, we conclude that no statistically significant anisotropy can be detected in the Union2.1 sample.

Alignment with the CMB dipole

Although the Monte Carlo test shows that random chance in an isotropic universe can easily produce most discrepant directions with lower P values than we found analyzing the actual data, the observed anisotropies present a characteristic feature which is worth being discussed.

The temperature distribution in the CMB presents a strong dipole anisotropy which is usually interpreted as due to our motion with respect to the CMB rest frame towards the direction with Galactic coordinates $(263.^\circ99 \pm 0.14, 48.^\circ26 \pm 0.03)$ (Planck Collaboration et al. 2014c). Figure 2.6 shows that the most discrepant directions we obtained from the Union2.1 sample closely align with the axis of the CMB dipole (CDP) in the SGH opposite to our motion with respect to the CMB rest frame (hereafter CDP-South). Assuming that the redshifts of the SNe Ia in the Union2.1 compilation have been correctly

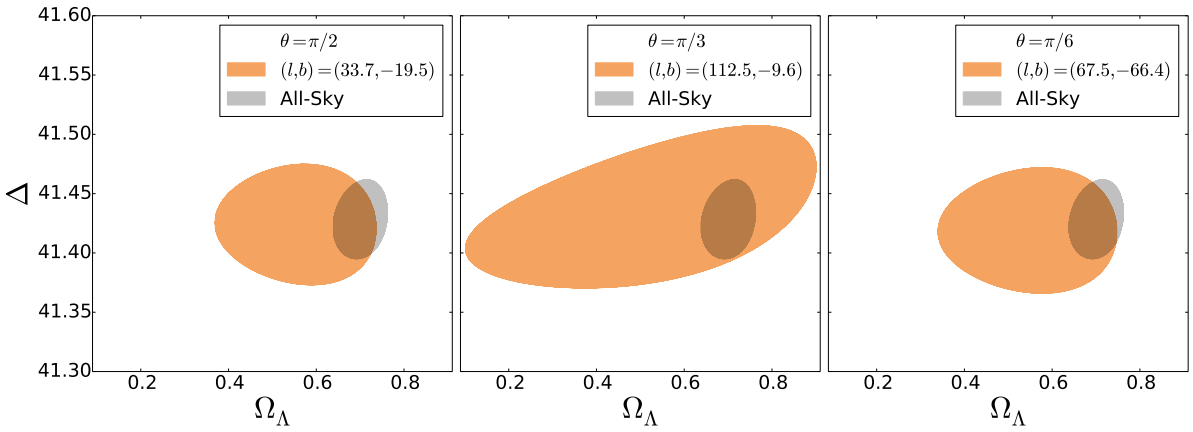

Figure 2.5: Formal 1σ ($\Delta\chi^2 \leq 2.30$) confidence regions from the all-SNe fit (gray) and the localized fits along the most discrepant directions (orange). From left to right the cone opening angle assumes the values $\theta = \frac{\pi}{2}$, $\frac{\pi}{3}$ and $\frac{\pi}{6}$.

transformed to the CMB rest frame, there is no obvious reason for explaining the origin of this alignment. As already mentioned in the Introduction, the CMB quadrupole (CQP) and octopole (COP) are also closely aligned with the CDP (Planck Collaboration et al. 2014b; Schwarz et al. 2004; Copi et al. 2010b, 2013, see Figure 2.6). It is yet unclear whether these alignments are a statistical fluke or a signature of new physics. Anyway, our study shows that the magnitude-redshift relation of SNe Ia with $z \geq 0.2$ tends to be different in the same direction (albeit the difference is detected with low signal-to-noise ratio). Other authors have reported similar results using the Union compilations (Cooke & Lynden-Bell 2010; Antoniou & Perivolaropoulos 2010; Li et al. 2013).

The debate on the physical relevance of the CMB anomalies opened up a discussion in the literature about the legitimacy and validity of “a posteriori" analyses in which tailored statistical tests are designed and hand picked after noticing the peculiarities in the data. A widespread point of view states that in a large dataset it is always possible to isolate some “strange" features (e.g. Bennett et al. 2011). To minimize the pitfalls of a posteriori reasoning, we focus on the well established CDP and do not consider the CQP and COP any further.

We thus proceed to quantify the probability that the most discrepant directions (defined in terms of the P value as above) form a given angle with the CDP under the null hypothesis of an isotropic magnitude-redshift relation. In order to account for the non-uniform sky distribution of the Union2.1 sample (especially for the SDSS-II stripe which is close to the CDP-South) we use the Monte Carlo realizations introduced in Section 2.4.2. Figure 2.7 shows the resulting probability distribution for the cosine of the angle between the most discrepant direction and the axis of the CDP-South. Our measurements from the Union2.1 data are indicated by vertical dashed lines. The second column in Table 2.4 reports the fraction of Monte Carlo realisations, f_1, showing a better alignment than our measurement. Our results suggest that it is rather unlikely to get an alignment as strong as the observed one under the null hypothesis of an isotropic magnitude-redshift relation. In fact, considering the most discrepant direction for $\theta = \frac{\pi}{2}$, only 8.5 per cent of the Monte Carlo realisations show a smaller separation angle than observed and this reduces to 4.5 percent for $\theta = \frac{\pi}{3}$. Note that for $\theta = \frac{\pi}{3}$ and $\frac{\pi}{6}$, the second-most discrepant directions are even better aligned with CDP-South. In these cases $f_1 \simeq 0.01$.

The test above is blind to the statistical significance of the most discrepant directions. In order to account for this, we compute the fraction of Monte Carlo realisations, f_2, for which the most discrepant directions are at least as significant as the measured ones (in terms of the P value) and are also better

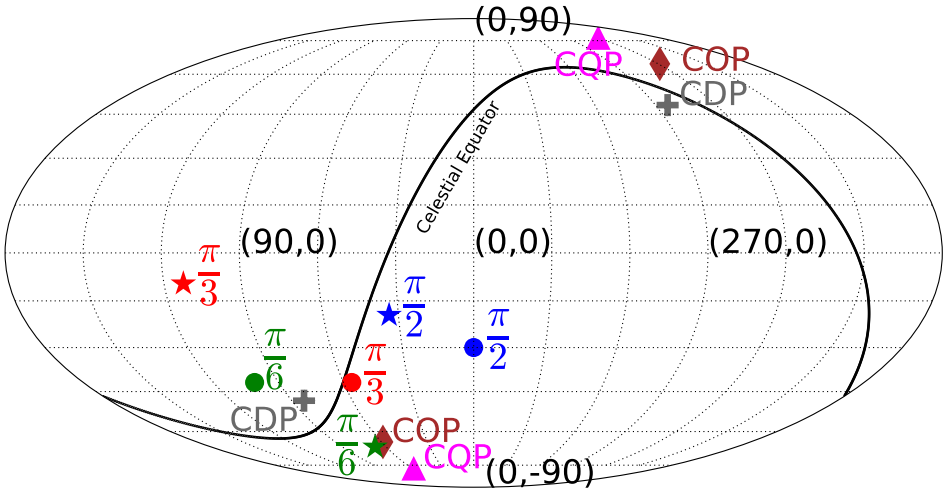

Figure 2.6: The most (star) and the second-most (circle) discrepant directions in the magnitude-redshift relation of SNe Ia (for three cone opening angles $\theta = \frac{\pi}{2}, \frac{\pi}{3}$ and $\frac{\pi}{6}$) obtained in this work are compared with the directions of the CMB dipole (CDP), quadrupole (CQP) and octopole (COP) from Planck Collaboration et al. (2014b). The black solid curve denotes the celestial equator.

aligned with the CDP-South. The third column in Table 2.4 shows that for the most discrepant directions this probability is smaller than 4.5 percent for all the opening angles which means the null hypothesis of an isotropic magnitude-redshift relation should be rejected at the 95 per cent confidence level. The value of f_2 reduces to a fraction of a percent when considering the second-most discrepant direction for $\theta = \frac{\pi}{3}$ and $\frac{\pi}{6}$.

The measured anisotropy could be due to a statistical fluke, to systematics in the SNe data (or error bars), to the presence of localized large scale structures, or even a sign of the failure of the cosmological principle. To further investigate its properties, we repeat the analysis along the most discrepant directions after slicing the SNe data in five redshift bins ($0.2 \leq z < 0.3$, $0.3 \leq z < 0.4$, $0.4 \leq z < 0.6$, $0.6 \leq z < 0.9$ and $z \geq 0.9$). Regrettably, due to the low number of SNe in each bin, the formal 1σ errors span most, if not all, the parameter space $0 \leq \Omega_\Lambda \leq 1$. Therefore no meaningful statements can be made regarding the variations of the best-fit cosmological parameters along the most-discrepant directions. In terms of signal-to-noise ratio, however, the redshift range $0.4 \leq z < 0.6$ clearly emerges as the most discrepant one for all the cone opening angles ($P = 0.033, 0.021$ and 0.016 for $\theta = \pi/2, \pi/3$ and $\pi/6$, respectively).

Given the current sparsity of the data, no firm conclusion can be drawn except from the fact that there seems to be a moderately statistically significant (2-3σ) anisotropy in the magnitude-redshift relation of SNe Ia close to the direction opposite to our motion with respect to the CMB rest frame. It is worth remembering that, in the Union2.1 compilation, most of the SNe Ia surrounding the CDP-South come from the SDSS-II stripe. Further investigations are thus needed to clarify the relation between the CMB dipole axis, our motion, and the way SNe data around this direction are treated.

2.5 Conclusions and future perspectives

We presented a simple but powerful method for investigating the isotropy of cosmic acceleration traced by Type Ia SNe with different angular resolution, θ. The key idea is to consider all the SNe contained within a cone with vertex located at the origin of the Galactic coordinate system and with apex angle 2θ.

Table 2.4: Alignment with the CMB dipole. Angular separation, α, between the direction of the CMB dipole in the SGH (CDP-South) and the most (stars) and the second-most (circles) discrepant directions for the maps based on the Union2.1 data with different cone opening angles, θ. The probability of measuring a value smaller than α in random realisations of a isotropic magnitude-redshift relation is indicated with f_1 while f_2 also accounts for the condition that the most (second-most) discrepant direction is associated with a smaller P value than for the Union2.1 measurement. Both probabilities have been estimated with a Monte Carlo method (see the main text for the details).

θ	α	f_1	f_2
★ $\pi/2$	49°.4	0.085	0.027
• $\pi/2$	64°.3	0.152	0.052
★ $\pi/3$	45°.5	0.045	0.021
• $\pi/3$	20°.5	0.008	0.002
★ $\pi/6$	20°.1	0.064	0.045
• $\pi/6$	13°.7	0.010	0.006

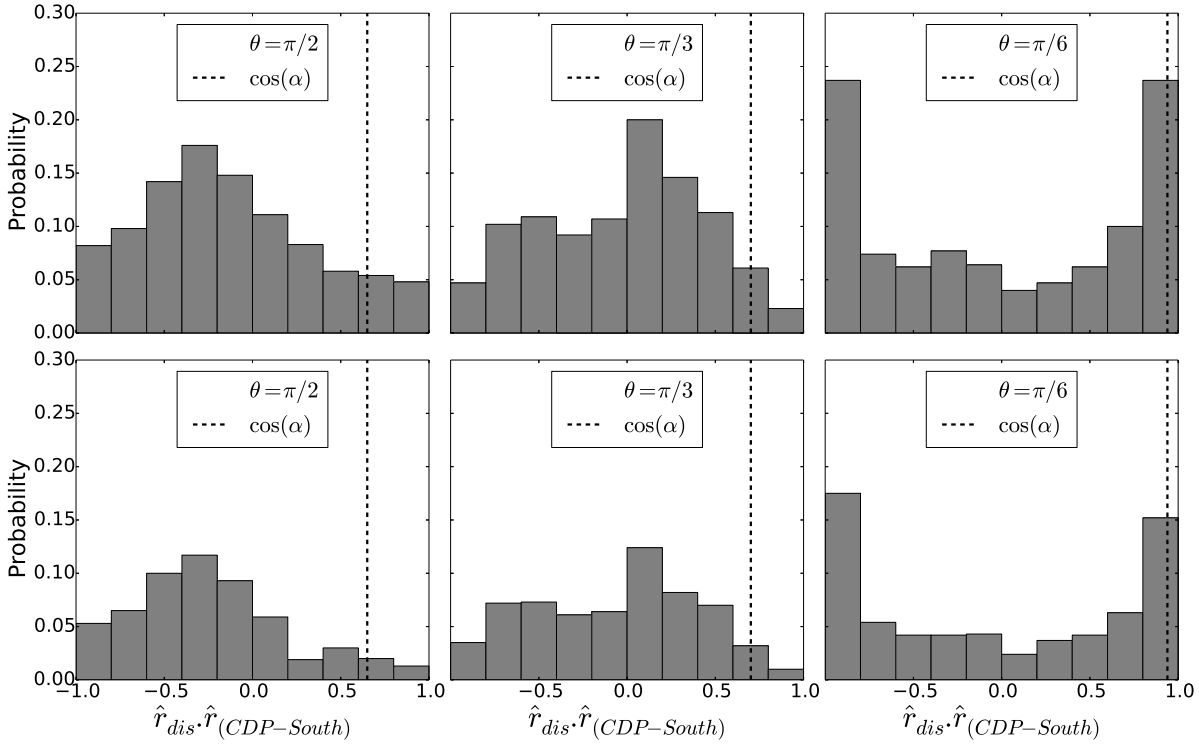

Figure 2.7: Top: Probability distribution of the cosine of the angle between the direction of the CMB dipole in the SGH, $\hat{r}_{CDP-South}$, and the most discrepant direction of the Hubble diagram of SNe Ia, $\hat{r}_{dis}$, determined using the Monte Carlo realisations introduced in Section 2.4.2. Bottom: As above but with the additional condition that the most-discrepant direction is associated with a smaller P value than for the Union2.1 measurement. From left to right, the panels refer to the cone-opening angles $\theta = \frac{\pi}{2}$, $\frac{\pi}{3}$ and $\frac{\pi}{6}$. The cosine of the observed angular separation in the Union2.1 sample, α, (reported in Table 2.4) is shown as a dashed line.

"Local cosmological parameters" are derived by fitting the magnitude-redshift relation of the SNe in the cone with a theoretical relation. The cone direction is then changed so that to cover the entire sky. Our cone-analysis method takes into account the mean variation of the SNe Ia correction parameters over different directions, and yields all-sky maps of the best-fit cosmological parameters.

Although a large data set with a uniform sky distribution is required for a thorough investigation of isotropy, we provided an example of the potential of our method by applying it to the SNe Ia with redshift $z \geq 0.2$ in the Union2.1 compilation. Assuming a flat Universe in the context of the standard cosmological model, we fitted the magnitude-redshift relation by varying the density parameter of the cosmological constant, Ω_Λ, and a parameter , Δ, including the effect of both the Hubble constant and the mean SNe Ia correction parameters. We used a HEALPix grid to discretise the celestial sphere and obtained sky maps for Ω_Λ and Δ considering three different cone-opening angles $\theta = \frac{\pi}{2}$, $\frac{\pi}{3}$ and $\frac{\pi}{6}$.

We ranked the pixels in each map in terms of a P value derived from the χ^2 distribution and which measures how much the local fits differ from the cosmology determined using the entire Union2.1 sample (in a signal-to-noise sense). We thus found the most discrepant directions (two per cone opening angle). Finally, we used a Monte Carlo method to estimate the statistical significance at which we could reject the null hypothesis that the magnitude-redshift relation of SNe Ia is isotropic based on the properties of the most discrepant directions. We found that random fluctuations can easily produce deviations from isotropy with smaller P values than measured in the Union2.1 data. Therefore, the null hypothesis cannot be rejected at any meaningful confidence level based on signal-to-noise arguments alone. However, if we also consider that the detected anisotropies in the Union2.1 sample align well with CMB dipole axis in the Southern Galactic Hemisphere, we find that the null hypothesis should be rejected at the 97.3, 97.9 and 95.5 per cent confidence level for opening angles $\theta = \frac{\pi}{2}$, $\frac{\pi}{3}$ and $\frac{\pi}{6}$, respectively.

We conclude that, although the deviation from isotropy that we found is not very significant per se in terms of signal-to-noise ratio, its vicinity to the axis of the CMB dipole (which enters the pipeline to determine the SN redshift in the CMB rest frame) with 2-3σ statistical significance requires further investigation both on the observational and on the theoretical sides. Note that other observations detected anisotropies in the same area of the sky. The statistical significance of the quadrupole–octopole alignment in the CMB is approximately 99 per cent (Planck Collaboration et al. 2014b). On combination of the likelihoods between the CMB and SN Ia, the null hypothesis of isotropy should be rejected at the 99.98 per cent confidence level (approximately 3.5 Gaussian σ). In this paper we followed a conservative approach by only considering the SN Ia data.

This study should be repeated when larger data sets with more uniform sky coverage will be available. Several major current and future facilities have dedicated plans for studying the accelerated expansion of the universe using SNe Ia. For instance, the Dark Energy Survey (DES) integrates a dedicated program that should detect around 4000 SNe Ia in the redshift range $0.05 < z < 1.2$ (Bernstein et al. 2012). Similarly, the Euclid mission includes a SNe survey within two deep fields each covering around 20 deg^2 and is expected to discover about 3000 SNe Ia out to $z \approx 1.2$ (Laureijs et al. 2011). However, both these surveys will only provide SN data in relatively small regions of the sky (see Figure 2.8) and the most promising perspective for isotropy tests of the Hubble diagram comes from the Large Synoptic Survey Telescope (LSST). While its use for a SN-dedicated survey on a limited area of sky will be able to deliver as many as 140,000 SNe Ia (in 10 years) with very precisely measured light curves, in its normal operating mode (due to its rapid cadence), LSST will discover around 250,000 SNe Ia per year in the redshift range $0.45 < z < 0.7$ and across a large fraction of the sky (Ivezic et al. 2008). Finally, the Panoramic Survey Telescope & Rapid Response System (Pan-STARRS, Brout et al. 2013) which is observing the Northern part of the sky will complement the above mentioned surveys. In summary, exciting perspectives to test the isotropy of the magnitude-redshift relation of SNe Ia with unprecedented accuracy will open up within the next two decades.

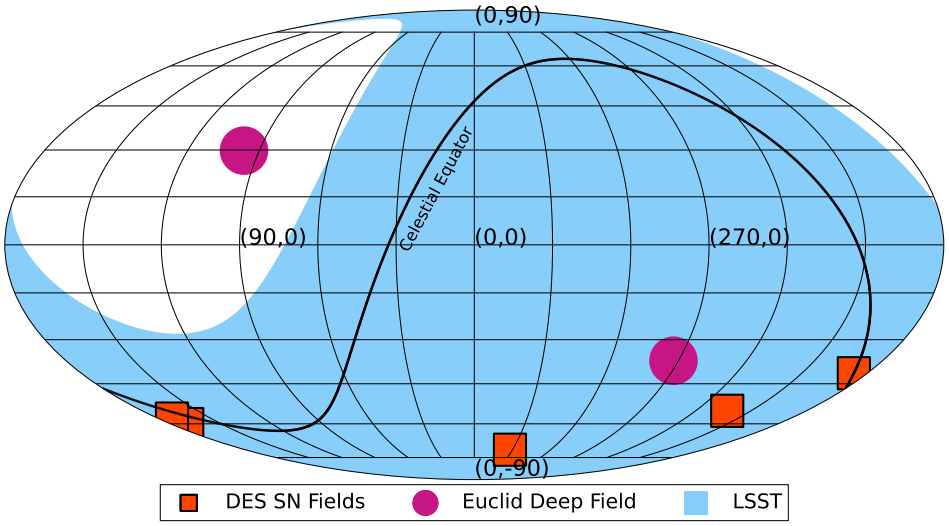

Figure 2.8: Survey footprints for the Euclid deep field, LSST main survey and the (likely) SNe fields of DES in the Galactic coordinate system. The size of the fields for DES and Euclid have been artificially magnified to ease readability. The black solid curve denotes the celestial equator.

Acknowledgments

We thank the referee for providing constructive comments on the manuscript. BJ thanks Ryan Cooke for help with finding some of the SNe Ia coordinates, Dominik Schwarz and Marek Kowalski for constructive comments and Douglas Applegate for very useful discussions. BJ was supported through a stipend from the International Max Planck Research School (IMPRS) for Astronomy and Astrophysics at the Universities of Bonn and Cologne. CP acknowledges support from the Deutsche Forschungsgemeinschaft through the Transregio 33 “The Dark Universe”.

CHAPTER 3

Anisotropy in the all-sky distribution of galaxy morphological types

Abstract

We present the first study of the isotropy of the all-sky distribution of morphological types of galaxies in the Local Universe out to around 200 Mpc using more than 60,000 galaxies from the HyperLeda database. We use a hemispherical comparison method where the sky is divided into two opposite hemispheres and the abundance distribution of the morphological types, T, are compared using the Kolmogorov-Smirnov (KS) test. By pointing the axis of symmetry of the hemisphere pairs to different directions in the sky, the KS statistic as a function of sky coordinates is obtained. For three samples of galaxies within around 100, 150, and 200 Mpc, we find a significant hemispherical asymmetry with a vanishingly small chance of occurring in an isotropic distribution. Astonishingly, regardless of this extreme significance, the observed hemispherical asymmetry for the three distance ranges is aligned with the celestial equator at the 97.1% – 99.8% confidence level and with the ecliptic at 94.6% – 97.6%, estimated using a Monte Carlo analysis. Shifting T values randomly within their uncertainties has a negligible effect on this result. When a magnitude limit of $B \leq 15$ mag is applied to these samples, the galaxies within 100 Mpc show no significant anisotropy after randomization of T. However, the direction of the asymmetry in the samples within 150 and 200 Mpc and the same magnitude limit is found to be within an angular separation of 32 degrees from $(l, b) = (123.7, 24.6)$ with a 97.2% and 99.9% confidence level, respectively. This direction is only 2.6 degrees away from the celestial north pole. Unless the Local Universe has a significant anisotropic distribution of galaxy morphologies aligned with the orientation or the orbit of the Earth (which would be a challenge for the Cosmological Principle), our results show that there seems to be a systematic bias in the classification of galaxy morphological types between the data from the northern and the southern equatorial sky. Further studies are absolutely needed to find the exact source of this anisotropy.

Note: This chapter is a reprint of a paper of the same title published in the Astronomy & Astrophysics journal. Credit: **B. Javanmardi** and P. Kroupa, A&A, 597, A120, 2017, reproduced with permission ©ESO.

3.1 Introduction

Galaxies appear in various shapes and are observed to have a range of different properties; one of the main ways of studying their evolution is to classify them based on these observed features. The most widely known classification of galaxies, which is famously known as "Hubble's tuning fork"[1], categorizes the (mostly nearby) galaxies into a range of morphological types based on bulge/disk domination. This classification was later revised by de Vaucouleurs (1959) who added a numerical value to each Hubble type and also to the intermediate stages.

The morphology of galaxies is closely linked to their physical properties and those of their environments (Sandage 1975; Kormendy 1982; van den Bergh 1998; Abraham 1998; Calvi et al. 2012), and is one of the important tools for studying galaxy formation and evolution. Bulge formation scenarios depend on galaxy formation models (Hopkins et al. 2010; Kroupa 2015; López-Corredoira & Kroupa 2016a; Combes 2016); distinct galaxy types are observed to have very different stellar populations and star formation rates (Grebel 2011) and different spectral properties (Sánchez Almeida et al. 2011), and their inner structure , such as bar and bulge types, is connected with their observed kinematics (Molaeinezhad et al. 2016). For a study on the evolution of the Hubble sequence see Delgado-Serrano et al. (2010) and for a recent review on galaxy morphology see Buta (2013).

Though the majority of the bright nearby galaxies fit into the Hubble's tuning fork classification, the high redshift galaxies detected by deep surveys and the low surface brightness dwarf galaxies, whose number is increasing thanks to various surveys inside and outside the Local Group (e.g., Bernstein et al. 2012 and Javanmardi et al. 2016, respectively), are hard to classify using the standard morphological classification system (Naim et al. 1997; Abraham & van den Bergh 2001).

One of the most widely used classification schemes is that of de Vaucouleurs compiled in the Third Reference Catalogue of Bright Galaxies (RC3) (de Vaucouleurs et al. 1991) from which many other catalogs extract the morphological types of different galaxies. As pointed out by Makarov et al. (2014), visual inspection has been the main method of classification in RC3.

The need for an automated morphology classification has been known for decades (Naim 1995) and has been used in recent years (see, e.g., the recent studies by Huertas-Company et al. 2015 and Kuminski & Shamir 2016, and references therein). Nair & Abraham (2010) and Baillard et al. (2011) used the data from the Sloan Digital Sky Survey (SDSS) and attempted to improve the visual classification of galaxy morphologies with the aim of paving the way for automated galaxy classification by providing training sets and calibration samples (for other catalogs of galaxy morphologies see Fukugita et al. 2007; Shibuya et al. 2015; Herrera-Endoqui et al. 2015; Krywult et al. 2016; Poudel et al. 2016, and Psychogyios et al. 2016). In general, the goal is to achieve a catalog of the morphological types of the observed galaxies as complete and systematic-free as possible and to have a well-defined classification method applicable to future large galaxy surveys. A catalog of this kind is obviously crucial for studies of galaxy formation and evolution.

In this work, and for the first time, we search for possible deviations from isotropy in the all-sky distribution of the morphological types of galaxies within ≈ 200 Mpc using the HyperLeda database. Based on the Cosmological Principle (generally understood to be confirmed by most of the observations so far), on sufficiently large scales the properties of the Universe, including the distribution of galaxy types, should be statistically isotropic. Therefore, deviations from isotropy can be a hint of

[1] Based on a classification originally published in Reynolds (1920) and later by Hubble (1926), and on the tuning fork of Jeans (1928). Its famous form was later presented in Hubble (1936). See Block & Freeman (2015) for a historical note.

systematic issues with the morphological classification of galaxies or with the homogenization of catalogs.

On the other hand, it is vital to re-inspect the assumption of isotropy with various observations (Maartens 2011) and this is one of the motivations of our study. If a significant deviation from cosmic isotropy is detected and confirmed by various data sets, cosmology will face a major paradigm change. During the last decade, probing isotropy in all-sky extragalactic data has become a vibrant research topic and continues to deliver interesting results. Tegmark et al. (2003), Eriksen et al. (2004), and Hansen et al. (2004) reported some large-scale anisotropies (hemispherical asymmetry and quadrupole-octopole alignment) in the cosmic microwave background (CMB) radiation data from the *WMAP* satellite. These CMB anomalies have recently been confirmed by the Planck Collaboration et al. (2014b) suggesting that they are not artifacts caused by the detectors or data-reduction procedures (see also Akrami et al. 2014; Rassat et al. 2014a; Copi et al. 2015, and Mukherjee et al. 2016). Javanmardi et al. (2015) found an anisotropy in the magnitude-redshift relation of high redshift Type Ia Supernovae (SNe Ia) that is significantly aligned with the direction of the CMB dipole and very close to the CMB quadrupole-octopole alignment (for similar studies see Carvalho & Marques 2015; Bengaly 2016; Migkas & Plionis 2016; Lin et al. 2016, and references therein). Also, an inconsistency between the amplitude of the observed dipole in the distribution of radio galaxies and the value expected from the CMB dipole has been reported in Singal (2011), Rubart & Schwarz (2013), and Tiwari & Nusser (2016). For a recent review on various isotropy studies see Zhao et al. (2013).

The isotropy of the spatial distribution of galaxies has been probed by various authors (Gibelyou & Huterer 2012; Yoon et al. 2014; Appleby & Shafieloo 2014a; Alonso et al. 2015; Bengaly et al. 2016). These studies have found some mild anisotropies with different directions, but none of them has reported a significant deviation.

In our analysis, we consider three distance ranges separately: galaxies with radial velocity less than 7,000, 10,000, and 14,000 km/s (equivalent to around 100, 150, and 200 Mpc from us, respectively[2]). Based on the standard model of cosmology, at such distance scales and especially beyond ≈150 Mpc (Marinoni et al. 2012) the distribution of galaxies should be statistically isotropic. For each distance range, we separate the galaxies by dividing the sky into two opposite hemispheres and compare their morphological type distribution using the Kolmogorov-Smirnov test. By pointing the axis of symmetry of our hemispheric cut towards different directions on the sky and repeating the test, we find the pair of hemispheres with the greatest difference in the distribution of morphological types and quantify the significance of the difference.

This paper is organized as follows. In Section 3.2 we describe our sample from the HyperLeda database. Our method of analysis is explained in Section 3.3. We present the results in Section 3.4, discuss them critically in Section 3.5, and finally we summarize and conclude in Section 3.6.

3.2 Data

HyperLeda (Paturel et al. 2003a,b; Makarov et al. 2014) is a large database of more than three million objects, around 1.5 million of which are confirmed galaxies that uniformly cover the entire sky except for the region around the Galactic plane. This database contains different observed properties like magnitude, surface brightness, color, redshift, and morphological type of galaxies. These measurements have been homogenized to standard systems and are updated when new measurements become available (Makarov

[2] Assuming the Hubble constant value of $H_0 = 70.0$ km s^{-1} Mpc^{-1}.

et al. 2014).

The morphological types, T, in HyperLeda are homogenized values based on compilation of morphology measurements from the literature. These types are in the de Vaucouleurs scale (de Vaucouleurs et al. 1991) ranging from $T = -5$ for elliptical galaxies to $T = 10$ for irregular galaxies. Most of these measurements are obtained by visual inspection of optical images. After the homogenization (which also takes into account the quality of each measurement), the best possible value and its uncertainty for each galaxy is determined. They are not limited to integer values and have an accuracy up to the first decimal digit in the HyperLeda database (e.g., $T = 2.2 \pm 0.7$ for the galaxy NGC3368). The information on the instruments used for these measurements are not kept in the database, but can be found in the individual works[3].

For the purpose of this study, we limit our sample to all the confirmed galaxies that have a radial velocity in the CMB reference frame, V_{CMB}, lower than 14,000 km/s. This velocity corresponds to a distance of about 200 Mpc. This gives us around 200,000 galaxies from the HyperLeda database. For each galaxy, we obtain its equatorial and Galactic coordinates, its morphological type (if available), its corresponding uncertainty (σ_T), corrected apparent total B magnitude, and absolute B-band magnitude (M_B) from the database.

More than 65,000 of these galaxies (≈33 % of the sample) have a measured morphological type assigned to them in the database[4]. In order to increase the robustness of our analysis, we exclude the ≈3000 galaxies (around 5% of the galaxies with T) for which an absolute B-band magnitude is not available[5]. This condition gives us the final sample of more than 62,000 galaxies that we used for our statistical analysis, hereafter referred to as "the whole sample". The faintest object in the sample has $B = 23.5$ mag, but only around 2500 galaxies in the sample have $B \geq 17.0$ mag[6]. The number distribution of the T values of the whole sample is shown in Figure 3.1 and its sky distribution in the Galactic coordinate system is shown in Figure 3.2 with the color code being V_{CMB} in units of km/s. We see that galaxies are distributed uniformly across the sky (except for the region around the Galactic plane) and we see no trace of any particular survey.

3.3 Method

3.3.1 Hemispherical comparison

We consider a particular hemisphere of the sky whose pole is pointing at a direction $\hat{r}$ with longitude and latitude (l, b) in the Galactic coordinate system. We then separate the galaxies into two groups: those inside that hemisphere and the ones that are in the opposite hemisphere whose pole is pointing towards $-\hat{r}$ with coordinates $(l + 180°, -b)$. We then compare the morphological distribution of these two sets of galaxies. The aim is to vary $\hat{r}$ to point towards different directions on the sky and repeat the hemispheric division and distribution comparison in order to find the pair of hemispheres with the greatest difference in the distribution of T and to calculate the significance of the difference. We start from the northern Galactic hemisphere, so $-\hat{r}$ will be in the southern hemisphere. We pixelize the sky using a HEALPix[7]

[3] The authors obtained some of the information in this paragraph from a private communication with Dmitry Makarov (one of the team members of HyperLeda) in August 2016.
[4] Our sample was downloaded from the database in May 2016. The database might have been updated since then.
[5] We consider the effect of including them in our analysis in Section 3.5.1.
[6] We also apply magnitude limits to our sample in Section 3.5.1.
[7] Hierarchical Equal Area isoLatitude Pixelation, http://healpix.sourceforge.net

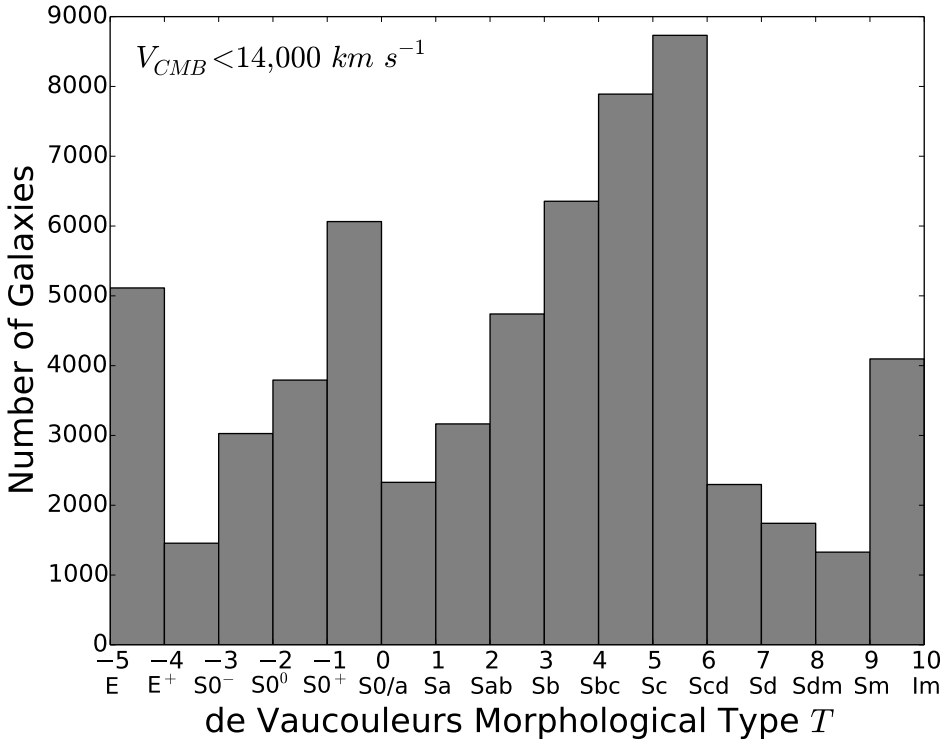

Figure 3.1: Number distribution of the T values for the galaxies in the HyperLeda database with $V_{CMB} < 14,000$ km/s and a measured M_B. In all the bins only the left edge is included in the counting (e.g., for the the first bin $-5 \leq T < 4$) except for the last bin, which also includes the right edge (i.e., $9 \leq T \leq 10$). This is the same for the rest of the histogram plots in this paper.

grid (Górski et al. 2005) with 768 pixels (or directions). This gives us 384 pairs of opposite hemispheres for our analysis.

3.3.2 Kolmogorov-Smirnov test

A simple but powerful statistical method for quantifying the level of consistency of the distribution of two data sets is the Kolmogorov-Smirnov (KS) test. This non-parametric method is used to test whether two data sets come from the same parent distribution. After separating the galaxies into two groups using the hemispheric cut (see Section 3.3.1), we obtain the cumulative distribution functions, $S_{\hat{r}}(T)$ and $S_{-\hat{r}}(T)$, of the morphological types in the hemispheres pointing at $\hat{r}$ and $-\hat{r}$, respectively. These distribution functions are normalized so that their highest value is equal to unity. The KS statistic as a measure of the difference between these two distributions is simply the maximum value of the absolute difference between $S_{\hat{r}}(T)$ and $S_{-\hat{r}}(T)$ (Press et al. 1986):

$$D(\hat{r}) = \max_{-5 \leq T \leq 10} |S_{\hat{r}}(T) - S_{-\hat{r}}(T)|. \tag{3.1}$$

We find $D(\hat{r})$ for the 384 hemisphere pairs to determine the direction with the highest D.

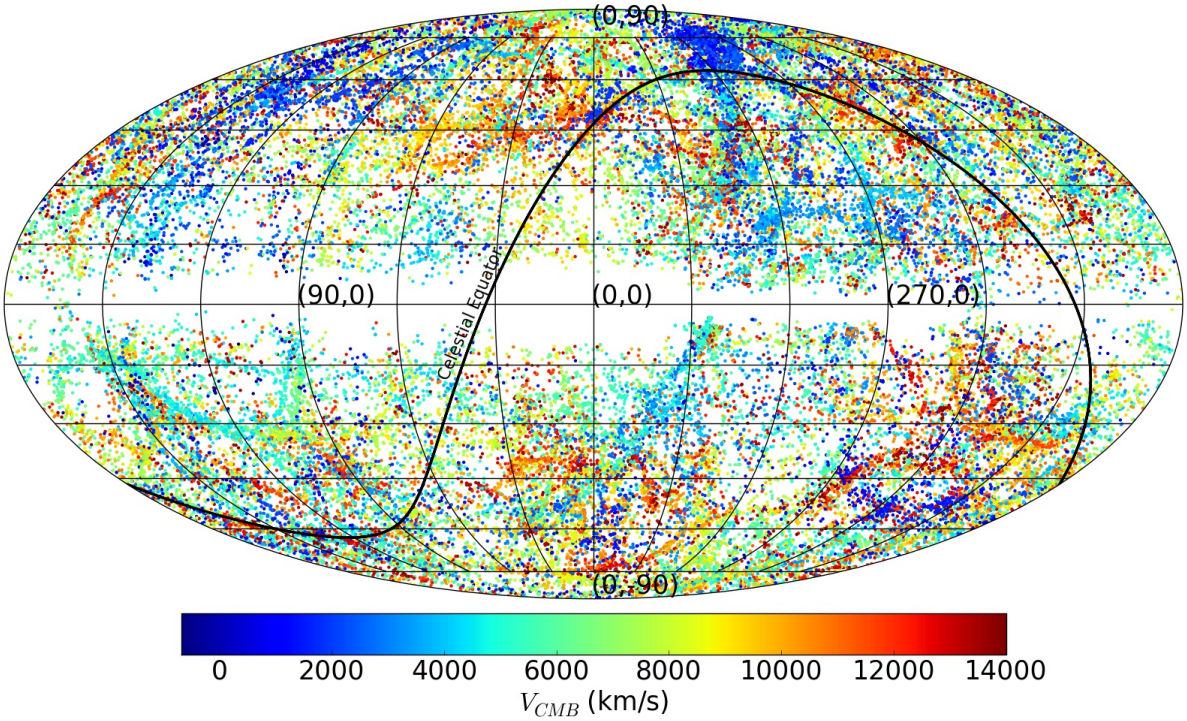

Figure 3.2: Sky distribution of all the galaxies in the HyperLeda database with $V_{CMB} < 14,000$ km/s that have T and M_B, in the Galactic coordinate system. The color code is radial velocity, V_{CMB}, in km/s and the celestial equator is shown by a black solid curve. The sample uniformly covers all the sky (except for the regions in and around the disk of our Galaxy).

3.4 Results

3.4.1 Hemispherical comparison and the directions with the greatest difference

Sky maps of $D(\hat{r})$ for the three radial velocity ranges are shown in the left panel of Figure 3.3. The value in each pixel is obtained by applying the KS test on the hemisphere whose pole is pointing towards the center of that pixel and its opposite hemisphere. Obviously, the D for each direction $\hat{r}$ and its opposite direction $-\hat{r}$ is exactly the same since it is a measure of the difference between them. On each map, the direction with the greatest difference, $\hat{r}_{max}$, and its opposite direction, $-\hat{r}_{max}$, are marked by a star and a circle, respectively. It can be seen that the general trend and the $\hat{r}_{max}$ in all three maps are very close to each other.

In Table 4.3, we list the coordinates of the $\hat{r}_{max}$ and the corresponding KS results, D_{max}, for the three V_{CMB} ranges. The number of total galaxies in the HyperLeda database within each radial velocity range, N_{tot}, and the number of galaxies that have both T and M_B and were used in our analysis, N_a, are also listed in this table. We see that D_{max} decreases when the distance increases from V_{CMB} <7,000 to 10,000 km/s, but increases again when going to V_{CMB} <14,000 km/s, while $\hat{r}_{max}$ remains unchanged in this step.

In this table, we also list the number of galaxies in the pair of hemispheres corresponding to D_{max}, namely $N_{\hat{r}_{max}}$ and $N_{-\hat{r}_{max}}$. We see that their difference is small for all three distance ranges, but to check whether these directions are related or are close to the directions with the greatest difference in the number of galaxies, we can look at the variation in the number of galaxies in each sample across the sky.

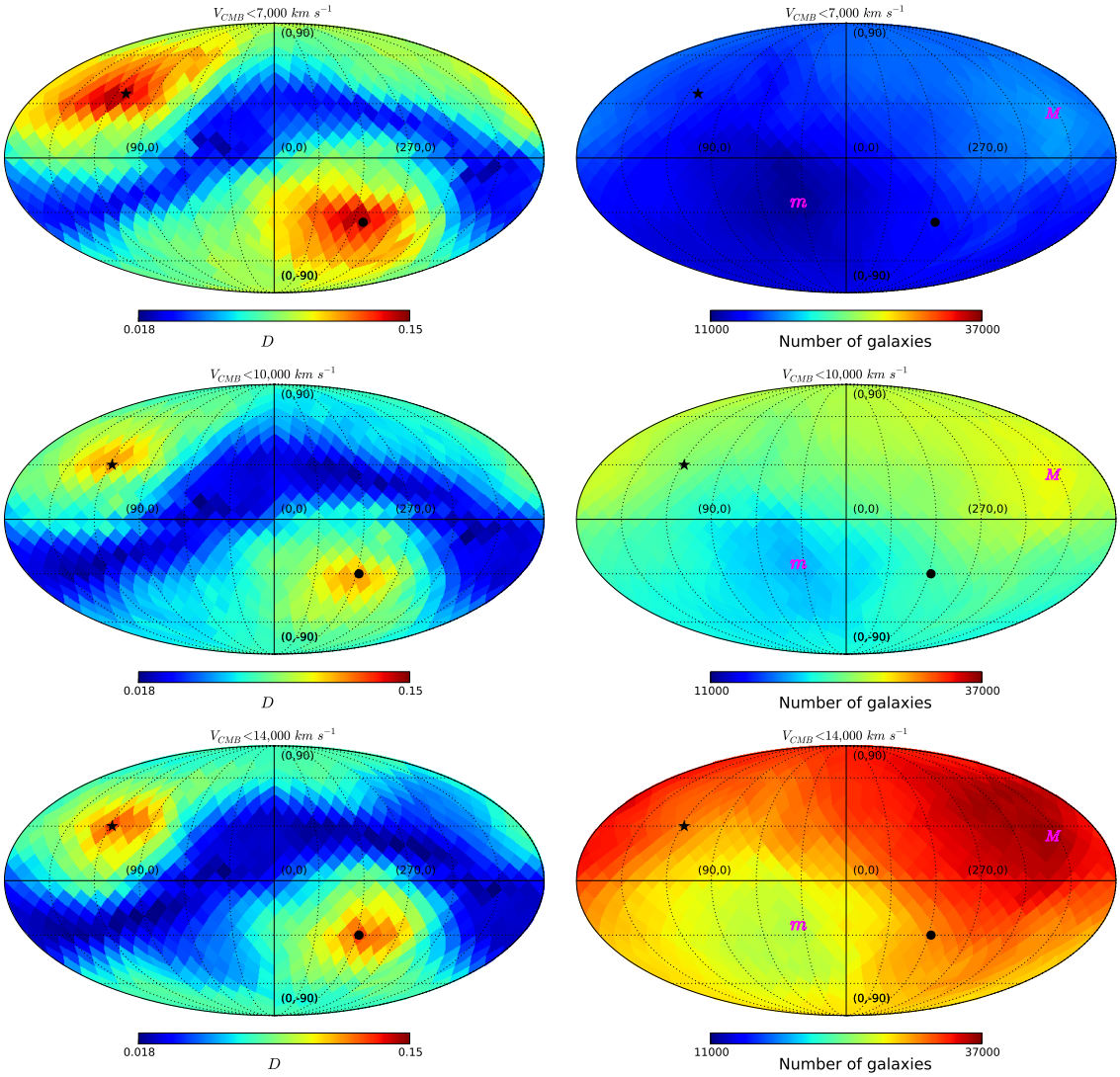

Figure 3.3: Left: Sky maps of D from the KS test in the Galactic coordinate system from top to bottom for V_{CMB} <7,000, 10,000, and 14,000 km/s. The value in each pixel is obtained from the KS comparison of the pair of hemispheres with axis of symmetry along the center of that pixel. The opposite direction of each pixel has exactly the same value. On each map, the direction $\hat{r}_{max}$ is marked by a star and its opposite direction, $-\hat{r}_{max}$, by a circle. Right: Variation in the number of galaxies in each sample across the sky, also in the Galactic coordinate system. The value of each pixel is the number of galaxies in a hemisphere whose pole is pointing towards that pixel. The directions with the minimum and the maximum number are denoted by small m and capital M, respectively. We see that the directions with the greatest difference in the distribution of morphologies are very different from those with the greatest difference in the number of galaxies (see Section 3.4.1).

Table 3.1: Our three radial velocity ranges and their corresponding estimated distances, the total number of galaxies from the HyperLeda database N_{tot} for each range and the number of galaxies N_a used in our analysis (i.e., having T and M_B). The Galactic coordinates of the directions having the greatest difference, $\hat{r}_{max}$, and their corresponding KS statistic, D_{max}, are listed in columns 5 and 6, respectively. The number of galaxies in the pair of hemispheres with the greatest difference, $N_{\hat{r}_{max}}$ and $N_{-\hat{r}_{max}}$ are also listed. We note that these two numbers are similar in all three cases.

V_{CMB}/(km/s) <	$\approx d$ (Mpc)	N_{tot}	N_a	$\hat{r}_{max} = (l, b)$	D_{max}	$N_{\hat{r}_{max}}$	$N_{-\hat{r}_{max}}$
7,000	100	62,314	29,830	(112.5, 35.7)	0.143	15,268	14,562
10,000	150	118,858	46,533	(118.1, 30.0)	0.115	24,307	22,226
14,000	200	198,971	62,125	(118.1, 30.0)	0.128	31,194	30,931

In the right panel of Figure 3.3, the number of galaxies in the hemispheres whose poles are pointing towards each pixel is plotted. We also show $\hat{r}_{max}$ and $-\hat{r}_{max}$ as in the left panel. Although these are only the galaxies that have a T value, the change in the number is smooth; the maximum, M, is consistently close to the direction that the Local Group moves towards (with respect to the CMB rest frame; see, e.g., Gibelyou & Huterer 2012), and the minimum, m, is in the opposite direction. Hence, the directions corresponding to D_{max} are very different from those with the greatest difference in the number of galaxies.

In the first two columns of Figure 3.4 we show the distribution of T in the hemispheres towards $\hat{r}_{max}$ and $-\hat{r}_{max}$ for the three V_{CMB} ranges. Their cumulative distributions are shown in the third column of this figure. We can see two prominent differences between the morphological distribution of galaxies in these opposite hemispheres. First, the number of galaxies with $9 \leq T \leq 10$ (i.e., Sm and Im types) in the direction of $\hat{r}_{max}$ is around twice as high as the number of these types in the direction $-\hat{r}_{max}$ in all three V_{CMB} ranges. Second, the number of galaxies with $-1 \leq T < 0$ (i.e., $S0^+$ types) in the direction of $-\hat{r}_{max}$ is more than twice the number of these galaxies in the direction of $\hat{r}_{max}$, again for all three V_{CMB} ranges. In the latter case, a clear jump in the cumulative distribution functions is visible. Another increase in this function is at $T = 5$ (i.e., Sc galaxies) and their number is higher towards $-\hat{r}_{max}$ in all the three V_{CMB} ranges.

Finally, we emphasize that the results are almost the same in all three of the distance ranges.

3.4.2 Significance of the observed asymmetry

Given the assumption that the distribution of galaxies is statistically isotropic in the distance ranges under consideration and therefore that the distribution of morphologies is statistically similar in different directions, we calculate the significance of the observed anisotropy using the KS distribution and different Monte Carlo (MC) analyses.

KS distribution

The null hypotheses here is that the morphological types in the opposite hemispheres towards $\hat{r}_{max}$ and $-\hat{r}_{max}$ come from the same parent distribution. The probability that this hypothesis is true is equal to the probability of obtaining a difference greater than (or equal to) the observed difference: $p(D_{max}) = Prob_{KS}(D \geq D_{max})$. This can be calculated using the standard two-sided Kolmogorov-Smirnov distribution, which is a function of the number of data points (see Press et al. 1986, for the details). The third column of Table 3.2, contains the probabilities, $p(D_{max})$, obtained for each D_{max} (which are listed again in this table for ease of comparison). These values are dramatically low and basically consistent with zero. To better understand these values, we can compare them to those for

Table 3.2: Probability $p(D_{max})$ (from the KS distribution) that the observed difference, D_{max}, occurs if the morphologies in the pair of hemispheres are from the same parent distribution. For comparison, we list the lowest value obtained from the hemispherical comparison, D_{min}, and its corresponding probability, $p(D_{min})$, for each radial velocity range (see Section 3.4.2). We note that $p(D_{min})$ is orders of magnitude higher than $p(D_{max})$ in all three cases.

V_{CMB}/(km/s)<	D_{max}	$p(D_{max})$	D_{min}	$p(D_{min})$
7,000	0.143	10^{-133}	0.022	1.7×10^{-3}
10,000	0.115	10^{-134}	0.018	8.2×10^{-4}
14,000	0.128	10^{-221}	0.018	6.7×10^{-5}

the directions with the smallest difference, D_{min}, which are also listed in Table 3.2 as $p(D_{min})$. In other words, $p(D_{min})$ corresponds to the pair of opposite hemispheres with the most similar distributions of T. We see that $p(D_{min})$ is many orders of magnitude higher than $p(D_{max})$ for all the three distance ranges.

Monte Carlo: Isotropic realizations

In an effort to investigate the significance calculated from the KS distribution even further, we can use MC analyses. In the first method, we create mock galaxy samples with an isotropic distribution of morphologies by shuffling the position of the galaxies in the analysis while keeping the sky distribution fixed to the original one. Although shuffling can (in some cases) place a late-type galaxy at the center of a galaxy cluster (where an elliptical is usually located), it is still a good way to have an estimate of the distribution of D in the case of a fully random sky distribution. We create 1000 random realizations with an isotropic distribution and repeat the hemispherical comparison method and find the pair of hemispheres with the highest D for each of the realizations. For all three distance ranges, the number of realizations having a D_{max} equal to or higher than the observed values is zero. Actually, the highest D_{max} values obtained in 1000 realizations are 0.029, 0.027, and 0.019 for V_{CMB} <7,000, 10,000, and 14,000 km/s, respectively, which are much lower than the observed values of D_{max}.

Monte Carlo: Random sampling

In the second MC approach, we randomly draw $N_{\hat{r}_{max}}$ galaxies from each sample (regardless of their coordinates) and compare their T distribution with the rest of the galaxies in the sample (whose number amounts to $N_{-\hat{r}_{max}}$) with the KS test. We repeat this 100,000 times and again in none of the random samples do we find a D as high as or higher than the observed D_{max} values. In this case, the highest D values obtained in 100,000 realizations are 0.028, 0.022, and 0.020 for V_{CMB} <7,000, 10,000, and 14,000 km/s, respectively, which are similar to those obtained by the shuffling method.

These MC results (and the ones from Section 3.4.2) were expected from the calculated probabilities from the KS distribution and together they show that it is extremely improbable that the observed values of D_{max} can occur out of an isotropic distribution of galaxy morphologies.

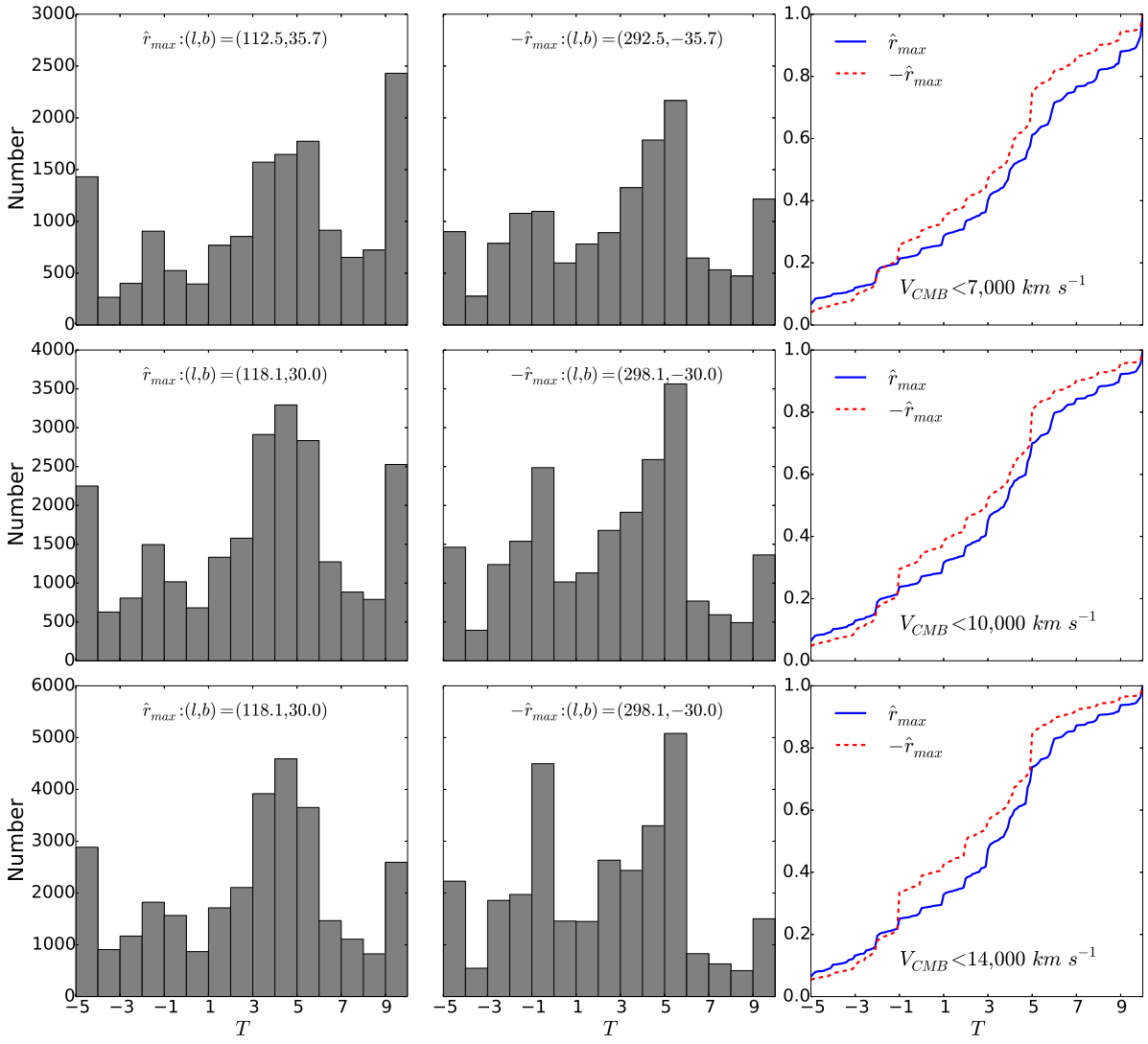

Figure 3.4: Distribution of morphologies in the hemisphere pairs with the greatest difference, i.e., towards $\hat{r}_{max}$ and $-\hat{r}_{max}$, in the first and second columns and their corresponding cumulative distributions in the third column from top to bottom for V_{CMB} <7,000, 10,000, and 14,000 km/s. The prominent differences are at $9 \leq T \leq 10$ and $-1 \leq T < 0$.

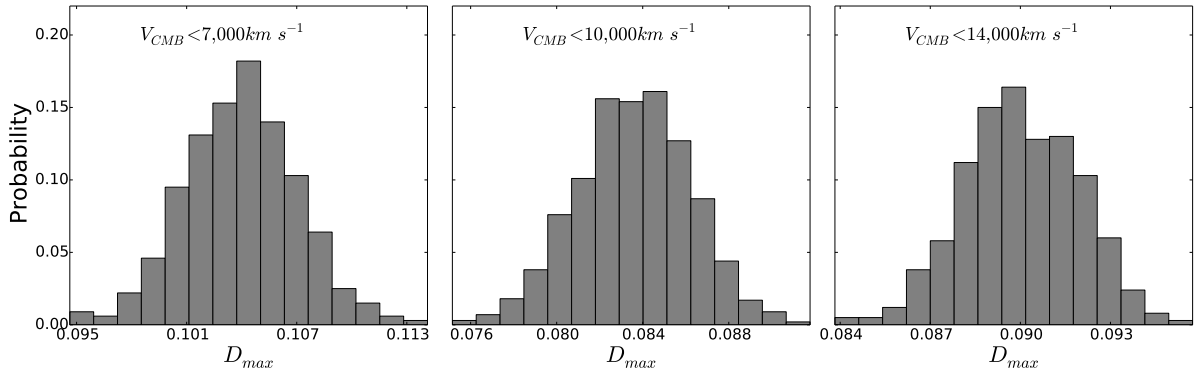

Figure 3.5: The probability distribution of D_{max} for 1000 realizations in which T_i of each galaxy is replaced by $T_i + \Delta T$ where ΔT is randomly drawn from a Gaussian distribution with zero mean and standard deviation σ_{T_i}. From left to right for V_{CMB} <7,000, 10,000 and 14,000 km/s, respectively. See section 3.4.4.

Table 3.3: Angular separation between $\hat{r}_{max}$ and the celestial, α_{CNP}, and the ecliptic, α_{ENP}, north poles. The fraction of 1000 random realizations in which $\hat{r}_{max}$ is as aligned as or more aligned than the observed direction with the CNP, f_{CNP}, and the ENP, f_{ENP}, is also listed (see Section 3.4.3).

V_{CMB}/(km/s)<	α_{CNP}	α_{ENP}	f_{CNP}	f_{ENP}
7,000	12°.3	14°.7	0.029	0.024
10,000	5°.1	18°.8	0.003	0.054
14,000	5°.1	18°.8	0.002	0.052

3.4.3 Alignment with the celestial equator and the ecliptic

The observed significant anisotropy has a peculiar feature that requires further analysis. The direction $\hat{r}_{max}$ for all three distance ranges is very close to the celestial north pole (CNP) and is also relatively close to the ecliptic north pole (ENP); in other words, the plane separating the hemispheres corresponding to D_{max} is aligned with the celestial equator and the ecliptic. The angular separations between $\hat{r}_{max}$ and the CNP, α_{CNP}, and the ENP, α_{ENP}, are listed in Table 3.3. Such an alignment is totally unexpected even if the result from the KS test would not have been significant. Since $\hat{r}_{max}$ is close to both the CNP and the ENP, we quantify the significance of the alignment to both of them.

Significance of the alignment from Monte Carlo analysis

Using the 1000 isotropic realizations from the MC analysis in Section 3.4.2, we find the fractions, f_{CNP} and f_{ENP}, of isotropic samples in which the direction with the highest D has the same or better alignment with the CNP and the ENP. These values are also listed in Table 3.3. To obtain these fractions we do not consider the significance of the anisotropy (i.e., the value of D_{max}) and we only take the direction into account. The fraction of random samples with better alignment and higher D_{max} would be zero as is obvious from the results in Section 3.4.2. Interestingly, f_{CNP} shows that even when the significance of the KS test is not taken into account, the hemispherical asymmetry is aligned with the celestial equator at the 97.1%, 99.7%, and 99.8% confidence levels for V_{CMB} <7,000, 10,000, and 14,000 km/s, respectively. The alignment of the observed hemispherical asymmetry with the ecliptic is at the 94.6% – 97.6% confidence levels, depending on the distance range under consideration. Actually, the alignment with the

ENP is slightly more significant than with the CNP for the sample with V_{CMB} <7,000 km/s. It may be worth noting that one of the CMB anomalies, i.e., the hemispherical asymmetry in the power spectrum, is also aligned with the ecliptic plane (Planck Collaboration et al. 2014b).

3.4.4 Effect of shuffling T within σ_T on the significance and the direction of the anisotropy

The uncertainty of the morphological types, σ_T, for the whole sample ranges between 0.1 and 6.6 with an average $\bar{\sigma}_T = 1.9$. The majority of galaxies have $\sigma_T \approx 2.0$. When a σ_T is available for a galaxy in the HyperLeda database, it means that several astronomers have classified that galaxy. All the galaxies in our sample have a σ_T assigned to their T values. By performing another MC analysis, we check the extent to which random uncertainties reduce the significance of the observed asymmetry and change its direction. To achieve this, we replace the morphological type T_i of each galaxy by $T_i + \Delta T$ where ΔT is randomly drawn from a Gaussian distribution with zero mean and standard deviation σ_{T_i}. We then perform the hemispherical comparison on the new T values. This process of randomization of T and search for asymmetry is repeated 1000 times for the three distance ranges. Figure 3.5 shows the distribution of D_{max} obtained from this MC analysis.

In 99.9% of these realizations, $p(D_{max})$ is lower than 1.5×10^{-58}, 4.2×10^{-58}, and 3.2×10^{-96} for V_{CMB} <7,000, 10,000, and 14,000 km/s, respectively. For the V_{CMB} <7,000 km/s range, the direction $\hat{r}_{max}$ remains exactly the same in 73.4% of the realizations, while in the rest $\hat{r}_{max}$ is within 9°.1 of the observed direction. For the sample with V_{CMB} <10,000 km/s, 83.3% of the cases yield the same $\hat{r}_{max}$ and the rest have an $\hat{r}_{max}$ within 7°.4 of the observed direction. Finally, for the distance range V_{CMB} <14,000 km/s, in all 1000 realizations the direction $\hat{r}_{max}$ remains exactly the same as the observed direction. Therefore, shuffling T within σ_T has little to no effect on the direction of the asymmetry found in these distance limited samples.

In Figure 3.6, we show the distribution of galaxy morphologies for the three radial velocity ranges in our study in the equatorial coordinate system[8]. The black dotted line is the plane of the ecliptic, and the red solid line is the plane separating the pair of hemispheres corresponding to D_{max} for each case. As can be seen, the observed hemispherical asymmetry is very close to both the ecliptic plane and the celestial equator for $V_{CMB} < 7,000$ km/s, but is closer to the celestial equator for $V_{CMB} < 10,000$ and 14,000 km/s. In the case of $V_{CMB} < 14,000$ km/s, the number of galaxies in the analysis increases by more than 30% with respect to this number for $V_{CMB} < 10,000$ km/s; however, the direction of $\hat{r}_{max}$ does not change. We can clearly see a region to the south of the celestial equator occupied mostly with early-type galaxies and the northern sky is more populated by late-type galaxies.

3.5 Discussion

At the moment, our results cannot be compared with other studies because this is the first time that the isotropy of galaxy morphological types has been investigated. The previous statistical studies of the morphological types (e.g., Nair & Abraham 2010, and de Lapparent et al. 2011) were limited to only a fraction of the sky. The studies on the isotropy of the number distribution of galaxies by Gibelyou

[8] All of our analyses were done in the Galactic coordinate system; plotting the distribution of T in the equatorial coordinate system is only to help see the observed alignments more easily.

& Huterer (2012) and Alonso et al. (2015) and on the isotropy of the luminosity function of galaxies by Appleby & Shafieloo (2014a) did not report a significant deviation from isotropy, but their reported directions are relatively close to the direction of the CMB dipole. The studies by Yoon et al. (2014) and Bengaly et al. (2016) of the isotropy of the galaxy number counts both found (with low significance) similar dipole directions of $(l, b) = (310, -15)$ and $(l, b) = (323, -5)$ that are different from the above-mentioned studies, but are not far from the $-\hat{r}_{max}$ directions in our study.

3.5.1 Sample selection effects

Since the anisotropy we found in the distribution of morphological types is very significant and unexpectedly aligned with the CNP and ENP, it is necessary to examine the results more closely. In this section we discuss the cases regarding our sample that could affect the results.

Including the galaxies without M_B

As we mentioned in Section 3.2, the galaxies that do not have an available M_B in the HyperLeda database were excluded from our analysis. Although they constitute only about 5% of the galaxies with T, we checked their effect on the results. We repeated the hemispherical comparison analysis for the whole sample of galaxies with $V_{CMB} < 14,000$ km/s, this time including the ≈ 3000 galaxies without M_B. The direction with the greatest difference remains exactly the same and $D_{max} = 0.124$. Hence, including these galaxies does not affect the final results.

Excluding galaxies with large error on T

Here we applied a strict cut and excluded all the galaxies with $\sigma_T \geq 3.0$ from the whole sample with $V_{CMB} < 14,000$ km/s, which left us with 50,195 galaxies for the analysis. The hemispherical comparison again results in exactly the same direction and a slightly smaller difference, $D_{max} = 0.121$. Therefore, excluding the galaxies with large error on T does not have a significant effect on the results either.

Distance tomography

The subsamples we considered are not independent of each other, i.e., the whole sample with all the galaxies within $V_{CMB} < 14,000$ km/s includes the other two samples with V_{CMB} <7,000 and 10,000 km/s. Here we repeat the hemispherical comparison analysis for the two independent subsamples of galaxies with 7,000< V_{CMB}/(km/s) <10,000, and 10,000< V_{CMB}/(km/s) <14,000. For the first sample, $D_{max} = 0.132$ and $p(D_{max}) = 4.6 \times 10^{-63}$, and for the second sample, $D_{max} = 0.203$ and $p(D_{max}) = 9.0 \times 10^{-139}$. For both of them, the direction $\hat{r}_{max}$ is $(l, b) = (118.1, 30.0)$, i.e., exactly the same as those of the samples with V_{CMB} <10,000 and 14,000 km/s (see Table 4.3). The KS test shows that the distance range 10,000< V_{CMB}/(km/s) <14,000 has the greatest asymmetry in the distribution of T. The overall results remain unchanged.

Applying a magnitude limit to the sample

The factor that is more likely to affect the results is that a large number of galaxies within 14,000 km/s in the HyperLeda database do not have a T value. Had we known the morphological types of these galaxies, the result could be different. Unfortunately, this information is not available at the moment.

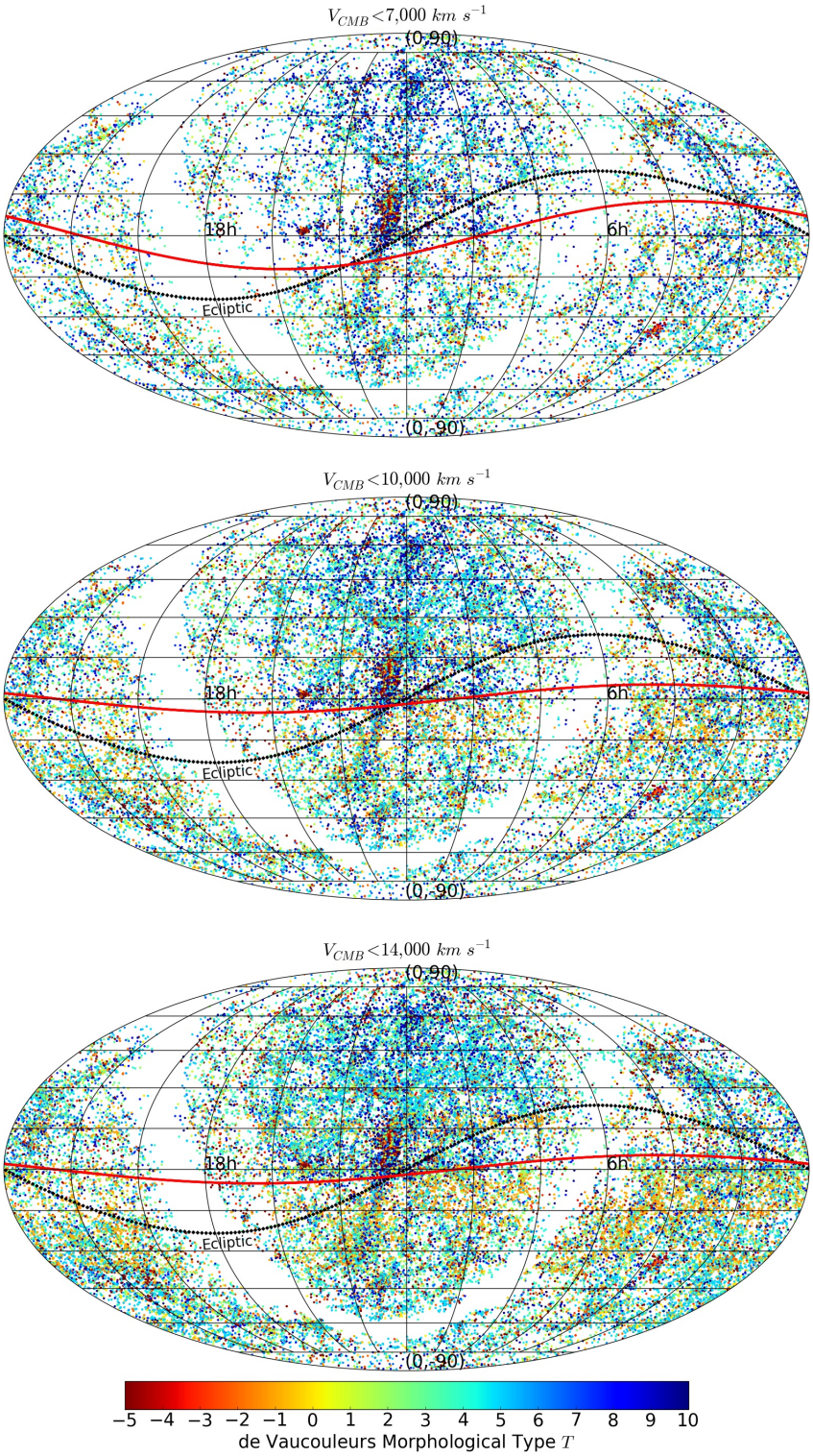

Figure 3.6: Equatorial coordinate system distribution of all the galaxies in the HyperLeda database with measured T and M_B, from top to bottom corresponding to V_{CMB} <7,000, 10,000, and 14,000 km/s. The color code is T, the empty parts are the region around the disk of the Milky Way, the plane of the ecliptic is shown with a dotted line, and the pair of hemispheres with the greatest difference in the distribution of morphologies are divided by a red solid line.

However, we can test the effect of completeness by limiting the analysis to all the galaxies brighter than a certain magnitude. We put a conservative magnitude limit and confine our hemispherical comparison analysis to the galaxies with B≤ 15 mag. The galaxy sample from HyperLeda with $V_{CMB} < 14,000$ km/s and B≤15 mag is around 99% complete, i.e., around 99% of galaxies in the database with these two conditions have a T value. This is the same for the samples with V_{CMB} <7,000 and 10,000 km/s and the same magnitude limit. The results of the hemispherical comparison for the three distance ranges are shown in Table 3.4. We see that the D_{max} values are lower than the values for the samples without the magnitude limit. Although the level of anisotropy decreases and the values of $p(D_{max})$ are orders of magnitude higher than those for the samples without the B≤ 15 mag limit, they are still quite low and the KS result is still very significant (compare the values of $p(D_{max})$ to those of $p(D_{min})$ which are also listed in Table 3.4). The direction of $\hat{r}_{max}$ did not change for the range V_{CMB} <7,000 km/s; however, for V_{CMB} <10,000 and 14,000 km/s, the $\hat{r}_{max}$ is farther away from the ENP, but interestingly is even more aligned with the CNP having only a 2°.6 angular separation.

We apply the MC method explained and used in Section 3.4.4 to check the effect of shuffling T within σ_T on the anisotropy observed in these samples. For V_{CMB} <10,000 and 14,000 km/s, 97.2% and 99.9% of the realizations have their $\hat{r}_{max}$ within 32°.0 of the observed direction[9], and all the realizations have their $p(D_{max})$ lower than 2.2×10^{-5} and 6.8×10^{-7}, respectively. However, in the case of the sample with V_{CMB} <7,000 km/s, only 17.0% of the realizations have their $\hat{r}_{max}$ within 32°.0 of the observed direction, the rest have their $\hat{r}_{max}$ towards various directions and ranging to more than 80°.0 away from the observed $\hat{r}_{max}$. Although shuffling T within σ_T washes out the asymmetry in the sample with V_{CMB} <7,000 km/s and B≤ 15 mag, the anisotropy in the samples with V_{CMB} <10,000 and 14,000 km/s and B≤ 15 (especially the latter) remain significantly close to the observed direction of $\hat{r}_{max}$.

Figure 3.7 shows the number distribution of different T values in the hemisphere pairs corresponding to D_{max} for the magnitude limited samples. We also show the difference in the number of each T bin between the two hemispheres. The greatest difference is for the galaxies with $-5 \leq T \leq -4$, $-3 \leq T \leq -2$, $3 \leq T \leq 4$, and $5 \leq T \leq 6$, in the order of relative difference. Based on these number differences we see that if ≈ 30% of galaxies with $3 \leq T \leq 4$ in the north and ≈ 34% of galaxies with $5 \leq T \leq 6$ in the south had their morphological types in the range $4 \leq T \leq 5$, and at the same time ≈ 35% of galaxies with $-5 \leq T \leq -4$ in the north and ≈ 40% of galaxies with $-3 \leq T \leq -2$ in the south had their morphological types in the range $-4 \leq T \leq -3$, then the anisotropy would be partially alleviated. However, even in this case, the number of galaxies with $4 \leq T \leq 5$ would be ≈ 17% more in the south and the number of galaxies with $-4 \leq T \leq -3$ would be ≈ 25% more in the north. Actually, it is not straightforward to tell what sort of shift in the T values will remove the asymmetry. Figure 3.8 shows the distribution of the morphological types of the magnitude limited samples in the equatorial coordinate system. By comparing this with Figure 3.6 we can see that the obvious sharp contrast between the north and the south in the case of the V_{CMB} <10,000 and 14,000 km/s samples is no longer visible, but the hemispherical asymmetry (shown by the red solid curve) is more aligned with the celestial equator. Applying the $B \leq 15.0$ mag limit reduces the level of anisotropy, but does not remove it.

However, given that the sky coverage of the distance limited sample is fairly uniform and covers a wide range of apparent magnitude as well as a full range of distances, and that the two hemispheres with the greatest difference have a similar number of galaxies, the question is raised as to why the distance limited sample, though incomplete, should be biased by a certain type of galaxy in one hemisphere and

[9] We chose the value 32°.0 because it is the maximum angular separation of $\hat{r}_{max}$ for 99.9% of the realizations of the sample with V_{CMB} <14,000 km/s and B≤ 15 mag.

Table 3.4: Results for the samples with B≤15 mag. With this magnitude limit, around 99% of the galaxies in the HyperLeda database within all three radial velocity ranges in our study have a T value. We note that for the V_{CMB} <10,000 and 14,000 km/s samples, the direction of $\hat{r}_{max}$ is only 2°.6 away from the celestial north pole.

V_{CMB} (km/s) <	$\hat{r}_{max} = (l, b)$	α_{CNP}	α_{ENP}	D_{max}	$p(D_{max})$	D_{min}	$p(D_{min})$
7,000	(112.5,35.7)	12°.3	14°.7	0.071	1.5×10^{-22}	0.016	0.15
10,000	(123.7,24.6)	2°.6	24°.8	0.069	2.2×10^{-31}	0.010	0.48
14,000	(123.7, 24.6)	2°.6	24°.8	0.074	4.7×10^{-43}	0.009	0.44

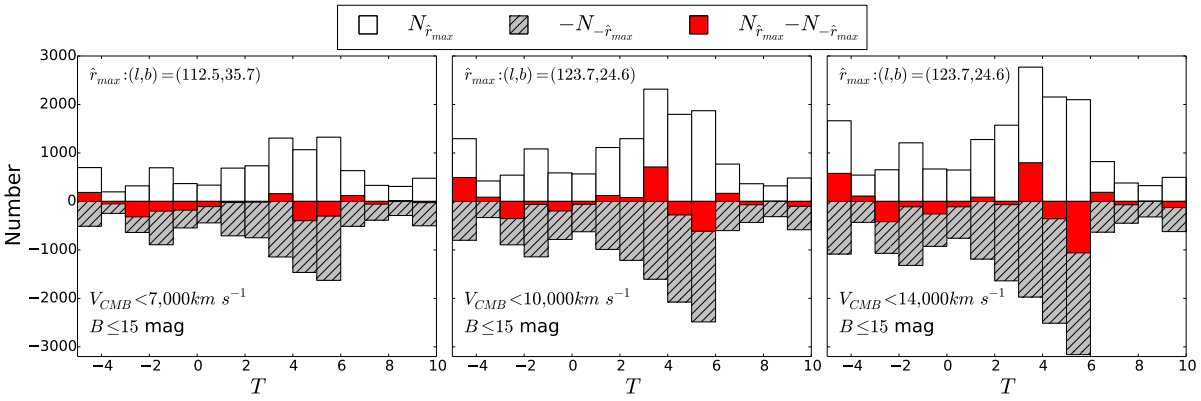

Figure 3.7: Distribution of morphologies in the hemispheres towards $\hat{r}_{max}$ (positive numbers) and $-\hat{r}_{max}$ (negative numbers) for the samples with B≤15 mag, from left to right corresponding to V_{CMB} <7,000, 10,000, and 14,000 km/s. The number difference between the two hemispheres for each T is shown by red bars.

by a different type in the opposite one.

3.6 Summary and conclusion

We presented the first probe of isotropy of the distribution of morphological types of galaxies in the Local Universe. Using the de Vaucouleurs morphological types of more than 60,000 galaxies with radial velocity V_{CMB} <14,000 km/s (corresponding to a distance within ≈200 Mpc) from the HyperLeda database, we searched for any directional difference in the distribution of morphological types. We used a hemispherical comparison method and by dividing the sky into two opposite hemisphere pairs, compared the frequency of morphological types, T, using a Kolmogorov-Smirnov test. The KS test was applied to hemisphere pairs with the axis of symmetry pointing at the centers of the pixels of a HEALPix grid. This gave us all-sky maps of the KS statistics, D. We performed this analysis for three radial velocity ranges, i.e., for galaxies with V_{CMB} <7,000, 10,000, and 14,000 km/s (corresponding to distances of about 100, 150, and 200 Mpc).

The directions $\hat{r}_{max}$ corresponding to the hemisphere pairs with the greatest difference, D_{max}, were found to be similar for the three distance ranges. These directions are very far from the directions with the greatest difference in the number of galaxies. Under the assumption that the galaxy morphologies should be statistically isotropic in the distance ranges under consideration, the probability of obtaining the observed difference or greater from the KS distribution, $p(D_{max})$, was found to be $\leq 10^{-133}$. In addition,

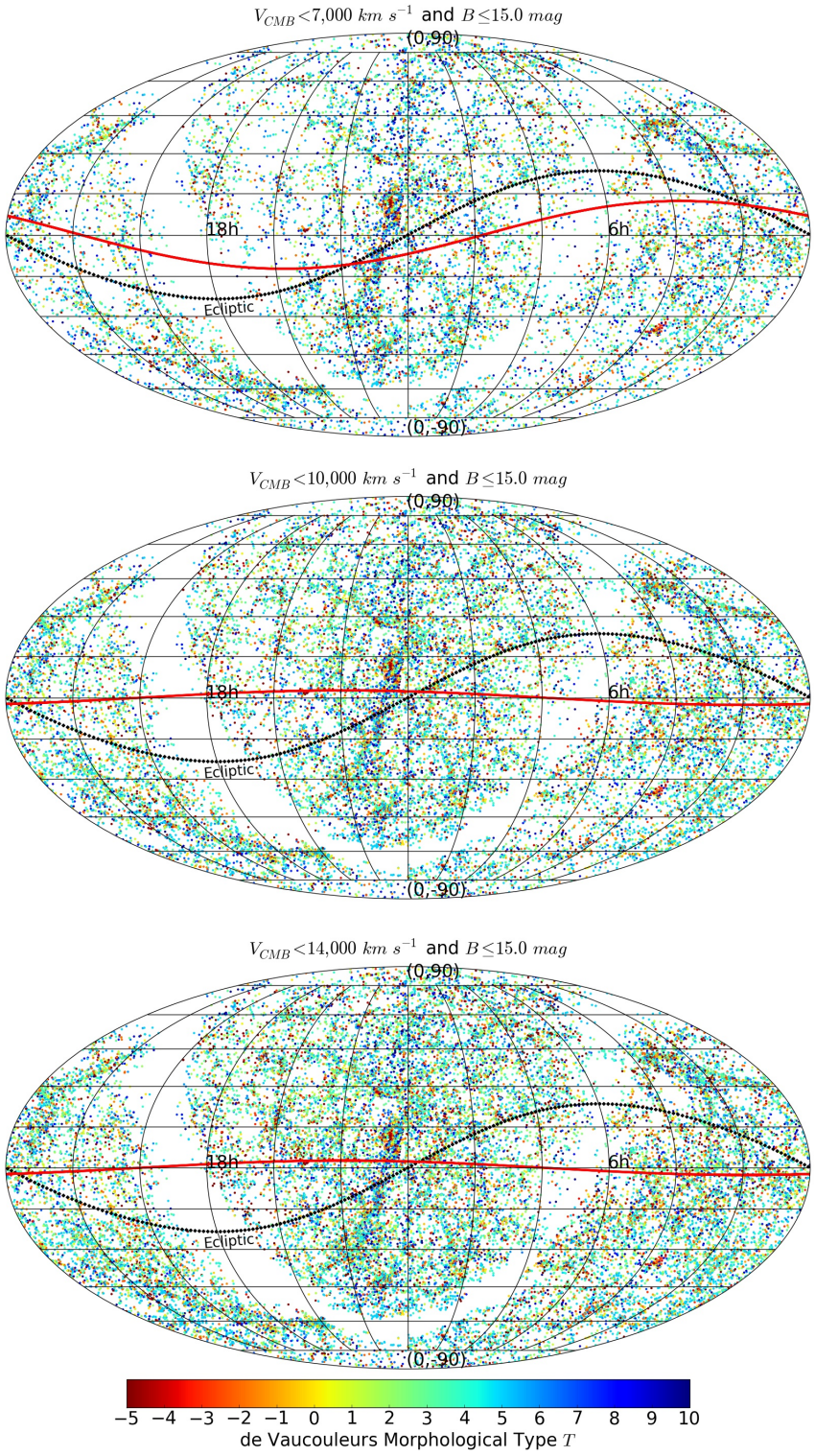

Figure 3.8: Equatorial coordinate system distribution of all the galaxies in the HyperLeda database with $B \leq 15.0$ mag and measured T and M_B, from top to bottom corresponding to V_{CMB} <7,000, 10,000, and 14,000 km/s. The color code is T, the empty parts are the region around the disk of the Milky Way, the plane of the ecliptic is shown with a dotted line, and the pair of hemispheres with the greatest difference in the distribution of morphologies are divided by a red solid line. Though the sharp contrast seen in Figure 3.6 is no longer visible, the hemispherical asymmetry obtained from the KS test is even more aligned with the celestial equator for galaxies with V_{CMB} < 10,000 and 14,000 km/s.

using a Monte Carlo analysis and by creating 1000 isotropic realizations, the number of realizations with equal or higher D_{max} was found to be zero and the highest values of D_{max} obtained from the 1000 realizations were found to be an order of magnitude lower than the observed values.

Interestingly, the hemispherical asymmetry that we found in the distribution of the morphological types of galaxies is aligned with both the ecliptic and the celestial equator planes. The direction $\hat{r}_{max}$ for the sample with V_{CMB} <7,000 km/s is only 12°.3 and 14°.7 away from the celestial and the ecliptic north poles, respectively. Using our Monte Carlo analysis with 1000 isotropic realizations, we quantified the significance of the alignment with the ecliptic to be at the 97.6% confidence level, and that of the alignment with the celestial equator to be at the 97.1% (both not taking into account the extreme significance obtained from the KS test). It may be interesting to note that the hemispherical asymmetry in the CMB power spectrum discovered in the *WMAP* data and confirmed by the *Planck* satellite is also aligned with the plane of the ecliptic (Planck Collaboration et al. 2014b).

For the other two samples with V_{CMB} <10,000 and 14,000 km/s, the observed anisotropy is aligned with the celestial equator at the 99.8% confidence level, with an angular separation of only 5°.1. In general, when looking at the sky distribution of morphological types of the whole sample ($V_{CMB} < 14,000$ km/s), the northern sky is more populated by late-type galaxies whereas early-type galaxies are the dominant type in the southern sky. In particular, the greatest difference in the abundance of morphological types is observed to be related to the galaxies with $9 \leq T \leq 10$ (i.e., Sm and Im types) whose number is two times higher towards the northern sky, and the galaxies with $-1 \leq T < 0$ (i.e., $S0^+$ types) whose number is more than twice as high in the southern sky. Excluding galaxies with large uncertainty on T (i.e., $\sigma_T \geq 3.0$) does not affect the direction of the asymmetry. Also, repeating the analysis on the independent subsamples of galaxies with 7,000< V_{CMB} (km/s)<10,000 and 10,000< V_{CMB} (km/s)<14,000 yields similar directions for the greatest difference in the distribution of T.

To increase the completeness of our sample, we applied a conservative magnitude limit and included only the galaxies with $B \leq 15.0$ mag in our analysis. This resulted in a decrease in the values of D_{max}, though still with a small probability of consistency with the null hypothesis of isotropy of $p(D_{max}) \leq 10^{-21}$ for all three distance ranges. For the sample with V_{CMB} <7,000 km/s, the direction of $\hat{r}_{max}$ remained unchanged with respect to the sample without the magnitude limit; however, for the samples with V_{CMB} <10,000 and 14,000 km/s and $B \leq 15.0$ mag the direction of $\hat{r}_{max}$ was found to be closer to the celestial north pole with only 2°.6 angular separation, i.e., the hemispherical asymmetry is even more aligned to the celestial equator than in the samples with the same distance ranges but without the magnitude limit.

Using an additional 1000 Monte Carlo realizations in each of which the T values are shifted randomly within their uncertainties, we quantified the effect of random errors on the anisotropy in the distance limited samples to be negligible. However, for the V_{CMB} <7,000 km/s and $B \leq 15.0$ mag sample, shuffling T within σ_T can change the direction of anisotropy towards various directions in each realization, meaning that the anisotropy in this sample is not significant. On the other hand, in 97.2% and 99.9% of the realizations for V_{CMB} <10,000 and 14,000 km/s and $B \leq 15.0$ mag, the direction $\hat{r}_{max}$ is within 32°.0 of the observed direction showing that the anisotropy in these samples (especially in the latter one) is robust against the effect of random errors. For these two samples, the number of galaxies with $-5 \leq T < -4$ and with $3 \leq T < 4$ is respectively around 50% and 40% higher and the number of galaxies with $-3 \leq T < -2$ and $5 \leq T < 6$ is respectively around 40% and 34% lower in the northern sky. A simple shift (e.g., +1 or -1) in the T values of one hemisphere does not decrease the value of D_{max} (it

actually increases it in most cases). Various combinations of shifts in T around $-5 \leq T < -2$ and around $3 \leq T < 6$ can only partially alleviate the tension in the number of morphological types between north and south.

If this significant deviation from isotropy is real and not due to issues with the catalog and the classifications, it could mean that the galaxies in these two opposite directions have different evolution and/or formation histories which would be a major challenge for the Cosmological Principle. However, the fact that the asymmetry has an equatorial north-south alignment indicates that most probably its source is a systematic bias in the classification of morphological types between the data of the northern and the southern sky possibly because different telescopes (with different systematics) were used to observe these galaxies.

The morphological types cataloged in RC3 and the HyperLeda database have been used for many studies, and some other catalogs and online databases extract the morphological information from them. Our results indicate that some of the studies based on this morphological information may need to be reconsidered. In addition, we should not forget that these classifications have mostly been done visually and it is necessary to put even more effort into making well-defined quantitative and automated approaches for morphological classifications. Further investigations are indispensable in order to uncover the exact reason for the anisotropy we found in this study.

Acknowledgements

We thank the referee for the critical and constructive comments. We are very grateful to Dmitry Makarov for his kind and helpful correspondence and very useful information on the HyperLeda database. We thank Christian Henkel and David Martinez-Delgado for useful discussions; Jan Pflamm-Altenburg, Cristiano Porciani, Fateme Kamali, and Hosein Haghi for their constructive comments; Jens Erler for his kind help with HEALPix; and Michael Marks and Patrick Simon for useful discussions on statistics. We acknowledge the usage of the HyperLeda database (http://leda.univ-lyon1.fr), HEALPix package, and the matplotlib plotting library.

CHAPTER 4

DGSAT: Dwarf Galaxy Survey with Amateur Telescopes
I. Discovery of low surface brightness systems around nearby spiral galaxies

Abstract

We introduce the Dwarf Galaxy Survey with Amateur Telescopes (DGSAT) project and report the discovery of eleven low surface brightness (LSB) galaxies in the fields of the nearby galaxies NGC 2683, NGC 3628, NGC 4594 (M104), NGC 4631, NGC 5457 (M101), and NGC 7814. The DGSAT project aims to use the potential of small-sized telescopes to probe LSB features around large galaxies and to increase the sample size of the dwarf satellite galaxies in the Local Volume. Using long exposure images, fields of the target spiral galaxies are explored for extended low surface brightness objects. After identifying dwarf galaxy candidates, their observed properties are extracted by fitting models to their light profiles. We find three, one, three, one, one, and two new LSB galaxies in the fields of NGC 2683, 3628, 4594, 4631, 5457, and 7814, respectively. In addition to the newly found galaxies, we analyse the structural properties of nine already known galaxies. All of these 20 dwarf galaxy candidates have effective surface brightnesses in the range $25.3 \lesssim \mu_e \lesssim 28.8$ mag.arcsec^{-2} and are fit with Sersic profiles with indices $n \lesssim 1$. Assuming that they are in the vicinity of the above mentioned massive galaxies, their r-band absolute magnitudes, their effective radii, and their luminosities are in the ranges $-15.6 \lesssim M_r \lesssim -7.8$, 160 pc $\lesssim R_e \lesssim 4.1$ kpc, and $0.1 \times 10^6 \lesssim \left(\frac{L}{L_\odot}\right)_r \lesssim 127 \times 10^6$, respectively. To determine whether these LSB galaxies are indeed satellites of the above mentioned massive galaxies, their distances need to be determined via further observations. Using small telescopes, we are readily able to detect LSB galaxies with similar properties to the known dwarf galaxies of the Local Group.

Note: This chapter is a reprint of a paper of the same title published in the Astronomy & Astrophysics journal. Credit: **B. Javanmardi**, D. Martinez-Delgado, P. Kroupa, C. Henkel, K. Crawford, K. Teuwen, R. J. Gabany, M. Hanson, T. S. Chonis and F. Neyer, A&A, 588, A89, 2016, reproduced with permission ©ESO.

4.1 Introduction

Dwarf galaxies are the most common type of galaxies in the universe and are crucial in testing different models of galaxy formation and evolution (Gallagher & Wyse 1994). The properties of dwarf satellite galaxies are important for testing cosmological and gravity models on small scales (Gentile et al. 2007; Kroupa et al. 2010; Lelli et al. 2015; Flores et al. 2016), and the spacial and velocity distributions of these small galaxies around their hosts probe structure formation models on scales of hundreds of kpc (Kroupa et al. 2005; Kroupa 2012, 2015). López-Corredoira & Kroupa (2016b) emphasize how different models lead to different predictions on the phase-space correlation, or lack thereof, of satellite galaxies.

In the framework of the standard cosmological model, galaxies form in a hierarchical process. This scenario faces challenges in providing convincing predictions for the properties of the galaxies in the Local Group (LG). The number of observed satellite galaxies in the LG is much smaller than the predicted number of substructures based on numerical simulations (the "missing satellite" problem; Klypin et al. 1999; Moore et al. 1999; Bullock 2010; Kravtsov 2010). Furthermore, the majority of the most massive predicted substructures are dense enough to trigger star formation and hence be observable (the "too big to fail" problem; Boylan-Kolchin et al. 2011). These small-scale problems are often seen as mild tensions that can be resolved with the complex processes acting amongst the constituents of the Standard Model of particle physics, i.e. owing to baryonic physics that is not well understood (e.g. Del Popolo et al. 2014). Problems and successes of the standard models based on dark matter are reviewed by Del Popolo (2014).

In addition to these small-scale tensions, on scales spanning 10s up to hundreds of kpc, the satellites of the Milky Way (MW) and the Andromeda (M31) galaxies are not distributed approximately isotropically (as expected from the standard galaxy formation scenario) around these two massive galaxies, but instead, they are located in thin disks and seem to have correlated orbits (Kroupa et al. 2005; Pawlowski et al. 2012, 2014, 2015a,b; Pawlowski & McGaugh 2014; Pawlowski & Kroupa 2014; Ibata et al. 2013, 2014, 2015). Furthermore, the MW and M31 satellites planes appear to be mutually correlated, and the distribution of all non-satellite LG galaxies is highly symmetrical in two planes equidistant from the line joining the MW and M31 (Pawlowski et al. 2013). And last but not least, the number of satellites of the main galaxies of the LG (i.e. M33, MW and M31) seem to be correlated with the masses of their bulges, amongst other problems (Kroupa et al. 2010; Kroupa 2015; López-Corredoira & Kroupa 2016b).

Although these features have been mostly observed and studied in the LG, where the best spacial three-dimensional and kinematical data are available, Chiboucas et al. (2013) have already noted the anisotropic distribution of dwarf galaxies in the nearest galaxy group, M81, which resembles the anisotropies evident in the LG. However, further observations are needed to find out if LG properties are also typical in case of other galaxy groups. For this reason, it is vital to conduct various systematic searches for dwarf satellite galaxies beyond the Local Group (McConnachie 2012; Chiboucas et al. 2013; Sand et al. 2014; Spencer et al. 2014; Koda et al. 2015; Muñoz et al. 2015; Sand et al. 2015; Crnojević et al. 2015; Giallongo et al. 2015; Davies et al. 2016; Makarov et al. 2015).

Recently, the potential of small-sized telescopes as tools for probing the low surface brightness (LSB) features in the nearby universe has been proposed and tested successfully. In recent years, the Stellar Tidal Stream Survey (STSS; PI. Martinez-Delgado) has obtained deep wide-field images of nearby spiral galaxies that showed evidence of being surrounded by diffuse light over-densities (Martínez-Delgado et al. 2008, 2010, 2015a). This observational effort has clearly revealed previously undetected stellar streams, which makes this survey the largest sample of stellar tidal structures in the local Universe so far. Similarly, Karachentsev et al. (2014, 2015) used small telescopes and long exposure imaging to visually search for LSB galaxies in the Local Volume. Also, the Dragonfly telephoto array of eight photographic lenses reported the discovery of seven LSB galaxies in the field of M101 (Merritt et al. 2014).

In this paper, we present the Dwarf Galaxy Survey with Amateur Telescopes (DGSAT), a pilot survey that exploits the deep images obtained by the STSS during recent years to complete the census of very faint dwarf satellites around our spiral galaxy targets (that are mainly Milky Way analogs). The first result of this project was the discovery of DGSAT I, a faint diffuse field galaxy behind the Andromeda galaxy, which turned out to be an ultra-diffuse galaxy associated with the Pisces-Perseus supercluster (Martínez-Delgado et al. 2015b). In this work, we present the results of our search for faint companions around six nearby Milky Way-like galaxies of the Local Volume, namely NGC 2683, NGC 3628, NGC 4594 (M104), NGC 4631, NGC 5457 (M101), and NGC 7814. Throughout this work, the adopted distances and distance moduli for these galaxies are the mean values given by the NASA/IPAC Extragalactic Database (NED)[1].

This manuscript is organized as follows. The observations are explained in Section 4.2. We describe our automated data calibration in Section 4.3 and our searching strategy and parameter extraction in Section 4.4 . Our results for each individual field are presented in Section 4.5 and discussed in Section 4.6. Finally, we summarize our results is Section 4.7.

4.2 Observations

Detecting faint features in the halos of spiral galaxies requires wide-field, deep images taken in very dark sky conditions and with exquisite flat-field quality over a wide region (> 30 arcmin) around the targets. Our survey strategy strives for multiple deep exposures of each target using high throughput clear filters with near-IR cut-off, known as luminance (L) filters (4000 Å< λ <7000 Å; see Fig. 1 in Martínez-Delgado et al. 2015a) and a typical exposure time of 7-8 hours. Our typical 5σ surface brightness detection limit (measured in random ~3 arcsec diameter apertures) is ~ 28.5 and 28 mag/arcsec^2 in g and r bands, which is approximately three magnitudes deeper than the Sloan Digital Sky Survey (SDSS) II images (Martínez-Delgado et al. 2010). From a direct comparison with SDSS data, we find that our images are ten times deeper than this survey in terms of photon statistics with comparable systematic background uncertainties (Martínez-Delgado et al. 2010; Cooper et al. 2011).

The observations of DGSAT were conducted with a network of privately owned robotic observatories equipped with modest-sized telescopes (0.1-0.8 meter) located in Europe, the United States, Australia, and Chile. Each observing location features spectacularly dark, clear skies with seeing below 1.5″. The list of participating facilities that have provided data for this paper is given in Table 4.1. Each telescope is equipped with a latest generation astronomical commercial CCD camera, using in the majority of the cases a film-format, 16 mega pixel imaging sensor composed of a 4096 × 4096 pixel array with 9 × 9 micron pixels. The fields of view and pixel scales resulting from the telescope and camera combinations are listed in Table 1. Additionally, our survey uses portable apocromatic refractors (with a typical aperture of 0.1 - 0.15 m) for achieving wider fields around those nearby galaxies with an extended apparent size (e.g. M101). The data reduction follows standard techniques (zero level subtraction and first order flat-field corrections from a large number of dome and twilight flat frames) using pipelines successfully proven during the STSS (Martínez-Delgado et al. 2008, 2010, 2015a).

[1] The NED is operated by the Jet Propulsion Laboratory, California Institute of Technology, under contract with the National Aeronautics and Space Administration.

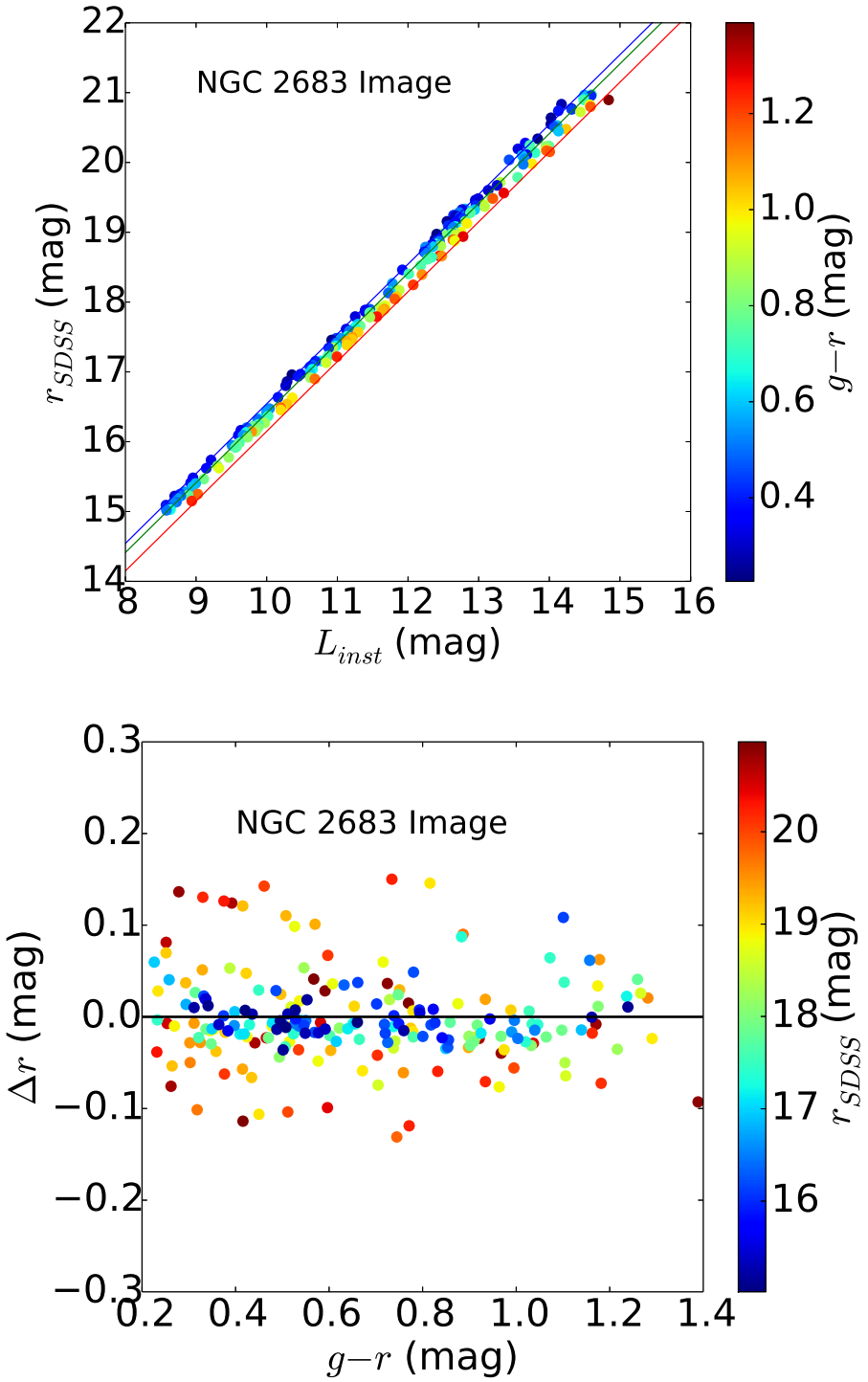

Figure 4.1: An example of the results of calibration to the SDSS r-band for the NGC 2683 field. Top: SDSS r magnitude r_{SDSS} of the calibrating stars in the image compared to the corresponding instrumental measurement L_{inst} ; the colour code is $(g-r)$. The red, green, and blue solid lines are the r_{cal} from Eq. 4.1 evaluated at the maximum (reddest), median, and minimum (bluest) of the $(g-r)$ values of the sample, respectively. Bottom: magnitude residuals after calibration, $\Delta r = r_{SDSS} - r_{cal}$, vs. $(g-r)$; the colour code is r_{SDSS}. No dependency on $(g-r)$ remains. The standard deviation of the residuals in this particular case is 0.05 mag and we reach similar accuracy in calibration of the rest of images (see Table 4.2).

Table 4.1: Target galaxies in order of NGC numbers, observatory, location, telescope and its focal ratio f/ used for observing, observation dates, total exposure time, t_{exp} (in seconds), field of view (FOV) (in arcmin^2), and pixel scale (in arcsec) of the images.

Target	Observatory	Location	Telescope	f/	Obs. Date	t_{exp} (s)	FOV (arcmin^2)	pixel scale (arcsec/pix)
NGC 2683	ROSA(POLLUX)	Verclause, France	Newton 0.4-m	3.5	Feb-Mar 2015	24000	81×81	1.22
NGC 3628	DGRO-Rancho Hidalgo	New Mexico, USA	RCOS 0.36-m	7.9	Dec 2011	36000	43×43	0.62
NGC 4594	Riverdingo	Adelaide, Australia	RCOS 0.36-m	7.9	Apr 2009	25200	43× 43	0.62
NGC 4631	Black Bird	New Mexico, USA	RCOS 0.5-m	8.1	May-Nov 2011	63000	31× 31	0.43
NGC 5457	ROSA(POLLUX)	Verclause, France	Newton 0.4-m	3.5	Apr-May 2014	75600	81×81	1.22
NGC 5457	Antares	Gossau, Switzerland	TEC140 APO	7.2	Feb - May 2012	87600	121×80	1.82
NGC 7814	Rancho del Sol	California, USA	RCOS 0.5-m	8.3	Aug 2013	40800	29×29	0.43

4.3 Data calibration

We developed a semi-automatic pipeline for calibrating our flux measurements to the SDSS r-band, as explained below. Since the applied Luminance filter, L, is a wide band filter that almost covers the entire SDSS g and r bands, a colour dependency is expected between the instrumental magnitude measurement, L_{inst}, and r magnitude. Therefore, the calibration takes the form

$$r_{cal} = c_0 L_{inst} + c_1(g - r) + c_2, \tag{4.1}$$

where r_{cal} is the calibrated r magnitude, c_0 tunes the linear relation between r and L_{inst}, c_1 corrects the colour dependency, and c_2 is just a magnitude zero-point correction. These calibrating parameters are determined via taking a maximum likelihood approach and minimising the function

$$\chi^2(c_j) = \sum_{i}^{N_{star}} \frac{[c_0 L_{inst,i} + c_1(g - r)_i + c_2 - r_i]^2}{\sigma^2_{L_{inst,i}}}, \tag{4.2}$$

where $\sigma_{L_{inst}}$ is the uncertainty of the instrumental flux measurement and N_{star} is the number of calibrating stars. To minimize the effect of human bias, we do not select "good stars" for calibrating, but those that are used for the final calibration are selected automatically via the following approach. In our pipeline, first the SExtractor (Bertin & Arnouts 1996) is run on the image (or a portion of it, depending on the field of view and the number of available stars) to detect and measure the flux of all the objects in the image. After that, the coordinates of our detected objects are cross-identified with the SDSS DR12 catalogue[2] and only the stars with magnitude $r \geq 15$ pass to the next step. The reason for this magnitude cut is that Chonis & Gaskell (2008) found that the SDSS photometry suffers from saturation effects around $g, r, i \approx 14$ mag. In the next step, the stars outside the colour ranges $0.08 < (r - i) < 0.5$ and $0.2 < (g - r) < 1.4$ are rejected since they behave non-linearly in the $(r - i)$ vs. $(g - r)$ space (see Chonis & Gaskell 2008). After this, we have a large number of stars (different for various images) with g and r magnitudes from SDSS and the L_{inst} from FLUX-AUTO given by the SExtractor. Using these stars, our code minimizes the χ^2 in eq. (4.2) for the first estimation of the c_j with which r_{cal} (from eq. 4.1) and $\Delta r = r_{SDSS} - r_{cal}$ are computed. At the next step, the 3σ outliers from the best-fit result (i.e. the stars with $\Delta r > 3\sigma$) are rejected, where σ is the standard deviation of Δr. The fitting is repeated with the remaining stars and is followed by another outlier rejection as explained above. This procedure is repeated until the fitting reaches a point where no 3σ outliers remain. Then the final c_j are obtained and the final r_{cal} and

[2] http://skyserver.sdss.org/dr12/en/tools/crossid/crossid.aspx

Table 4.2: Target galaxies in order of NGC numbers, their adopted distances, d, and distance moduli, DM, from the NED, number of final calibrating stars, N_{star}, and final standard deviation in Δr, σ_{cal}, and the 5 σ values of the limiting surface brightness (photon noise) in r band for each image in mag/arcsec^2 using boxes of around 3 arcsec.

Target	d (Mpc)	DM (mag)	N_{star}	σ_{cal} (mag)	Photon Noise (mag/arcsec^2)
NGC 2683	10.5 ± 2.2	30.05 ± 0.50	212	0.05	28.03
NGC 3628	10.9 ± 2.4	30.14 ± 0.53	138	0.07	28.06
NGC 4594	11.1 ± 4.1	30.12 ± 0.69	140	0.08	27.54
NGC 4631	5.8 ± 1.5	28.76 ± 0.58	72	0.08	29.61
NGC 5457	6.8 ± 0.8	29.16 ± 0.26	104	0.05	28.92
NGC 7814	16.4 ± 3.6	31.03 ± 0.49	107	0.05	27.87

Δr are determined. An example of the results of our calibration for the image of the field of NGC 2683 is shown in Figure 4.1. The top panel shows the SDSS r magnitudes of the calibrating stars vs. their instrumental measurement L_{inst} and the bottom panel illustrates that the final magnitude residuals after calibration, Δr, show no dependency on $(g - r)$ colour. The latter means that our colour correction has well accounted for the systematic effects due to the spectral energy distribution of measured objects and the width difference of the transmitting filters. The final number of stars used for the calibration, N_{star}, and the standard deviation of the final residuals, σ_{cal}, (which is added in quadrature to the subsequently reported results) are listed in Table 4.2 for all the images. If one chooses the calibrating stars manually instead of the above explained automatic star selection, a smaller but not necessarily reliable σ_{cal} might be achieved. The method we present here is statistically robust.

The limiting surface brightnesses of our images were determined following the method described in Martínez-Delgado et al. (2010). For estimating the photon noise, we measured the standard deviation of apertures with around 3 arcsec diameter and computed the surface brightness corresponding to five times that standard deviation. The obtained values for each image are listed in Table 4.2.

4.4 Methods of analysis

In this section we explain our searching strategy to find dwarf galaxy candidates and to extract information about their structural properties by light profile fitting. The following two subsections outline our general procedures, while we go into detail later when we discuss individual galaxies.

4.4.1 Searching strategy

To search for low surface brightness galaxies, we use the SExtractor software by Bertin & Arnouts (1996). Though the top-hat convolution filter in this software is suited for detecting extended low surface brightness objects, we do not limit the search only to that filter and run SExtractor several times with different convolution filters and detection thresholds. The detected objects from different runs are matched based on their image coordinates. This gives us a large catalogue of all the objects in the image. We put a size constraint on the detections and remove all the objects with a FLUX-RADIUS smaller than 1.5 times the size of the full width at half maximum (FWHM) of the point spread function (PSF) of the image. This value (which is between 4 to 6 arcsec for our images) seems to be large enough for rejection of most of the stars and small enough to keep the smallest LSB galaxies. Most of the rejected objects are stars

and the rest are bright background galaxies or noise. This cut condition helps to reduce significantly the number of detections that need to be checked visually. Among the surviving detections, most of them are either noise fluctuation, saturated stars and their wings, or galactic cirrus.

4.4.2 Parameter extraction

To determine the structural properties of the dwarf candidates, we fit a Sersic model (Sersic 1968) on them via the GALFIT software developed by Peng et al. (2002). For this purpose, we cut a proper-sized square centred on each dwarf candidate. Depending on the brightness and position of possible neighbouring or overlapping stars, we either mask them, remove them by PSF photometry via IRAF/DAOPHOT software (Stetson 1987) before model fitting, or fit them simultaneously with the dwarf candidate using GALFIT. We repeat the fitting until we reach a good fit by checking the reduced χ^2 (given by GALFIT) and by visually inspecting the model and residual images.

4.5 Results

In this section we report the results of our search for dwarf satellite galaxies. We start with the field of the M101 galaxy, which has the largest number of newly detected dwarf galaxies that have been recently reported by the Dragonfly team (Merritt et al. 2014). Therefore, this galaxy is the proper target to begin with. The other fields, where most of our new detections are located, are reported in order of NGC number.

4.5.1 NGC 5457 (M101) revisited

M101 or the Pinwheel galaxy is a massive spiral galaxy at an adopted distance of 6.8 ± 0.8 Mpc (Table 4.2). The field of M101 has been recently probed by the Dragonfly project (Merritt et al. 2014) for low surface brightness features. They had a $3.^{\circ}3 \times 2.^{\circ}8$ image centred on M101 and were able to discover seven low surface brightness galaxies. We use our $2.^{\circ}0 \times 1.^{\circ}3$ image (Figure 4.2) of the field of this galaxy (which is a combination of two images taken by K. Teuwen and F. Neyer) to revisit the discovered Dragonfly LSBs and look for other possible dwarf galaxy candidates. As they mention in Merritt et al. (2014), their survey is not able to reveal the smallest galaxies because of their relatively large FWHM of around 6.5 arcsec. Our image of the M101 field with an FWHM ≈ 3.2 arcsec (corresponding to around 100 pc at the distance of M101) is more suitable than that of the Dragonfly for revealing small galaxies.

Two of the M101 LSB galaxies discovered by Dragonfly, namely DF2 and DF5, are outside of our image field. With our search strategy explained in Section 4.4.1, we could not only detect DF1, DF3, DF4, DF6 and DF7, but we also find yet another low surface brightness galaxy (the NGC5457-DGSAT-1) which was not reported by the Dragonfly project. This dwarf galaxy candidate was also independently discovered by Karachentsev et al. (2015)[3]. The Dragonfly LSB galaxies and our obtained models for them are shown in Figure 4.3. The top panel is the cut-out portion of the main image centred on each LSB galaxy, the middle panel shows the model obtained by GALFIT and the lower panel is the result of the subtraction of the model from the main image. Prior to the GALFIT modelling, the foreground stars were removed by fitting the PSF model of the image using DAOPHOT. The models can be compared to those reported in Figure 1 of Merritt et al. (2014). For almost all of them, the residual images are clean of the LSB galaxy but in the case of DF4 there remains a bit of unsubtracted light. This galaxy has an attached, elongated tail , which is not visible in the Dragonfly image, and may be caused by tidal

[3] The image of M101 used in our study, taken by the astrophotographer F. Neyer (see Table 4.1), is also used in that paper.

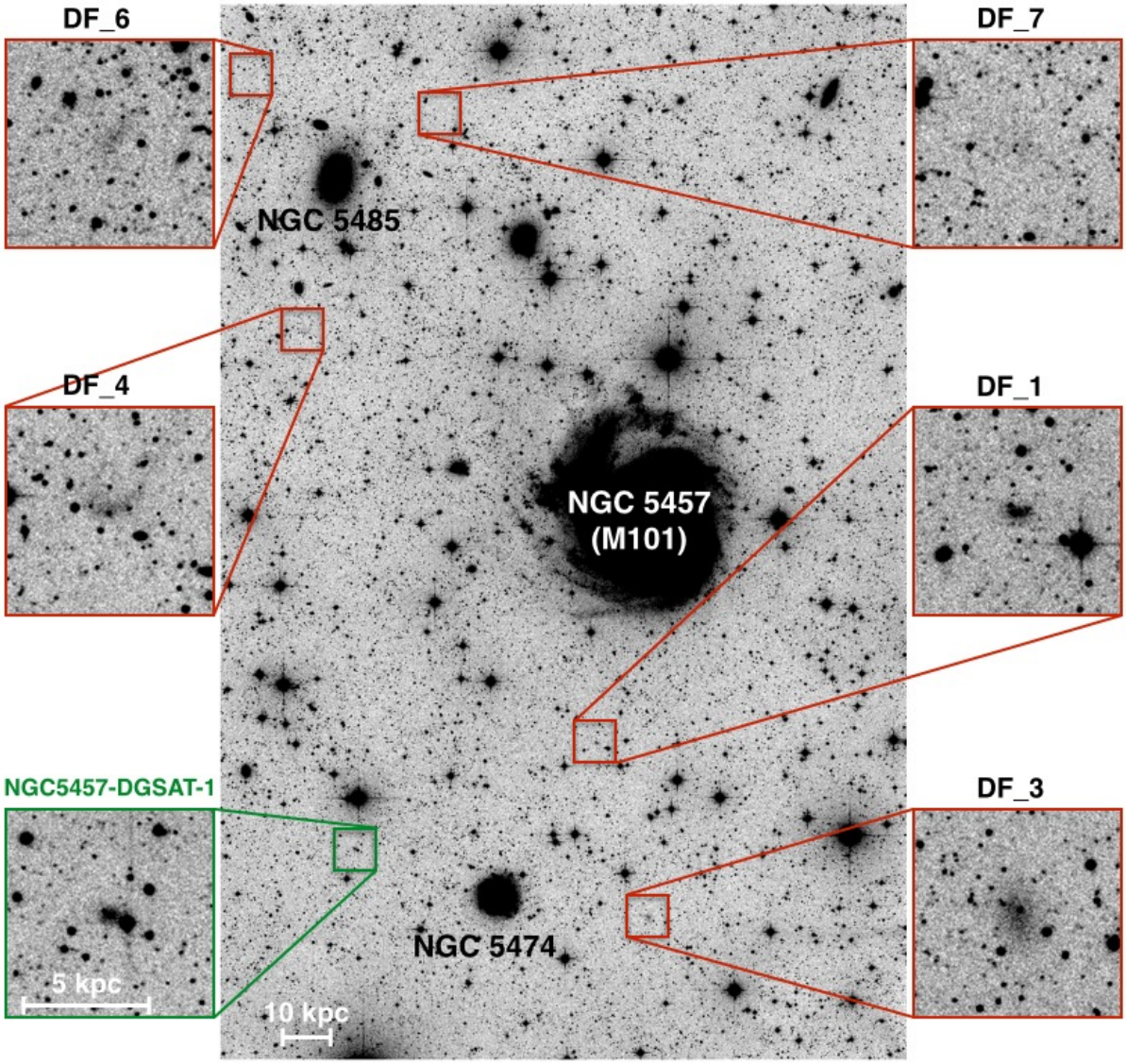

Figure 4.2: The $2.^{\circ}0 \times 1.^{\circ}3$ field of NGC 5457 (M101) or Pinwheel galaxy. North is up and east is to the left. The zoomed-in squares show the low surface brightness galaxies in the image. The red squares are five dwarf galaxies reported by the Dragonfly project (DF-number), which are all confirmed. The green square is the one newly discovered in our image (NGC5457-DGSAT-1). Two of the Dragonfly LSB galaxies, namely the DF-2 and DF-5, are outside the field of our image.

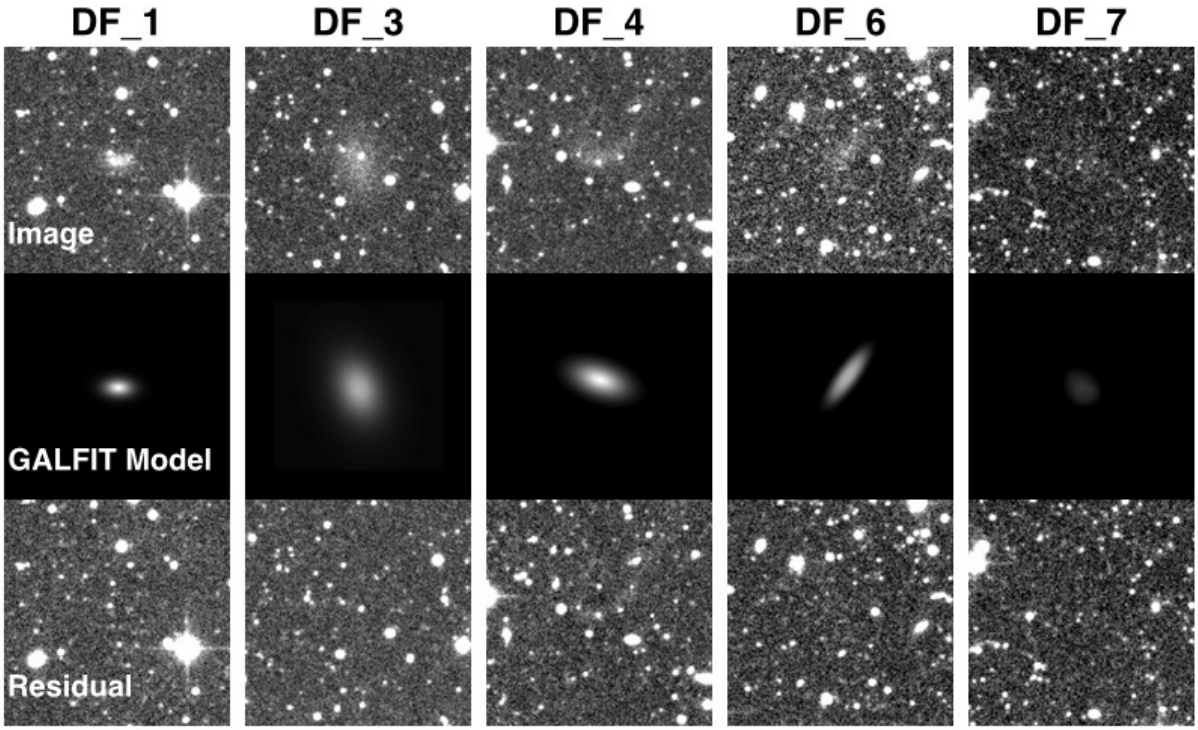

Figure 4.3: Top: Dragonfly LSB galaxies (DF-number) detected in our image. DF-2 and DF-5 are outside our field. Middle: our GALFIT models (see Table 4.3 for the results of the modelling). Bottom: residual images obtained by subtracting the model image (middle) from the main image (top). The results are in agreement with those reported by the Dragonfly team (see Figure 4.4).

disruption of this galaxy. The results of the modelling for DF galaxies are shown in the top part of Table 4.3. We assume $(g - r) = 0.5$, which is the mean value for these galaxies measured by Merritt et al. (2014)[4]. Figure 4.4 gives a comparison of our results with those of the Dragonfly team. This agreement further confirms the consistency of our magnitude calibration and galaxy-modelling approach.

The newly discovered galaxy in the field of M101 and its model are shown in Figure 4.5. We also included the SDSS image of the same field for comparison. In the case of NGC5457-DGSAT-1, the bright neighbouring star was masked before fitting a Sersic model to the galaxy. In the resulting residual image, the bright star (USNO-A2.0 1425-08068454, indicated with a red arrow) and the uncatalogued point source (identified by a yellow arrow) can be easily compared with those in the SDSS image. The results of the modelling for NGC5457-DGSAT-1 are also shown in Table 4.3. The reason that Dragonfly could not detect this object is most likely because their FWHM is larger and, therefore, this LSB galaxy and its neighbouring stars were not resolved properly. Another interesting feature in our image of the field of M101 is illustrated in Figure 4.6. It shows a clear stellar tidal stream around the background elliptical galaxy NGC 5485, which is situated at a distance of around 28 Mpc. This ring-like LSB feature was also noted by Karachentsev et al. (2015) and could be related to the tidal disruption of a dwarf satellite with an almost circular orbit.

[4] We assume the same value for other dwarf galaxy candidates that we present later in this paper. Assuming that the dwarf galaxies are composed by metal-poor, old populations, we can expect an integrated colour similar to those of Galactic globular clusters (Vanderbeke et al. 2014).

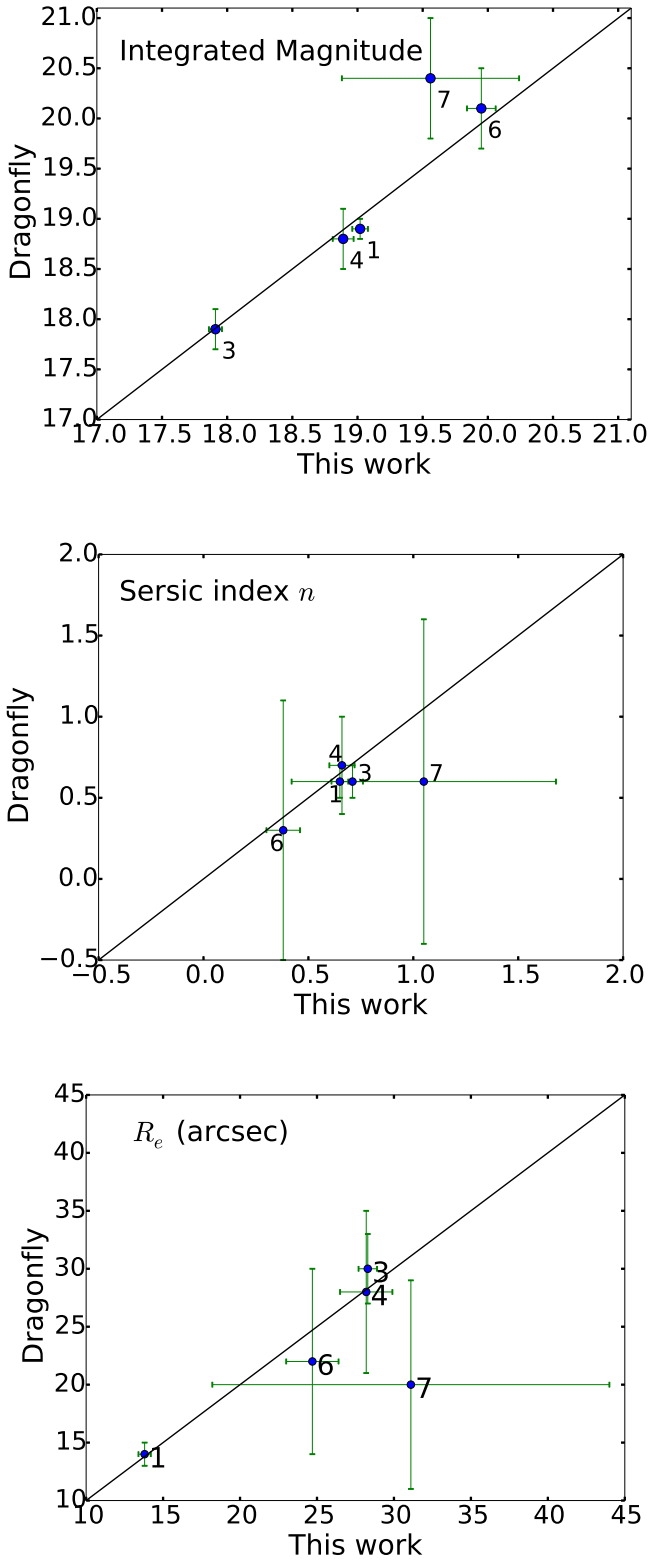

Figure 4.4: Comparison between our results for integrated magnitude (in g band, assuming $(g-r) = 0.5$), Sersic index n, and effective radius R_e with those of the Dragonfly study (Merritt et al. 2014) for DF1, 3, 4, 6, and 7.

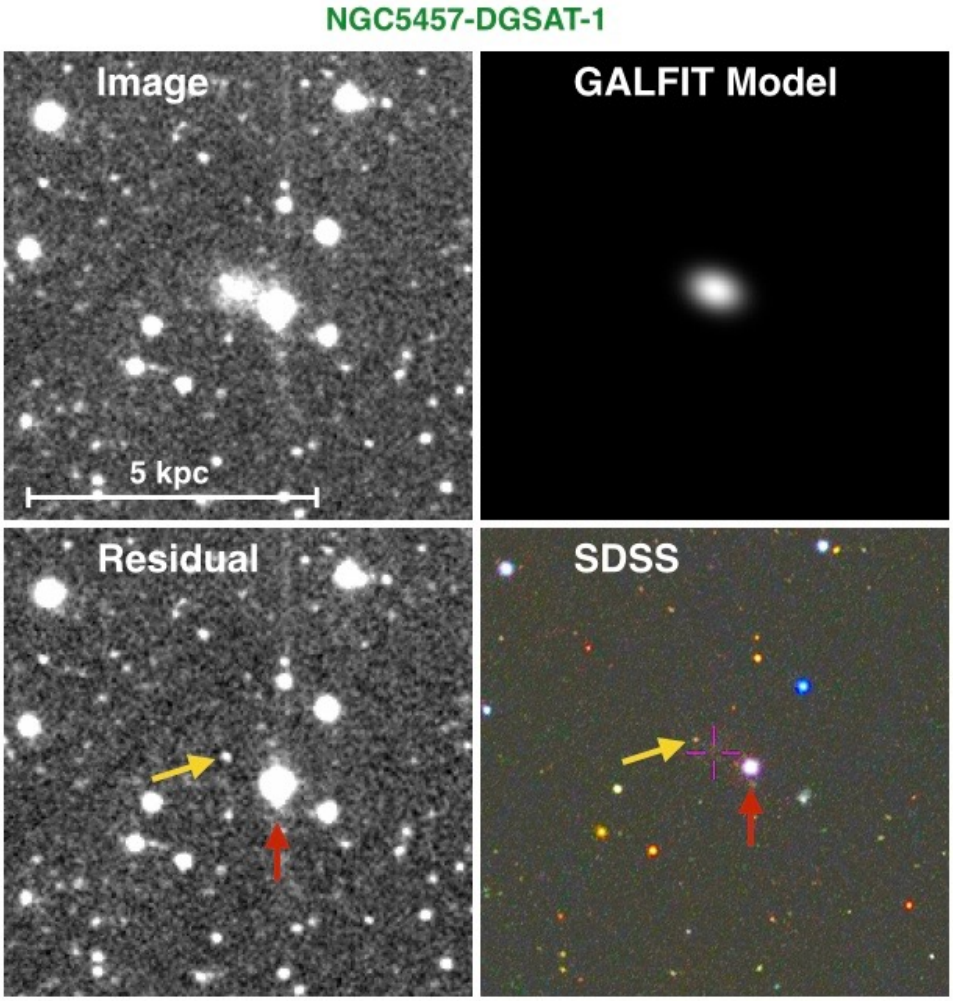

Figure 4.5: Top left: cut out portion of our image centred on NGC5457-DGSAT-1. Top right: our GALFIT model (see Table 4.3 for the results of the modelling). Bottom left: residual image obtained by subtracting the model image from the main image. Bottom right: same field from SDSS for comparison. In both of the bottom images, the red arrow points to USNO-A2.0 1425-08068454 and the yellow arrow points to an uncatalogued point source. The comparison of these two images with the main image (top left) helps to better see NGC5457-DGSAT-1.

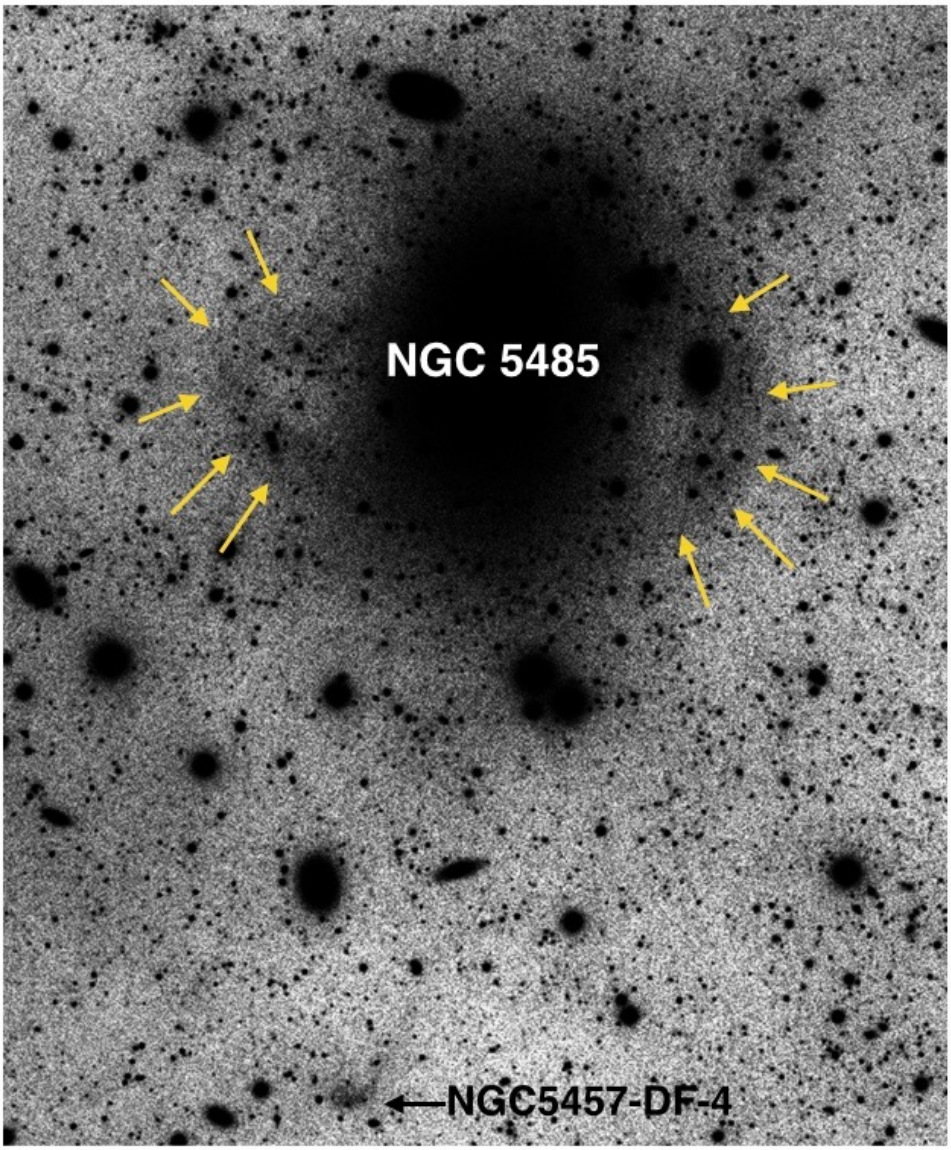

Figure 4.6: Low surface brightness stellar tidal stream around the elliptical galaxy NGC 5485 is shown by yellow arrows. North is up and east is to the left. NGC5457-DF-4 is also indicated by name (see Figure 4.2).

Table 4.3: LSB galaxies, their equatorial coordinates, RA and DEC, and their structural parameters evaluated by GALFIT modelling; calibrated integrated magnitude, r_{cal}, surface brightness, μ_e, at effective radius, the Sersic index, n, the effective radius, R_e, and the axis ratio, b/a. In the case of NGC5457-DF-7, the axis ratio is kept fixed (to the value given by SExtractor) to stabilize the fitting.

ID	RA	DEC	r_{cal} (mag)	μ_e (mag.arcsec^{-2})	n	R_e (arcsec)	b/a
NGC5457-DF-1	14:03:45.0	+53:56:38.0	18.52 ± 0.06	26.14 ± 0.06	0.65 ± 0.04	13.8 ± 0.4	0.59 ± 0.01
NGC5457-DF-3	14:03:05.8	+53:36:52.0	17.41 ± 0.05	26.58 ± 0.05	0.71 ± 0.05	28.3 ± 0.6	0.56 ± 0.01
NGC5457-DF-4	14:07:33.8	+54:42:39.2	18.39 ± 0.08	27.46 ± 0.07	0.66 ± 0.06	28.2 ± 1.7	0.53 ± 0.02
NGC5457-DF-6	14:08:18.7	+55:11:30.6	19.45 ± 0.11	27.43 ± 0.11	0.38 ± 0.08	24.7 ± 1.7	0.31 ± 0.02
NGC5457-DF-7	14:05:47.5	+55:07:57.3	19.06 ± 0.68	28.85 ± 0.68	1.05 ± 0.63	31.1 ± 12.9	0.70(fixed)
NGC5457-DGSAT-1	14:06:49.8	+53:44:28.8	18.49 ± 0.10	25.69 ± 0.10	0.47 ± 0.07	10.8 ± 0.9	0.72 ± 0.06
NGC2683-DGSAT-1	8:52:47.8	+33:47:33.1	14.49 ± 0.07	26.29 ± 0.07	0.61 ± 0.05	80.9 ± 5.8	0.82 ± 0.01
NGC2683-DGSAT-2	8:55:23.3	+33:33:32.4	16.11 ± 0.06	25.62 ± 0.06	0.78 ± 0.02	27.3 ± 0.7	0.79 ± 0.01
NGC2683-DGSAT-3	8:55:10.9	+33:36:45.7	18.59 ± 0.07	25.52 ± 0.07	0.61 ± 0.04	11.2 ± 0.1	0.61 ± 0.02
NGC2683-DGSAT-4	8:54:20.0	+33:14:49.1	18.99 ± 0.23	26.48 ± 0.23	0.70 ± 0.19	9.9 ± 2.1	0.98 ± 0.14
NGC2683-DGSAT-5	8:52:48.1	+32:49:37.7	20.08 ± 0.08	26.00 ± 0.08	0.52 ± 0.05	6.8 ± 0.4	0.55 ± 0.03
NGC3628-DGSAT-1	11:21:37.0	+13:26:50.7	19.21 ± 0.08	25.78 ± 0.08	0.46 ± 0.03	8.2 ± 0.3	0.74 ± 0.02
NGC4594-DGSAT-1	12:39:55.1	-11:44:38.4	16.04 ± 0.09	25.86 ± 0.09	0.79 ± 0.04	31.0 ± 2.7	0.82 ± 0.01
NGC4594-DGSAT-2	12:39:51.6	-11:20:24.8	19.28 ± 0.08	25.68 ± 0.08	0.57 ± 0.02	6.8 ± 0.1	0.85 ± 0.01
NGC4594-DGSAT-3	12:39:32.8	-11:13:38.5	17.77 ± 0.11	25.26 ± 0.11	0.19 ± 0.07	13.33 ± 0.6	0.82 ± 0.04
NGC4631-DGSAT-1	12:42:53.1	+32:27:19.0	18.74 ± 0.08	26.91 ± 0.08	0.73 ± 0.03	14.66 ± 0.5	0.81 ± 0.01
NGC4631-DGSAT-2	12:42:06.1	+32:37:14.8	17.25 ± 0.08	27.01 ± 0.08	0.48 ± 0.02	34.52 ± 1.5	0.74 ± 0.01
NGC4631-DGSAT-3	12:41:08.0	+32:26:50.4	20.95 ± 0.09	26.37 ± 0.09	0.28 ± 0.03	5.57 ± 0.2	0.63 ± 0.02
NGC7814-DGSAT-1	0:03:24.0	+16:11:13.6	18.05 ± 0.06	25.26 ± 0.06	0.38 ± 0.05	11.5 ± 0.2	0.71 ± 0.01
NGC7814-DGSAT-2	0:03:06.8	+16:18:33.3	18.19 ± 0.05	26.14 ± 0.05	0.66 ± 0.02	18.7 ± 0.5	0.43 ± 0.01

4.5.2 The NGC 2683 field

NGC 2683 is a galaxy with a bulge and an active nucleus at an adopted distance of 10.5 ± 2.2 Mpc (Table 4.2). Our image of the field of this galaxy (Figure 4.7) has the dimensions of 1.°4 × 1.°4, a pixel scale of 1.22 arcsec/pixel, and its FWHM is ≈ 3.5 arcsec. We zoomed into five LSB galaxies in this image. The two largest and brightest of these LSB galaxies were already catalogued in Karachentsev et al. (2004) as [KK98a] 084944.1+335913 and [KK98a] 085216.3+334502. We refer to these galaxies as NGC2683-DGSAT-1 and 2 in our catalogue. The former has an irregular shape, while the latter is almost spheroidal. Similar to the other LSB galaxies in this paper, we fit a Sersic model to these two galaxies. The results are shown in Figure 4.8 and Table 4.3. In the case of NGC2683-DGSAT-1, because of its irregular shape and many foreground stars on top of its image, it is very difficult to obtain an accurate model. Therefore, its GALFIT model and the corresponding measurements in this paper are only estimates. As can be seen in the figure, we could also discover three other dwarf galaxy candidates in the field of NGC 2683. During the final phase of the writing of this paper, we noted that one of these dwarf galaxy candidates, namely NGC2683-DGSAT-4, was independently discovered by Karachentsev et al. (2015). Results of modelling NGC2683-DGSAT-3 to 5 can also be seen in Figure 4.8 and Table 4.3.

4.5.3 The NGC 3628 field

NGC 3628 is a spiral galaxy with an active nucleus and lies at an adopted distance of 10.9 ± 2.4 Mpc (Table 4.2). Our image from the field of this galaxy comprises 0.°7 × 0.°7 and it is shown in Figure 4.9. The pixel size of this image is 0.62 arcsec and its FWHM is ≈ 2.7 arcsec. The immediately observable features of this image are a heavily perturbed disk and a stream parallel to the disk of the galaxy. In the

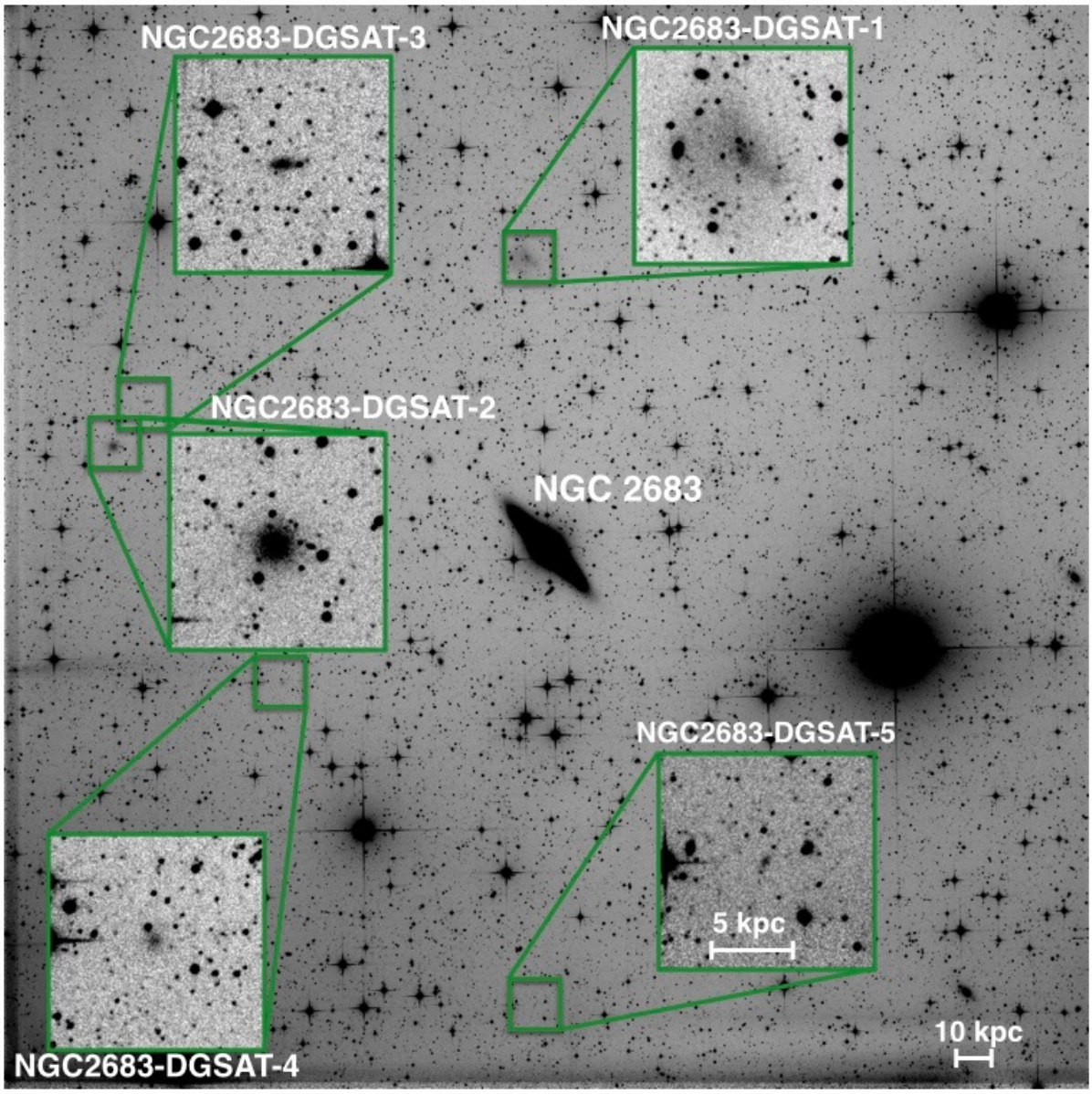

Figure 4.7: The 1°.4 × 1°.4 field of NGC 2683. North is up and east is to the left. The zoomed-in squares show the LSB galaxies in the image.

figure, we show the NGC3628-UCD1, which was identified and studied by Jennings et al. (2015) to be an embedded star cluster in the observed stream. The dwarf galaxy candidate that we found in this field is also shown in Figure 4.9. The GALFIT modelling and its results are shown in Figure 4.8 and Table 4.3.

4.5.4 The NGC 4594 (M104) field

NGC 4594 (also known as the Sombrero galaxy) is an unbarred galaxy with a large bulge and an active nucleus. The adopted distance to this galaxy is 11.1 ± 4.1 Mpc (see Table 4.2). Our image of the field of this galaxy (Figure 4.10) spans $0.^{\circ}7 \times 0.^{\circ}7$ and has a pixel size of 0.62 arcsec. We could detect three LSB galaxies in this image, which are also shown in Figure 4.10. The results of GALFIT modelling for these three candidates are also shown in Figure 4.8 and Table 4.3.

4.5.5 The NGC 4631 field

NGC 4631 (also known as the Whale Galaxy) is an edge-on galaxy at an adopted distance of 5.8 ± 1.5 Mpc (Table 4.2). Our image of the field of this galaxy (Figure 4.11) spans $0.^{\circ}4 \times 0.^{\circ}3$ and has a pixel size of 0.43 arcsec. Karachentsev et al. (2014) and Martínez-Delgado et al. (2015a) reported three dwarf galaxy candidates aligned with a stellar stream in deep images of this galaxy. Two of these LSB galaxies, which are in the field of our image, (and in our catalogue we refer to them as NGC4631-DGSAT-1 and 2) are shown in Figure 4.11. Our searching method could also find another new dwarf galaxy candidate in this field; NGC4631-DGSAT-3. The results of GALFIT modelling for these three candidates are shown in Figure 4.8 and Table 4.3.

4.5.6 The NGC 7814 field

NGC 7814 is an edge-on disk galaxy with a prominent bulge at the distance of 16.4 ± 3.6 Mpc (see Table 4.2). Our image from the field of this galaxy spans $0.^{\circ}5 \times 0.^{\circ}5$ and is shown in Figure 4.12. The pixel scale of this image is 0.43 arcsec/pixel and its FWHM is ≈ 2.2 arcsec. The two discovered LSB galaxies in the field of this galaxy, NGC7814-DGSAT-1 and 2, are also shown in Figure 4.12; they are visible even without zooming. The results of GALFIT modelling of these dwarf galaxy candidates are presented in Figure 4.8. The foreground stars were removed by fitting the PSF model of the image using DAOPHOT before using GALFIT. The clean residual images show that the models are good. The results can be seen in Table 4.3.

4.6 Discussion

All of the detected objects in this work have very low surface brightness (>25 mag/arcsec^2), and cannot be detected in the available images from large-scale surveys like the SDSS or PanSTARRs. This also makes it very difficult to undertake follow-up observations for obtaining their radial velocities (and confirming their association with the spiral galaxies) even for 8 meter class telescopes. For further analysis, and given their low angular projected distances, we assume that the discovered galaxies are the satellites of these nearby massive galaxies (see Table 4.2), and derive their physical properties[5]. Interestingly, some

[5] In addition, the contamination of our search for faint satellites around massive spirals by background dE galaxies of similar colour is significantly reduced when we probe the surface brightness regime below 25 mag/arcsec^2, as is shown in the typical scaling relation diagram for early-type galaxies (e.g. see the surface brightness versus size relation diagram in Toloba et al. 2012).

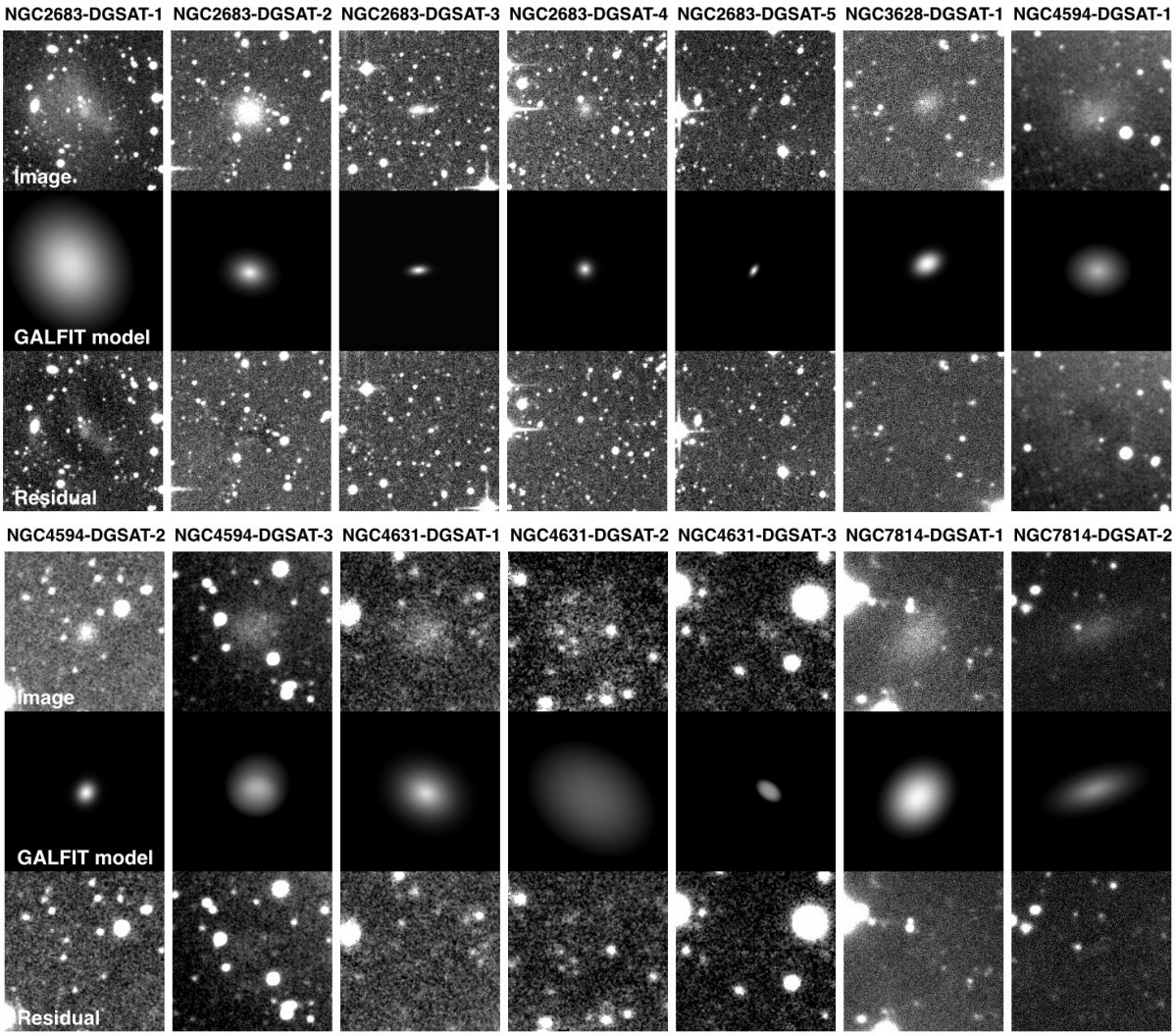

Figure 4.8: In both the top and bottom panels, the first row: dwarf galaxy candidates detected in our images (except that of the NGC 5457); the middle row: our GALFIT models (see Table 4.3 for the results of the modelling), and the bottom row: residual images obtained by subtracting the model image (middle) from the main image (top).

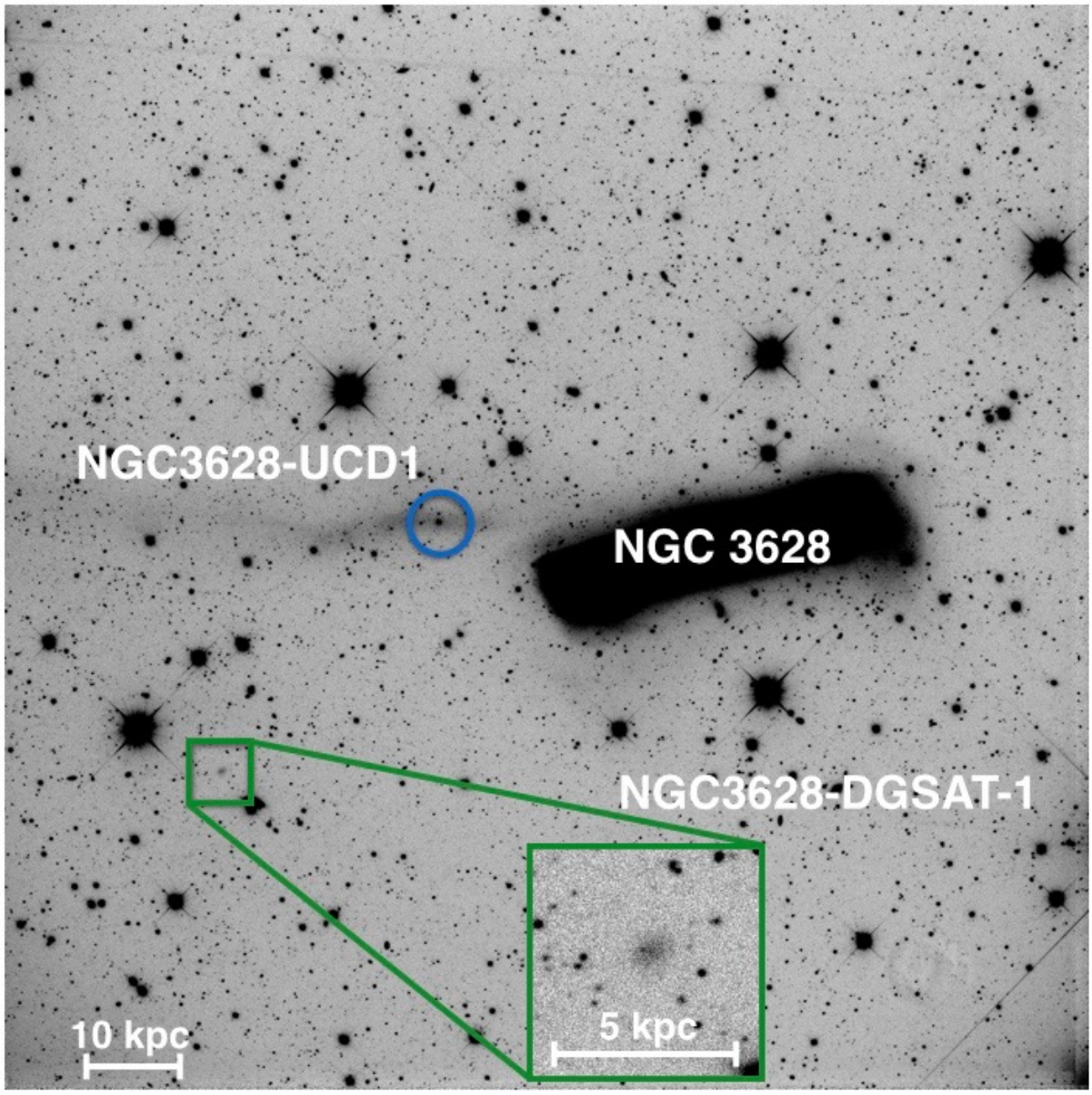

Figure 4.9: The 0.°7 × 0.°7 field of NGC 3628. North is up and east is to the left. The zoomed-in square shows the LSB galaxy we found in the image and the blue circle shows the NGC3628-UCD1 (Jennings et al. 2015).

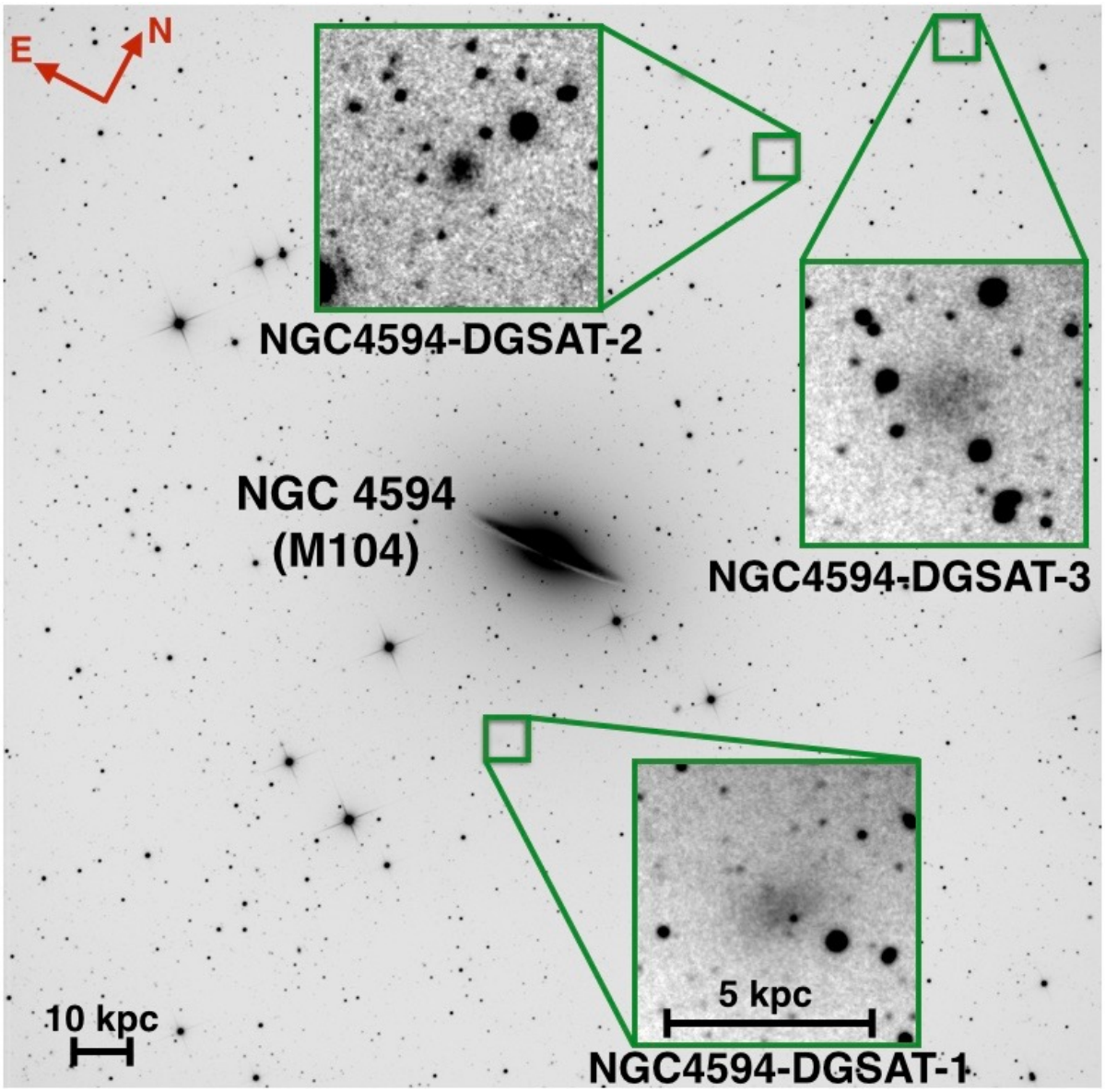

Figure 4.10: The $0.^{\circ}7 \times 0.^{\circ}7$ field of NGC 4594. North (N) and east (E) are indicated with arrows at the top left of the image. The zoomed-in squares show the LSB galaxies we found in the image.

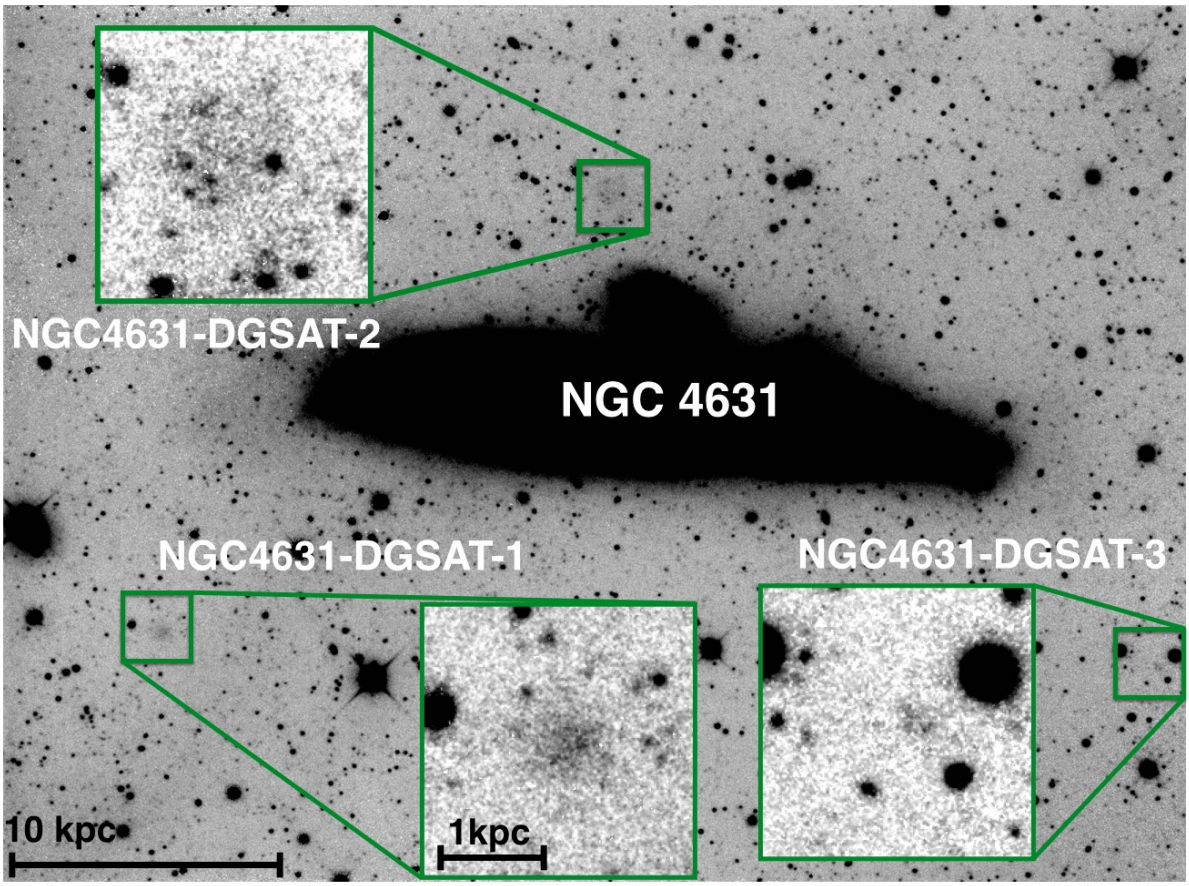

Figure 4.11: The 0.°4 × 0.°3 field of NGC 4631. North is up and east is to the left. The zoomed-in squares show the LSB galaxies in the image.

of our faint systems display insights of tidal disruption (e.g. NGC2683-DGSAT-1, NGC7814-DGSAT-2, and NGC5457-DF-4), which suggest their proximity to the spiral host.

In Table 4.4 we list the effective radius (in pc), projected distance (in kpc) to their putative massive companion, absolute magnitude, M, (in mag) and luminosity, L, (in $10^6 \times L_\odot$) of all 20 dwarf galaxy candidates that we listed in Table 4.3. Their r-band luminosities and their effective radii are in the ranges $0.1 \times 10^6 \lesssim \left(\frac{L}{L_\odot}\right)_r \lesssim 127 \times 10^6$, and 160 pc $\lesssim R_e \lesssim 4.1$ kpc, respectively. Their r-band surface brightnesses and absolute magnitudes are in the ranges $25.3 \lesssim \mu_e \lesssim 28.8$ mag.arcsec^{-2} and $-15.6 \lesssim M_r \lesssim -7.8$, respectively. Figure 4.13 shows the distribution of the dwarf galaxy candidates studied in this work in the R_e vs. L, μ_e vs. R_e, and μ_e vs. M_V planes. The known dwarf galaxies of the Local Group (McConnachie 2012) are also shown in these plots. In the μ_e vs. M_V plane, two of our dwarf galaxy candidates, which are outliers to the overall trend, are indicated with names. NGC5457-DF-7 is very faint and its measured properties have large uncertainties, but NGC2683-DGSAT-1 is bright enough to show its irregular shape, which suggests that it might be undergoing tidal disruption.

As can be seen, the DGSAT candidates can be characterized by similar properties as those of the LG dwarf galaxies. This shows the ability of the DGSAT, and in general small telescopes, for discovering such faint systems in the Local Volume.

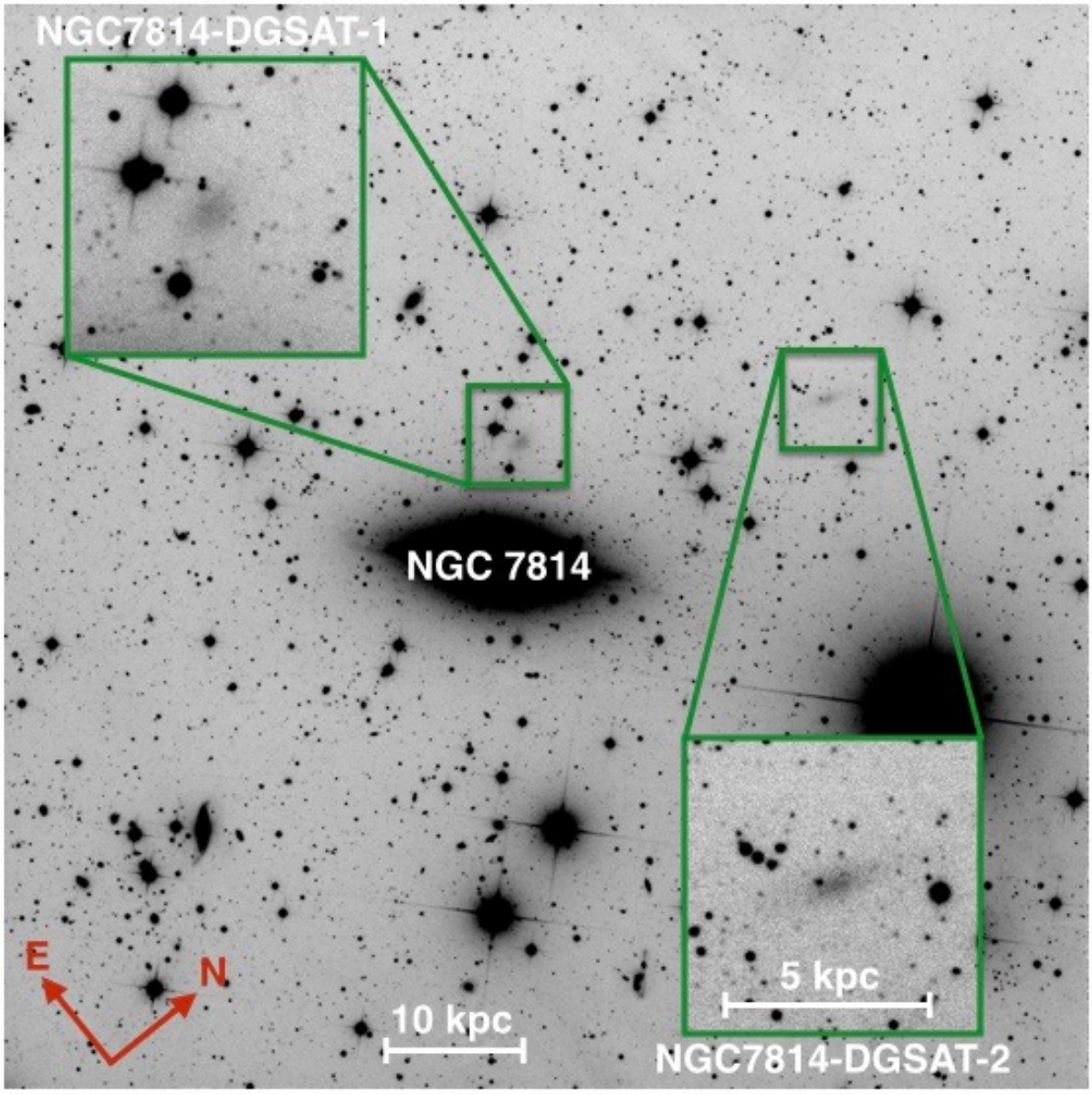

Figure 4.12: The 0.°5 × 0.°5 field of NGC 7814. North (N) and east (E) are indicated with arrows at the bottom left of the image. The zoomed-in squares show the LSB galaxies we found in the image.

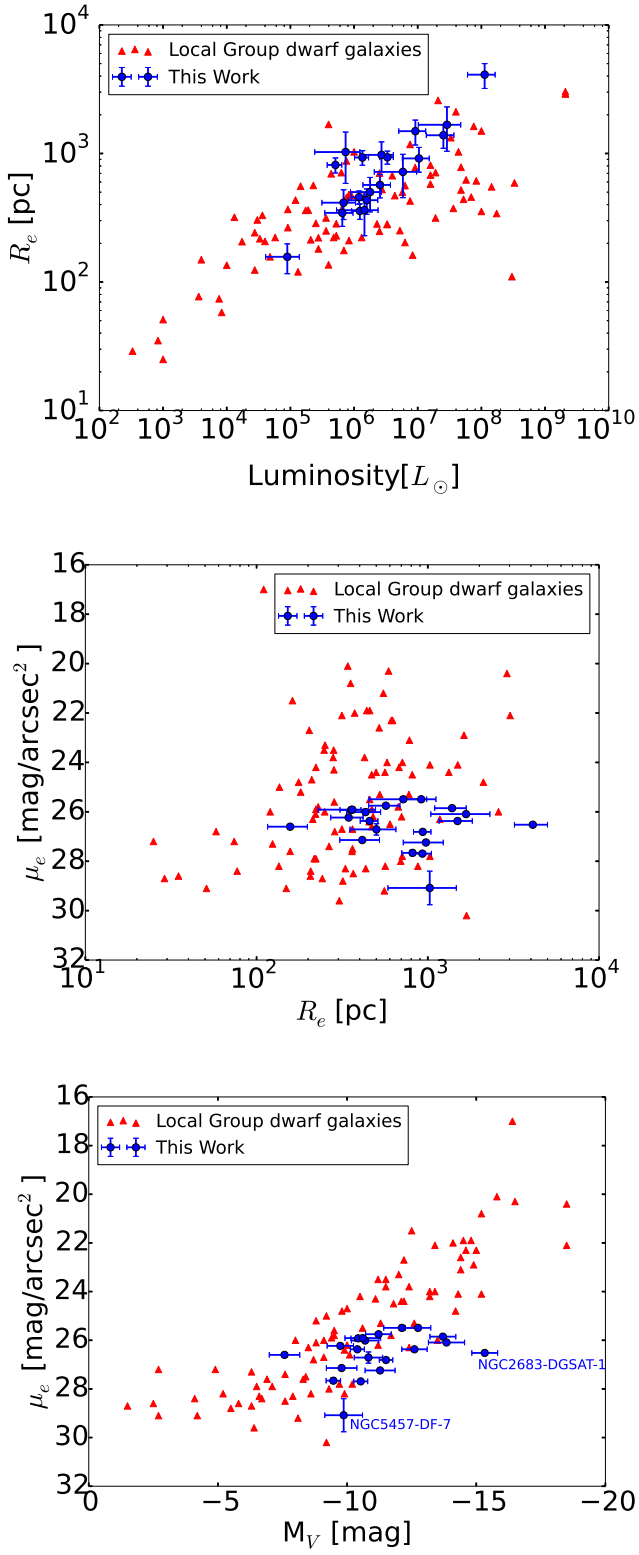

Figure 4.13: A comparison between the properties of the dwarf galaxy candidates studied in this work and the known dwarf galaxies of the Local Group (McConnachie 2012). Top: effective radius in pc vs. V band luminosity in $L_\odot$. Middle: V band surface brightness in mag.arcsec^{-2} vs. effective radius in pc. Bottom: V band surface brightness in mag.arcsec^{-2} vs. absolute V band magnitude. In the latter, the outliers are emphasized by name. The V band quantities were obtained by transforming r band magnitudes to V magnitudes using Fukugita et al. (1996).

Table 4.4: Physical properties of the LSB galaxies assuming that they are satellites of the nearby (in projection) massive galaxies. R_e and d_P are effective radius and projected distance of the dwarf candidate to the centre of the host galaxy, respectively. M_r denotes the absolute magnitude in r-band (assuming the distance moduli in Table 4.2) and the last column provides the luminosity in units of 10^6 solar luminosities, $L_\odot$.

ID	R_e (pc)	d_P (kpc)	M_r (mag)	$\left(\frac{L}{L_\odot}\right)_r \times 10^6$
NGC5457-DF-1	457 ± 54	49.2 ± 5.6	−10.63 ± 0.27	1.3 ± 0.3
NGC5457-DF-3	934 ± 109	87.4 ± 10.0	−11.74 ± 0.26	3.8 ± 0.9
NGC5457-DF-4	930 ± 120	86.8 ± 9.9	−10.76 ± 0.27	1.5 ± 0.4
NGC5457-DF-6	814 ± 109	133.3 ± 15.3	−9.70 ± 0.28	0.6 ± 0.1
NGC5457-DF-7	1026 ± 441	103.7 ± 11.9	−10.10 ± 0.73	0.8 ± 0.6
NGC5457-DGSAT-1	357 ± 50	96.2 ± 11.0	−10.66 ± 0.28	1.4 ± 0.4
NGC2683-DGSAT-1	4103 ± 898	68.2 ± 14.1	−15.56 ± 0.50	127.1 ± 58.5
NGC2683-DGSAT-2	1386 ± 289	104.9 ± 21.7	−13.94 ± 0.50	28.6 ± 13.2
NGC2683-DGSAT-3	569 ± 118	100.5 ± 20.8	−11.45 ± 0.50	2.9 ± 1.3
NGC2683-DGSAT-4	501 ± 150	69.8 ± 14.4	−11.06 ± 0.55	2.0 ± 1.0
NGC2683-DGSAT-5	345 ± 74	107.7 ± 22.3	−9.97 ± 0.51	0.7 ± 0.3
NGC3628-DGSAT-1	433 ± 97	67.9 ± 15.1	−10.93 ± 0.53	1.8 ± 0.9
NGC4594-DGSAT-1	1672 ± 631	24.0 ± 8.8	−14.08 ± 0.70	32.5 ± 21.0
NGC4594-DGSAT-2	362 ± 133	54.9 ± 20.2	−10.84 ± 0.69	1.6 ± 1.0
NGC4594-DGSAT-3	719 ± 266	79.6 ± 29.2	−12.35 ± 0.70	6.6 ± 4.3
NGC4631-DGSAT-1	414 ± 108	19.3 ± 5.0	−10.02 ± 0.59	0.8 ± 0.4
NGC4631-DGSAT-2	975 ± 256	8.1 ± 2.1	−11.51 ± 0.58	3.0 ± 1.6
NGC4631-DGSAT-3	157 ± 41	22.5 ± 5.8	−7.81 ± 0.59	0.1 ± 0.05
NGC7814-DGSAT-1	915 ± 200	16.2 ± 3.5	−12.98 ± 0.49	11.8 ± 5.3
NGC7814-DGSAT-2	1491 ± 328	47.6 ± 10.4	−12.84 ± 0.49	10.4 ± 4.7

4.7 Conclusion

We presented the first results of the DGSAT project and its ability to find LSB galaxies around nearby Milky Way-like galaxies using a network of robotic amateur telescopes. We developed a semi-automatic pipeline to calibrate the luminance images taken by amateur telescopes, search for dwarf galaxy candidates, and extract their observed parameters. By exploring the fields of six nearby massive galaxies NGC 2683, NGC 3628, NGC 4594 (M104), NGC 4631, NGC 5457 (M101), and NGC 7814, we discovered eleven so far unknown LSB galaxies in our images. The models of these galaxies were obtained using the GALFIT software and by fitting a Sersic function to their light profile. While revisiting the field of M101, we have discovered a new LSB galaxy that was not reported by the Dragonfly team, which recently observed the field of this galaxy. Our results for the rest of the LSB galaxies in the field of M101 confirm those of the Dragonfly study but our image provides significantly better angular resolution.

The LSB galaxies in the fields of the other mentioned massive galaxies show similar observed properties to those in the field of M101. In addition to the eleven newly identified dwarf galaxy candidates, we also analysed the morphology of nine already known objects. The surface brightness of all of these galaxies are in the range $25.3 \lesssim \mu_e \lesssim 28.8$ mag.arcsec^{-2} and their Sersic indices are $n \lesssim 1$, which are similar to those of the dwarf satellites in the Local Group (McConnachie 2012). Assuming that they are dwarf satellites of their neighbouring (in projection) massive galaxies, their r-band absolute magnitude, their luminosities, and their effective radii are in the ranges $-15.6 \lesssim M_r \lesssim -7.8$, $0.1 \times 10^6 \lesssim \left(\frac{L}{L_\odot}\right)_r \lesssim 127 \times 10^6$,

and 160 pc $\lesssim R_e \lesssim$ 4.1 kpc, respectively. In particular, DGSAT is able to detect LSB systems with similar observed properties to those of the “classical” dwarf spheroidal galaxies around the Milky Way.

To confirm that the discovered galaxies are dwarf satellites of their nearby massive galaxies, further observations are required. Our results show the potential of amateur telescopes in discovering more dwarf galaxies in the Local Volume, which enables us to further test models of galaxy formation and evolution outside the Local Group.

Acknowledgments

We thank the referee for providing constructive comments on the manuscript. BJ thanks Chien Peng for his kind help with the GALFIT software, Eva Grebel for her constructive comments on the project, and Luca Fossati and Tim Schrabback for their useful guidance on image analysis. BJ was supported for this research through stipends from the International Max Planck Research School (IMPRS) for Astronomy and Astrophysics at the Universities of Bonn and Cologne, and from Karl Menten and SPODYR groups. DMD acknowledges support by the Sonderforschungsbereich (SFB) 881 "The Milky Way system" of the German Research Foundation (DFG), particularly through the sub-project A2. This research has made use of the SIMBAD database, and the VizieR catalogue access tool, operated at CDS in Strasbourg, France, and the "Aladin sky atlas", which was developed at the same location.

CHAPTER 5

Summary of the Thesis and Future Perspectives

How does the Universe work?, what is this Universe at all?, where do we come from?, and where are we going? These and a lot of other questions have always occupied humans minds. Cosmology is trying to find the answer to some of these questions. The Universe has revealed its tremendous vastness to us, but with that it also faces us with numerous new questions.

In the past century, a standard model of cosmology has been formed which is founded on the Einstein's theory of gravity and on the assumption of the Cosmological Principle. The observations show that the absolute majority of galaxies, the building blocks of the large scale structure of the Universe, are receding from us. The Big Bang model states that the Universe initiated from a very hot and dense state and kept expanding since then. During the expansion, gravity has been responsible for gathering the constituents of the Universe and for forming larger and larger structures. In the standard model, a form of matter that does not (or only very weakly) interact with electromagnetic radiation but interacts gravitationally, called *dark matter*, is the main matter component of the Universe and very influential in the formation of structure. The other main component of the standard model is *dark energy* which is believed to be responsible for the observations which are indicative of the acceleration of the expansion of the Universe. The standard model can provide reasonably well explanations for many observations, but is challenged by some others.

The two main problems of the standard model are that dark matter has not been directly detected yet and we do not know what dark energy is. Doubts have been raised on whether or not these two main components of the standard model exist at all (Milgrom 1983; Bekenstein 2004; Mannheim 2006; Wiltshire 2009; Kroupa 2012; Koyama 2016). In this thesis, we provided investigations towards solving some of the interesting issues with the current standard model of cosmology that are different from, but related to, the two mentioned main problems.

On large scales some observed deviations from isotropy in the CMB (Tegmark et al. 2003; Eriksen et al. 2004; Hansen et al. 2004) led to a boost in the studies of testing the assumption of isotropy of the Cosmological Principle. In Chapters 2 and 3, we probed isotropy on the distance scales larger that 800 Mpc and smaller than 200 Mpc, respectively. In Chapter 2, we studied the isotropy of cosmic acceleration by searching for any directional dependency in the magnitude-redshift relation of SNe Ia with redshift larger than 0.2 from the Union2.1 catalog (Suzuki et al. 2012). We found that the most discrepant direction in this relation is aligned with the CMB dipole at the 95-99% confidence level. This might

be either due to uncleaned systematics or some yet unknown phenomena. Interestingly, the anomalous alignment of the CMB quadrupole and octopole is also very close to the CMB dipole. However, the sparseness of the current SNe Ia catalogs makes it difficult to draw a firm conclusion. The result of this research was published in Javanmardi et al. (2015). This study should be repeated when larger data sets from future surveys become available.

In Chapter 3, we provided the first test of the isotropy of the all-sky distribution of galaxy morphological types. We used the data of more than 60,000 galaxies from the HyperLeda catalog (Paturel et al. 2003a,b; Makarov et al. 2014) that covers the entire sky (except from the Galactic region). We found a significant hemispherical asymmetry in the distribution of morphological types that is aligned with the celestial equator at the 99.8%, and with the ecliptic at least at the 94.6%, confidence levels. Interestingly, one of the CMB anomalies, the hemispherical asymmetry, is also aligned with the ecliptic (Eriksen et al. 2004). In general, our results show that the distribution of galaxy morphological types in the northern sky is significantly different from that of the southern sky. If this anisotropy is real, it would be a major challenge for the Cosmological Principle. However, the fact that it is aligned with the celestial equator indicates that it is most likely due to a systematic bias in the classification of the galaxy types or in the homogenization of the catalog, possibly due to the fact that the HyperLeda catalog is a combination of data from various telescopes. This indicates that more effort must be put on developing uniform and automated classification methods applicable to the large forthcoming data from near future surveys. The result of this research was published in Javanmardi & Kroupa (2017). Further studies are needed to find the exact source of this anisotropy.

One of the most promising future surveys for detecting a large number of Type Ia Supernovae and galaxies across a large fraction of the sky is the Large Synoptic Survey Telescope (LSST, Ivezic et al. 2008). It is planned to scan all the southern and part of the northern sky with a 3200 megapixel camera and an $\approx$ 8.5m mirror for 10 years. LSST is expected to start operation in mid 2020s. Another interesting survey will be done by the Euclid satellite which is planned to be launched in 2020 (Laureijs et al. 2011). It aims at mapping the large scale structure of the Universe by observing and measuring the redshift of $\approx 10^8$ galaxies. In principle, both of these surveys are also able to deliver morphological measurements of a considerable number of galaxies in the Local Universe which would be valuable for different studies including probing isotropy.

On small scales, observations regarding the number and spatial distribution of dwarf satellite galaxies in our Local Group of galaxies are not in agreement with the predictions of the standard model's structure formation scenario. However, it is vital to check if similar properties are observed in other galaxy groups and for that we need to increase the number of known dwarf satellite galaxies outside the Local Group. While large telescopes and big surveys are delivering a large amount of valuable data, we have shown recently that small telescopes are also capable of contributing to the cutting-edge research in this field. In Chapter 4, we presented our Dwarf Galaxy Survey with Amateur Telescopes (DGSAT) which was able (in its first application) to discover eleven low surface brightness (LSB) galaxies in the field of six nearby Milky-way-type galaxies. These LSB galaxies, have similar properties to the dwarf satellite galaxies in the Local Group. The first results of DGSAT was published in Javanmardi et al. (2016). This project will continue and we are very optimistic that it will be able to detect a large number of LSB galaxies. Such surveys will eventually enable us to test the predictions of different cosmological models on scales of galaxy groups with higher statistical confidence.

The next two coming decades will be very exciting for cosmology as a huge amount of data with unprecedented quality will become available. These data can transform our perception of the Universe and our place within it.

"Oh me! Oh life! of the questions of these recurring,
Of the endless trains of the faithless, of cities fill'd with the foolish,
Of myself forever reproaching myself, (for who more foolish than I, and who more faithless?)
Of eyes that vainly crave the light, of the objects mean, of the struggle ever renew'd,
Of the poor results of all, of the plodding and sordid crowds I see around me,
Of the empty and useless years of the rest, with the rest me intertwined,
The question, O me! so sad, recurring—What good amid these, O me, O life?
Answer.
That you are here—that life exists and identity,
That the powerful play goes on, and you may contribute a verse."

Walt Whitman (1819–1892)

Bibliography

Abraham, R. G. 1998, ArXiv Astrophysics e-prints

Abraham, R. G. & van den Bergh, S. 2001, Science, 293, 1273

Akrami, Y., Fantaye, Y., Shafieloo, A., et al. 2014, ApJ, 784, L42

Al-Sufi, A. R. 964, Book of Fixed Stars (World Digital Library (WDL) of the U.S. Library of Congress)

Albrecht, A. & Steinhardt, P. J. 1982, Physical Review Letters, 48, 1220

Alonso, D., Salvador, A. I., Sánchez, F. J., et al. 2015, MNRAS, 449, 670

Alpher, R. A. & Herman, R. C. 1948, Physical Review, 74, 1737

Alpher, R. A. & Herman, R. C. 1949, Physical Review, 75, 1089

Amanullah, R., Lidman, C., Rubin, D., et al. 2010, ApJ, 716, 712

Antoniou, I. & Perivolaropoulos, L. 2010, J. Cosmology Astropart. Phys., 12, 12

Appleby, S. & Shafieloo, A. 2014a, J. Cosmology Astropart. Phys., 10, 070

Appleby, S. & Shafieloo, A. 2014b, J. Cosmology Astropart. Phys., 3, 7

Appleby, S., Shafieloo, A., & Johnson, A. 2015, ApJ, 801, 76

Astier, P., Guy, J., Regnault, N., et al. 2006, A&A, 447, 31

Baillard, A., Bertin, E., de Lapparent, V., et al. 2011, A&A, 532, A74

Bechtol, K., Drlica-Wagner, A., Balbinot, E., et al. 2015, ApJ, 807, 50

Bekenstein, J. D. 2004, Phys. Rev. D, 70, 083509

Bengaly, Jr., C. A. P. 2016, J. Cosmology Astropart. Phys., 4, 036

Bengaly, Jr., C. A. P., Bernui, A., Alcaniz, J. S., Xavier, H. S., & Novaes, C. P. 2016, ArXiv e-prints

Bennett, C. L., Halpern, M., Hinshaw, G., et al. 2003, ApJS, 148, 1

Bennett, C. L., Hill, R. S., Hinshaw, G., et al. 2011, ApJS, 192, 17

Bernstein, J. P., Kessler, R., Kuhlmann, S., et al. 2012, ApJ, 753, 152

Bertin, E. & Arnouts, S. 1996, A&AS, 117, 393

Block, L. D. & Freeman, C. K. 2015, A Walk with Dr Allan Sandage—Changing the History of Galaxy Morphology, Forever, ed. K. Freeman, B. Elmegreen, D. Block, & M. Woolway (Cham: Springer International Publishing), 1–20

Blomqvist, M., Mörtsell, E., & Nobili, S. 2008, J. Cosmology Astropart. Phys., 6, 27

Bonvin, C., Durrer, R., & Kunz, M. 2006, Physical Review Letters, 96, 191302

Boylan-Kolchin, M., Bullock, J. S., & Kaplinghat, M. 2011, MNRAS, 415, L40

Brout, D., Scolnic, D., Rest, A., et al. 2013, in American Astronomical Society Meeting Abstracts, Vol. 221, American Astronomical Society Meeting Abstracts #221, 253.12

Buchert, T., Coley, A. A., Kleinert, H., Roukema, B. F., & Wiltshire, D. L. 2015, ArXiv e-prints

Bull, P., Akrami, Y., Adamek, J., et al. 2016, Physics of the Dark Universe, 12, 56

Bullock, J. S. 2010, ArXiv e-prints

Buta, R. J. 2013, Galaxy Morphology, ed. J. Falcón-Barroso & J. H. Knapen, 155

Cai, R.-G., Ma, Y.-Z., Tang, B., & Tuo, Z.-L. 2013, Phys. Rev. D, 87, 123522

Calvi, R., Poggianti, B. M., Fasano, G., & Vulcani, B. 2012, MNRAS, 419, L14

Campanelli, L., Cea, P., Fogli, G. L., & Marrone, A. 2011, Phys. Rev. D, 83, 103503

Carvalho, C. S. & Marques, K. 2015, ArXiv e-prints

Chang, Z. & Lin, H.-N. 2015, MNRAS, 446, 2952

Chiboucas, K., Jacobs, B. A., Tully, R. B., & Karachentsev, I. D. 2013, AJ, 146, 126

Chonis, T. S. & Gaskell, C. M. 2008, AJ, 135, 264

Colin, J., Mohayaee, R., Sarkar, S., & Shafieloo, A. 2011, MNRAS, 414, 264

Combes, F. 2016, Galactic Bulges, 418, 413

Cooke, R. & Lynden-Bell, D. 2010, MNRAS, 401, 1409

Cooper, A. P., Martínez-Delgado, D., Helly, J., et al. 2011, ApJ, 743, L21

Copi, C. J., Huterer, D., Schwarz, D. J., & Starkman, G. D. 2010a, Advances in Astronomy, 2010, 92

Copi, C. J., Huterer, D., Schwarz, D. J., & Starkman, G. D. 2010b, Advances in Astronomy, 2010

Copi, C. J., Huterer, D., Schwarz, D. J., & Starkman, G. D. 2013, ArXiv e-prints

Copi, C. J., Huterer, D., Schwarz, D. J., & Starkman, G. D. 2015, MNRAS, 449, 3458

Copi, C. J., Huterer, D., & Starkman, G. D. 2004, Phys. Rev. D, 70, 043515

Crnojević, D., Sand, D. J., Spekkens, K., et al. 2015, ArXiv e-prints

Davies, J. I., Davies, L. J. M., & Keenan, O. C. 2016, MNRAS, 456, 1607

de Lapparent, V., Baillard, A., & Bertin, E. 2011, A&A, 532, A75

de Vaucouleurs, G. 1959, Handbuch der Physik, 53, 275

de Vaucouleurs, G., de Vaucouleurs, A., Corwin, Jr., H. G., et al. 1991, Third Reference Catalogue of Bright Galaxies. Volume I: Explanations and references. Volume II: Data for galaxies between 0^h and 12^h. Volume III: Data for galaxies between 12^h and 24^h.

Del Popolo, A. 2014, International Journal of Modern Physics D, 23, 1430005

Del Popolo, A., Lima, J. A. S., Fabris, J. C., & Rodrigues, D. C. 2014, J. Cosmology Astropart. Phys., 4, 021

Delgado-Serrano, R., Hammer, F., Yang, Y. B., et al. 2010, A&A, 509, A78

Diemand, J., Kuhlen, M., Madau, P., et al. 2008, Nature, 454, 735

Dodelson, S. 2003, Modern cosmology

Dreyer, J. L. E. 1888, MmRAS, 49, 1

Einstein, A. 1915, Sitzungsberichte der Königlich Preußischen Akademie der Wissenschaften (Berlin), Seite 844-847.

Eriksen, H. K., Hansen, F. K., Banday, A. J., Górski, K. M., & Lilje, P. B. 2004, ApJ, 605, 14

Feindt, U., Kerschhaggl, M., Kowalski, M., et al. 2013, A&A, 560, A90

Fixsen, D. J. 2009, ApJ, 707, 916

Flores, H., Hammer, F., Fouquet, S., et al. 2016, MNRAS, 457, L14

Friedmann, A. 1922, Zeitschrift fur Physik, 10, 377

Fukugita, M., Ichikawa, T., Gunn, J. E., et al. 1996, AJ, 111, 1748

Fukugita, M., Nakamura, O., Okamura, S., et al. 2007, AJ, 134, 579

Galilei, G. 1610, Sidereus Nuncius (Venetiis : Apud Thomam Baglionum)

Gallagher, III, J. S. & Wyse, R. F. G. 1994, PASP, 106, 1225

Gamow, G. 1946, Physical Review, 70, 572

Gamow, G. 1956, Vistas in Astronomy, 2, 1726

Gentile, G., Famaey, B., Combes, F., et al. 2007, A&A, 472, L25

Giallongo, E., Menci, N., Grazian, A., et al. 2015, ApJ, 813, 68

Gibelyou, C. & Huterer, D. 2012, MNRAS, 427, 1994

Goobar, A. & Leibundgut, B. 2011, Annual Review of Nuclear and Particle Science, 61, 251

Górski, K. M., Hivon, E., Banday, A. J., et al. 2005, ApJ, 622, 759

Grebel, E. K. 2011, in IAU Symposium, Vol. 270, Computational Star Formation, ed. J. Alves, B. G. Elmegreen, J. M. Girart, & V. Trimble, 335–346

Gupta, S. & Saini, T. D. 2010, MNRAS, 407, 651

Guth, A. H. 1981, Phys. Rev. D, 23, 347

Guth, A. H., ed. 1997, The inflationary universe. The quest for a new theory of cosmic origins

Guy, J., Astier, P., Baumont, S., & et al. 2007, A&A, 466, 11

Hansen, F. K., Banday, A. J., & Górski, K. M. 2004, MNRAS, 354, 641

Hansen, F. K., Banday, A. J., Górski, K. M., Eriksen, H. K., & Lilje, P. B. 2009, ApJ, 704, 1448

Heneka, C., Marra, V., & Amendola, L. 2014, MNRAS, 439, 1855

Herrera-Endoqui, M., Díaz-García, S., Laurikainen, E., & Salo, H. 2015, A&A, 582, A86

Hopkins, P. F., Bundy, K., Croton, D., et al. 2010, ApJ, 715, 202

Hubble, E. 1929, Proceedings of the National Academy of Science, 15, 168

Hubble, E. P. 1926, ApJ, 64

Hubble, E. P. 1936, Realm of the Nebulae

Huertas-Company, M., Gravet, R., Cabrera-Vives, G., et al. 2015, ApJS, 221, 8

Ibata, R. A., Famaey, B., Lewis, G. F., Ibata, N. G., & Martin, N. 2015, ApJ, 805, 67

Ibata, R. A., Ibata, N. G., Lewis, G. F., et al. 2014, ApJ, 784, L6

Ibata, R. A., Lewis, G. F., Conn, A. R., et al. 2013, Nature, 493, 62

Ivezic, Z., Tyson, J. A., Abel, B., et al. 2008, ArXiv e-prints

Javanmardi, B. & Kroupa, P. 2017, A&A, 597, A120

Javanmardi, B., Martinez-Delgado, D., Kroupa, P., et al. 2016, A&A, 588, A89

Javanmardi, B., Porciani, C., Kroupa, P., & Pflamm-Altenburg, J. 2015, ApJ, 810, 47

Jeans, J. H. 1928, Astronomy and Cosmogony (Cambridge University Press)

Jennings, Z. G., Romanowsky, A. J., Brodie, J. P., et al. 2015, ApJ, 812, L10

Jiménez, J. B., Salzano, V., & Lazkoz, R. 2015, Physics Letters B, 741, 168

Kalus, B., Schwarz, D. J., Seikel, M., & Wiegand, A. 2013, A&A, 553, A56

Karachentsev, I. D., Bautzmann, D., Neyer, F., et al. 2014, ArXiv e-prints

Karachentsev, I. D., Karachentseva, V. E., Huchtmeier, W. K., & Makarov, D. I. 2004, AJ, 127, 2031

Karachentsev, I. D., Riepe, P., Zilch, T., et al. 2015, Astrophysical Bulletin, 70, 379

Karpenka, N. V., Feroz, F., & Hobson, M. P. 2015, MNRAS, 449, 2405

Kessler, R., Becker, A. C., Cinabro, D., et al. 2009, ApJS, 185, 32

Klypin, A., Kravtsov, A. V., Valenzuela, O., & Prada, F. 1999, ApJ, 522, 82

Koda, J., Yagi, M., Komiyama, Y., et al. 2015, ApJ, 802, L24

Koivisto, T. & Mota, D. F. 2008, ApJ, 679, 1

Kolatt, T. S. & Lahav, O. 2001, MNRAS, 323, 859

Kormendy, J. 1982, Morphology and dynamics of galaxies; Proceedings of the Twelfth Advanced Course, Saas-Fee, Switzerland, March 29-April 3, 1982 (A84-15502 04-90). Sauverny, Switzerland, Observatoire de Geneve, 1983, p. 113-288., 12, 113

Kowalski, M., Rubin, D., Aldering, G., et al. 2008, ApJ, 686, 749

Koyama, K. 2016, Reports on Progress in Physics, 79, 046902

Kravtsov, A. 2010, Advances in Astronomy, 2010, 281913

Kroupa, P. 2012, PASA, 29, 395

Kroupa, P. 2015, Canadian Journal of Physics, 93, 169

Kroupa, P., Famaey, B., de Boer, K. S., et al. 2010, A&A, 523, A32

Kroupa, P., Pawlowski, M., & Milgrom, M. 2012, International Journal of Modern Physics D, 21, 30003

Kroupa, P., Theis, C., & Boily, C. M. 2005, A&A, 431, 517

Krywult, J., Tasca, L. A. M., Pollo, A., et al. 2016, ArXiv e-prints

Kuminski, E. & Shamir, L. 2016, ApJS, 223, 20

Laureijs, R., Amiaux, J., Arduini, S., et al. 2011, ArXiv e-prints

Lelli, F., Duc, P.-A., Brinks, E., et al. 2015, A&A, 584, A113

Lemaître, G. 1927, Annales de la Société Scientifique de Bruxelles, 47, 49

Li, X., Lin, H.-N., Wang, S., & Chang, Z. 2013, European Physical Journal C, 73, 2653

Liddle, A. 2003, An Introduction to Modern Cosmology, Second Edition, 188

Lin, H.-N., Li, X., & Chang, Z. 2016, MNRAS, 460, 617

Linde, A. D. 1982, Physics Letters B, 108, 389

López-Corredoira, M. & Kroupa, P. 2016a, ApJ, 817, 75

López-Corredoira, M. & Kroupa, P. 2016b, ApJ, 817, 75

Maartens, R. 2011, Philosophical Transactions of the Royal Society of London Series A, 369, 5115

Makarov, D., Prugniel, P., Terekhova, N., Courtois, H., & Vauglin, I. 2014, A&A, 570, A13

Makarov, D. I., Sharina, M. E., Karachentseva, V. E., & Karachentsev, I. D. 2015, A&A, 581, A82

Mannheim, P. D. 2006, Progress in Particle and Nuclear Physics, 56, 340

Mariano, A. & Perivolaropoulos, L. 2012, Phys. Rev. D, 86, 083517

Marinoni, C., Bel, J., & Buzzi, A. 2012, J. Cosmology Astropart. Phys., 10, 036

Martínez-Delgado, D., D'Onghia, E., Chonis, T. S., et al. 2015a, AJ, 150, 116

Martínez-Delgado, D., Gabany, R. J., Crawford, K., et al. 2010, AJ, 140, 962

Martínez-Delgado, D., Laesker, R., Sharina, M., & et al. 2015b, AJ, in press

Martínez-Delgado, D., Peñarrubia, J., Gabany, R. J., et al. 2008, ApJ, 689, 184

Mather, J. C., Hauser, M. G., Bennett, C. L., et al. 1991, Advances in Space Research, 11, 181

Matvievskaya, G. P. 1983, Istoriko-Astronomicheskie Issledovaniya, 16, 92

McConnachie, A. W. 2012, AJ, 144, 4

Merritt, A., van Dokkum, P., & Abraham, R. 2014, ApJ, 787, L37

Messier, C. 1771, French Academy of Sciences, 435

Migkas, K. & Plionis, M. 2016, Rev. Mexicana Astron. Astrofis., 52, 133

Milgrom, M. 1983, ApJ, 270, 365

Molaeinezhad, A., Falcón-Barroso, J., Martínez-Valpuesta, I., et al. 2016, MNRAS, 456, 692

Moore, B., Ghigna, S., Governato, F., et al. 1999, ApJ, 524, L19

Muñoz, R. P., Eigenthaler, P., Puzia, T. H., et al. 2015, ApJ, 813, L15

Mukherjee, S., Aluri, P. K., Das, S., Shaikh, S., & Souradeep, T. 2016, J. Cosmology Astropart. Phys., 6, 042

Naim, A. 1995, Astrophysical Letters and Communications, 31, 87

Naim, A., Ratnatunga, K. U., & Griffiths, R. E. 1997, ApJ, 476, 510

Nair, P. B. & Abraham, R. G. 2010, ApJS, 186, 427

Paturel, G., Petit, C., Prugniel, P., et al. 2003a, A&A, 412, 45

Paturel, G., Theureau, G., Bottinelli, L., et al. 2003b, A&A, 412, 57

Pawlowski, M. S., Famaey, B., Jerjen, H., et al. 2014, MNRAS, 442, 2362

Pawlowski, M. S., Famaey, B., Merritt, D., & Kroupa, P. 2015a, ApJ, 815, 19

Pawlowski, M. S. & Kroupa, P. 2014, ApJ, 790, 74

Pawlowski, M. S., Kroupa, P., & Jerjen, H. 2013, MNRAS, 435, 1928

Pawlowski, M. S. & McGaugh, S. S. 2014, ApJ, 789, L24

Pawlowski, M. S., McGaugh, S. S., & Jerjen, H. 2015b, MNRAS, 453, 1047

Pawlowski, M. S., Pflamm-Altenburg, J., & Kroupa, P. 2012, MNRAS, 423, 1109

Peacock, J. A. 1999, Cosmological Physics, 704

Peng, C. Y., Ho, L. C., Impey, C. D., & Rix, H.-W. 2002, AJ, 124, 266

Penzias, A. A. & Wilson, R. W. 1965, ApJ, 142, 419

Perlmutter, S., Aldering, G., Goldhaber, G., et al. 1999, ApJ, 517, 565

Planck Collaboration, Ade, P. A. R., Aghanim, N., et al. 2014a, A&A, 571, A1

Planck Collaboration, Ade, P. A. R., Aghanim, N., et al. 2014b, A&A, 571, A23

Planck Collaboration, Ade, P. A. R., Aghanim, N., et al. 2015, ArXiv e-prints

Planck Collaboration, Aghanim, N., Armitage-Caplan, C., et al. 2014c, A&A, 571, A27

Poudel, A., Heinämäki, P., Nurmi, P., et al. 2016, A&A, 590, A29

Press, W. H., Flannery, B. P., & Teukolsky, S. A. 1986, Numerical recipes. The art of scientific computing

Psychogyios, A., Charmandaris, V., Diaz-Santos, T., et al. 2016, A&A, 591, A1

Rassat, A., Starck, J.-L., Paykari, P., Sureau, F., & Bobin, J. 2014a, J. Cosmology Astropart. Phys., 8, 006

Rassat, A., Starck, J.-L., Paykari, P., Sureau, F., & Bobin, J. 2014b, J. Cosmology Astropart. Phys., 8, 6

Rathaus, B., Kovetz, E. D., & Itzhaki, N. 2013, MNRAS, 431, 3678

Reynolds, J. H. 1920, Monthly Notices of the Royal Astronomical Society, 80, 746

Riess, A. G., Filippenko, A. V., Challis, P., et al. 1998, AJ, 116, 1009

Robertson, H. P. 1929, Proceedings of the National Academy of Science, 15, 822

Rubart, M. & Schwarz, D. J. 2013, A&A, 555, A117

Sachs, R. K. & Wolfe, A. M. 1967, ApJ, 147, 73

Sánchez Almeida, J., Aguerri, J. A. L., Muñoz-Tuñón, C., & Huertas-Company, M. 2011, ApJ, 735, 125

Sand, D. J., Crnojević, D., Bennet, P., et al. 2015, ApJ, 806, 95

Sand, D. J., Crnojević, D., Strader, J., et al. 2014, ApJ, 793, L7

Sandage, A. 1975, Classification and Stellar Content of Galaxies Obtained from Direct Photography, ed. A. Sandage, M. Sandage, & J. Kristian (the University of Chicago Press), 1

Schwarz, D. J., Starkman, G. D., Huterer, D., & Copi, C. J. 2004, Physical Review Letters, 93, 221301

Schwarz, D. J. & Weinhorst, B. 2007, A&A, 474, 717

Scott, D. 2006, Canadian Journal of Physics, 84, 419

Sersic, J. L. 1968, Atlas de galaxias australes

Shibuya, T., Ouchi, M., & Harikane, Y. 2015, ApJS, 219, 15

Singal, A. K. 2011, ApJ, 742, L23

Slipher, V. M. 1915, Popular Astronomy, 23, 21

Smoot, G., Bennett, C., Weber, R., et al. 1990, ApJ, 360, 685

Spencer, M., Loebman, S., & Yoachim, P. 2014, ApJ, 788, 146

Springel, V., Frenk, C. S., & White, S. D. M. 2006, Nature, 440, 1137

Stetson, P. B. 1987, PASP, 99, 191

Suzuki, N., Rubin, D., Lidman, C., et al. 2012, ApJ, 746, 85

Tegmark, M., de Oliveira-Costa, A., & Hamilton, A. J. 2003, Phys. Rev. D, 68, 123523

Tiwari, P. & Nusser, A. 2016, J. Cosmology Astropart. Phys., 3, 062

Toloba, E., Boselli, A., Peletier, R. F., et al. 2012, A&A, 548, A78

Turnbull, S. J., Hudson, M. J., Feldman, H. A., et al. 2012, MNRAS, 420, 447

van den Bergh, S. 1998, Galaxy Morphology and Classification

van Gent, R. H. 2014, Sufi, Abd al-Rahman, al- (903–986), ed. I. Kalin, S. Ayduz, & C. Dagli (Oxford University Press), 286–288

Vanderbeke, J., West, M. J., De Propris, R., et al. 2014, MNRAS, 437, 1734

Vogelsberger, M., Genel, S., Springel, V., et al. 2014, Nature, 509, 177

Walker, A. G. 1933, MNRAS, 94, 159

Wang, J. S. & Wang, F. Y. 2014, MNRAS, 443, 1680

Wiltshire, D. L. 2009, International Journal of Modern Physics D, 18, 2121

Yang, X., Wang, F. Y., & Chu, Z. 2014, MNRAS, 437, 1840

Yoon, M., Huterer, D., Gibelyou, C., Kovács, A., & Szapudi, I. 2014, MNRAS, 445, L60

Zhao, W., Wu, P., & Zhang, Y. 2013, International Journal of Modern Physics D, 22, 50060

Acknowledgements

This thesis, though being a challenging effort during a considerable fraction of my life since I have got to know myself, is but a tiny contribution to the global efforts of many researchers devoted to understanding the Cosmos. I try to remember everyone who have been helpful to me in different ways during the past years of my life which led to where I am now. I have learned a lot from many people and I admire all of them.

I would like to start with Pavel Kroupa from whom I have learned (amongst many other things) to try to *think out of the box* and to develop a critical way of looking at "established scientific models". It has been a great pleasure for me to have him as my PhD supervisor. He has always been supportive to me and I have always enjoyed discussing with him on various topics, thank you Pavel. In addition, I would like to thank Cristiano Porciani from whom I have learned to be critical *towards my own research results* and to keep an open mind. His patience and comments on my first project have been very influential on the improvement of that work and my whole PhD. I have bothered him a lot, but he has always been supportive, thank you Cris. Also, I am grateful to David Martinez-Delgado and Christian Henkel for their kind and patient advisership and for their support, I have learned a lot from them. The next thanks goes to the other members of my thesis committee, Emmanouil (Manolis) Angelakis, Jan Pflamm-Altenburg, and Douglas Applegate for their precious comments and feedback. Furthermore, I am thankful to my good friends and colleagues, Michael (aka *Michi* or *The Postdoc*), Joerg, Marcel, Fabian, Armin, Ahmed, Seungkyung, Andrea and other past and current members of the SPODYR group in Bonn.

I would also like to thank those who have been influential on the path I have taken before even starting the PhD studies. I am indebted to Ahmad Poostforush from whom I learned the basics of scientific approach, to Farshad Khunjush from whom I learned the fundamentals of computer programming, to Sadegh Movahed from whom I learned the basics of doing research, to the Biruni Observatory and to its former director Nematollah Riazi (who supervised my first astronomy project), and to the past members of the Student Astronomical Society of Shiraz University (Kanoon Nojum) specially Alireza Molaeinezhad.

I am also very thankful to the administrative members of AIfA, IMPRS, and MPIfR, specially Christina Stein-Schmitz, Ole Marggraf, Andreas Boedewig, Simone Pott, Barbara Menten, and Tuyet-Le Tran. I would also like to thank Ian Brock for providing this nice LaTeX template. During my PhD studies, I have been supported financially by IMPRS in Bonn and Cologne, Karl Menten group at the MPIfR, and SPODYR group at the University of Bonn.

And many many thanks to my lovely friends and colleagues; Luca, Ana, Vassilis, Bia, Ioannis, Hariklia, Jean-Claude (JC), Hananeh, Zeinab, Zahra, Shahram (Faridani), Maryam (Habibi), Haniyeh (Mahmoudian), Saeed, Shadi, Fatima (Yousefi), Mohsen, Jens, Miriam, Aarti, Eugenia, Julia, Amrita, Luca (Fossati), Nicolas (Gonzalez), Joey, Amit, Hans, Sama (Bagheri), Isabel (Oldengott), Milos (Mirosavic), Sadra (Hajkarim), Tim, Patrick (Simon) and past and current members of the IMPRS in Bonn and Cologne. Also thanks to the coffee machine of the AIfA (for obvious reasons), to the Shiraz

Persian Restaurant in Bonn (for Juje, barg, Koobide, and Bagahli-Polo ba Mahiche), the Blazing Suns basketball club and the Homa Bonn football club.

Many thanks goes to my beloved friends (Hapishte members), Davoud, Fatima (Mirabian), Alireza (Dehghani), Sheeva, Mitra, Mehdi, Negar, Amir, Homa, Hojjat, Tannaz, Elham, and little Diana, and also Mohammad (Salari), Andishe, and Alireza (Aghajamali).

In addition, I would like to thank my uncles Ali (Chaboki) and Khalil for their supports and encouragements while I was applying for PhD positions, aunt Mojgan and uncle Hesam (and their family) for their warm attention towards me during my past four years in Germany, and uncle Hasan and his dear wife for gifting me my first astronomy book, *The Moon* by Isaac Asimov, when I was 7 years old.

And of course I want to thank my parents who (apart from being the reason for my existence) have always loved me unconditionally and supported me with all the means they had, this thesis is dedicated to them. Also I want to thank my good friend Behrouz who tolerated his older brother for 23 years before I finally left home, he changed my bedroom to a gym after that (it's OK, I miss you).

My very special thanks go to my best friend Fateme Kamali without whom the years of PhD studies would have been extremely difficult, I have learned a lot from her both scientifically and personally and I would like to keep doing so.

And in the end, I would like to express my sincere gratitude to the late Prof. Mehdi Jahan-Miri from whom I have learned the fundamentals of astrophysics and from whom for the first time I learned how breathtakingly vast is the Universe.

Publications included in this PhD thesis

- Chapter 2 is based on
  Probing the Isotropy of Cosmic Acceleration Traced By Type Ia Supernovae
  B. Javanmardi, C. Porciani, P. Kroupa, and J. Pflamm-Altenburg
  The Astrophysical Journal, 810, 47, (2015)

- Chapter 3 is based on
  Anisotropy in the all-sky distribution of galaxy morphological types
  B. Javanmardi and P. Kroupa
  Astronomy & Astrophysics, 597, A120 (2017)

- Chapter 4 is based on
  DGSAT: Dwarf Galaxy Survey with Amateur Telescopes I. Discovery of low surface brightness systems around nearby spiral galaxies
  B. Javanmardi, D. Martinez-Delgado, P. Kroupa, C. Henkel, K. Crawford, K. Teuwen, R. J. Gabany, M. Hanson, T. S. Chonis and F. Neyer
  Astronomy & Astrophysics, 588, A89, (2016)